

REPORT DOCUMENTATION PAGE				Form Approved OMB No. 0704-0188	
<p>The public reporting burden for this collection of information is estimated to average 1 hour per response, including the time for reviewing instructions, searching existing data sources, gathering and maintaining the data needed, and completing and reviewing the collection of information. Send comments regarding this burden estimate or any other aspect of this collection of information, including suggestions for reducing the burden, to Department of Defense, Washington Headquarters Services, Directorate for Information Operations and Reports (0704-0188), 1215 Jefferson Davis Highway, Suite 1204, Arlington, VA 22202-4302. Respondents should be aware that notwithstanding any other provision of law, no person shall be subject to any penalty for failing to comply with a collection of information if it does not display a currently valid OMB control number.</p> <p>PLEASE DO NOT RETURN YOUR FORM TO THE ABOVE ADDRESS.</p>					
1. REPORT DATE (DD-MM-YYYY) 16-11-2011		2. REPORT TYPE Final Performance Report		3. DATES COVERED (From - To) From 20-04-2007 To 16-11-2011	
4. TITLE AND SUBTITLE Photonic Applications using Electrooptic Optical Signal Processors				5a. CONTRACT NUMBER	
				5b. GRANT NUMBER FA9550-07-1-0384	
				5c. PROGRAM ELEMENT NUMBER	
6. AUTHOR(S) Dr. Harold R. Fetterman				5d. PROJECT NUMBER	
				5e. TASK NUMBER	
				5f. WORK UNIT NUMBER	
7. PERFORMING ORGANIZATION NAME(S) AND ADDRESS(ES) REGENTS OF THE UNIV OF CALIFORNIA OFFICE OF THE SECRETARY AND CHIEF OF STAFF TO THE REGENTS 1111 Franklin St., 12 Floor, Oakland, CA 94607				8. PERFORMING ORGANIZATION REPORT NUMBER	
9. SPONSORING/MONITORING AGENCY NAME(S) AND ADDRESS(ES) AFOSR / RSE 875 North Randolph Street, Suit 325 Room 3112 Arlington, Virginia 22203-1768				10. SPONSOR/MONITOR'S ACRONYM(S) AFOSR / RSE	
				11. SPONSOR/MONITOR'S REPORT NUMBER(S) AFRL-OSR-VA-TR-2012-0188	
12. DISTRIBUTION/AVAILABILITY STATEMENT 1) DISTRIBUTION STATEMENT A: Approved for public release; distribution is unlimited					
13. SUPPLEMENTARY NOTES					
14. ABSTRACT During the contract new designs of electrooptic signal processors were made from nonlinear optical polymers. These systems were based upon the latest lowest loss polymers available and involved a novel system of serial modules. The first implementation of these devices included ring resonators [1], analog-to-digital conversion [2] and single sideband optical links [3]. These are discussed in the paper [4] by Seo on Optical Signal Processor using electrooptic waveguides. One of the major demonstrations of this OSP approaches was the linear and parallel cascading of devices to improve modulation linearity and SFDR. The design was published [5] fabricated and tested [6]. The testing showed that significant improvement could be obtained by these techniques but that the material did not have the required electrooptic capabilities and transmission to make many cascaded sections. The next step was to try to increase the electrooptic coefficient using laser alignment techniques. This was effective in increasing the					
15. SUBJECT TERMS Photonic Applications; Electrooptic Optical Signal Processors					
16. SECURITY CLASSIFICATION OF:			17. LIMITATION OF ABSTRACT	18. NUMBER OF PAGES	19a. NAME OF RESPONSIBLE PERSON
a. REPORT	b. ABSTRACT	c. THIS PAGE			Howard Schlossberg, RSE (Program Manager)
U	U	U	UU		19b. TELEPHONE NUMBER (include area code) 703.696.7549

To: Technical Reports@AFOSR.AF.mil

Final Report: Grant #FA9550-07-1-0384

Title: Photonic Applications using Electrooptic Optical Signal Processors

During the contract new designs of electrooptic signal processors were made from nonlinear optical polymers. These systems were based upon the latest lowest loss polymers available and involved a novel system of serial modules. The first implementation of these devices included ring resonators [1], analog-to-digital conversion [2] and single sideband optical links [3]. These are discussed in the paper [4] by Seo on Optical Signal Processor using electrooptic waveguides.

One of the major demonstrations of this OSP approaches was the linear and parallel cascading of devices to improve modulation linearity and SFDR. The design was published [5] fabricated and tested [6]. The testing showed that significant improvement could be obtained by these techniques but that the material did not have the required electrooptic capabilities and transmission to make many cascaded sections.

The next step was to try to increase the electrooptic coefficient using laser alignment techniques. This was effective in increasing the number of aligned chromophores and improving performance. The paper [7] on this however showed that the material still was not sufficiently active, relative to its transmission, in our OSP applications.

Therefore we moved on to newer InP based semiconductors using Quantum Dots. In this case the nonlinear electrooptic properties come from the Quantum Confined Stark effect and can be tailored to our specific wavelengths and use. The key elements including the MMIs, resonant rings, and multilevel structures that we designed for the Polymer systems can all be transferred directly to the InP devices.

We have made and reported the first of these InP modulation devices[8] and find that they have impressive high frequency performance. In an effort to further improve the OSP systems we have recently looked at coupled Quantum Dots which significantly increase the electrooptic performance. This is currently in the process of submission [8].

Our conclusion from this study is that a new generation of Optical signal processing devices is coming based upon our designed and fabricated linear modulators. These devices will operate at tens of GHz and be significantly faster and more capable than any electronic systems. From our testing of the polymer based devices we have found that newer materials are required to realize this potential. The Quantum Dot systems look extremely promising in our study and we believe that this will form the basis of the next generation of OSP systems.

1. Design of ring resonators using electro-optic polymer waveguides **Author(s):** Byoung-Joon Seo; Seongku Kim; Fetterman, H.; Steier, W.; Jin, D.; Dinu, R. **Source:** Journal of Physical Chemistry C vol.112, no.21 : 7953-8, 29 May 2008

Book Chapter : Practical Applications of Microresonators in Optics and Photonics by Andrey Matsko CRC Press 2009
 “Electro-Optic Polymer Ring Resonators for Millimeter-Wave Modulation and Optical Signal Processing” H.Tazawa, Y.C. Hung S. Kim, W. Steier, and H. Fetterman pp. 265-93

2. High-speed photonically assisted analog-to-digital conversion using a continuous wave multiwavelength source and phase modulation **Author(s):** Bortnik, B.J.; Fetterman, H.R. **Source:** Optics Letters vol.33, no.19 : 2230-2, 1 October 2008
3. Distortion comparison of single-sideband coherent analog optical links employing X-cut and Z-cut Mach-Zehnder modulators **Author(s):** Guanghao Zhu; Bortnik, B.; Wei Liu; Fetterman, H.R.; Forber, R.; Wang, W.C. **Source:** IEEE Photonics Technology Letters vol.20, no.18 : 1548-50, 15 September 2008
4. Optical signal processor using electro-optic polymer waveguides **Author(s):** Byoung-Joon Seo; Seongku Kim; Bortnik, B.; Fetterman, H.; Jin, D.; Dinu, R. **Source:** Journal of Lightwave Technology vol.27, no.15 : 3092-106, 1 August 2009
5. A broadband linearized coherent analog fiber optic link employing dual parallel Mach-Zehnder modulators **Authors(s):** I G. Zhu, W. Liu, and H. R. Fetterman, **Source:** IEEE Photon. Technol. Lett. **21**(21), 1627–1629 (2009)
6. Nonlinear Intermodulation distortion suppression in coherent analog fiber optic link using electro-optic polymeric dual parallel Mach-Zehnder modulator **Author(s):** S. kim, W. Liu, Q. Pei, L. Dalton and H. Fetterman **Source:** Optics Express 19(8) 7865-7871 2011
7. Photoassisted Corona Poled YLD-124/DRI-co-PMMA Electrooptic Device Using Photoisomerization **Authors(s):** S. Kim, Q. Pei, H. Fetterman and L. Dalton, **Source:** IEEE Photonics Technology Letters **23**(13) 845-847 July 2011
8. High Speed InAs Quantum Dot Electrooptic Phase Modulators **Authors:** W. W.Liu, R. Kim, B. Liang, D. Huffaker, H. Fetterman **Source:** IEEE Photonic Technology Letters 23(23) 1748-1750 Dec. 2011
9. High Frequency In(Ga)As Quantum Dot Electrooptic Phase Modulators **Authors:** W. Liu, B.Liang, D. Huffaker, H. Fetterman Conference Submission

High-speed photonically assisted analog-to-digital conversion using a continuous wave multiwavelength source and phase modulation

Bartosz J. Bortnik* and Harold R. Fetterman

Department of Electrical Engineering, University of California Los Angeles (UCLA),
Los Angeles, California 90034, USA

*Corresponding author: bartb@ucla.edu

Received June 6, 2008; revised August 14, 2008; accepted August 15, 2008;
posted August 27, 2008 (Doc. ID 95371); published September 29, 2008

A more simple photonically assisted analog-to-digital conversion system utilizing a cw multiwavelength source and phase modulation instead of a mode-locked laser is presented. The output of the cw multiwavelength source is launched into a dispersive device (such as a single-mode fiber). This fiber creates a pulse train, where the central wavelength of each pulse corresponds to a spectral line of the optical source. The pulses can then be either dispersed again to perform discrete wavelength time stretching or demultiplexed for continuous time analog-to-digital conversion. We experimentally demonstrate the operation of both time stretched and interleaved systems at 38 GHz. The potential of integrating this type of system on a monolithic chip is discussed. © 2008 Optical Society of America

OCIS codes: 070.1170, 060.5060.

Photonically assisted techniques of analog-to-digital conversion (ADC) have attracted significant interest owing to the broad bandwidth and low signal losses in the optical domain [1]. Recently, there have been a number of developments in photonically assisted ADC systems utilizing time stretch, where the signal under test (SUT) is ultimately slowed in time (and hence compressed in bandwidth) by photonic means [2]. This technique permits the observation and digitization at extremely high sampling rates, up to terasamples per second to date [3]. Alternatively, this technique allows the use of inexpensive lower-speed ADC equipment when utilized on an SUT of only moderate frequency content.

However, most all-fiber photonically assisted ADC systems to date require a sophisticated and expensive mode-locked laser as the optical source. In this Letter, we propose and demonstrate experimentally a photonically assisted time-stretch analog-to-digital system operating in the millimeter-wave regime that employs a cw multiwavelength source and single-frequency phase modulation. We also propose and demonstrate a high-frequency ADC interleaved type system (for continuous time ADC) that utilizes a cw multiwavelength source and single-frequency modulation. The use of a cw source and phase modulator in place of a mode-locked laser found in conventional schemes allows for greater system flexibility while reducing complexity, cost, and easing the optical source performance requirements.

Figure 1 depicts the proposed discrete wavelength time-stretch system. This system includes a significant simplification to the previously proposed system in [2] by employing a cw multiwavelength source, single-frequency electro-optic phase modulation, and fiber dispersion in place of a broadband mode-locked laser, wavelength multiplexers, and finely tailored delay lines. Sinusoidal phase modulation at frequency f_m produces a waveform with increasing and

decreasing instantaneous frequencies as a function of time. After dispersion, various frequency components will travel at different group velocities and will “bunch up” to create pulses with a repetition period of $T=1/f_m$, given the right dispersion [4].

The same fiber used to create these pulses from the phase-modulated signal also acts to properly separate the pulses in time. This method of delaying the pulses with respect to one another is not subject to the temporal uncertainty of employing fiber-optic delay lines. The wavelength spacing $\Delta\lambda$, fiber dispersion D , and length L_1 are chosen so that pulses of adjacent central wavelengths are delayed by a time $\Delta T=pT+\Delta\tau\approx\Delta\lambda DL_1$ apart, where p is an integer and $\Delta\tau$ is a time smaller than the pulse repetition period T .

The pulses are then launched into the amplitude modulator and sample the SUT. After the modulator, they are dispersed again in a second shorter spool of fiber and detected via electronic means. Note that unlike a system that uses a mode-locked laser, where the maximum wavelength separation (and hence amount of temporal separation after dispersion) is limited by the spectral bandwidth of the laser, in the proposed system it is determined by the wavelength separation between the cw spectral lines. Further-

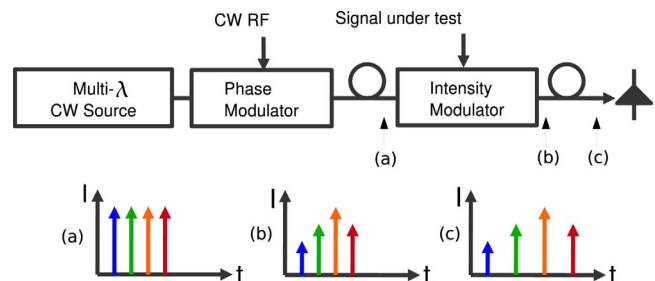


Fig. 1. (Color online) Schematic of the proposed architecture utilizing a cw multiwavelength source, phase modulation, and fiber dispersion in place of a mode-locked laser.

more, there is no stipulation on the coherence among the spectral lines, and there is a modest linewidth requirement of each line, corresponding to the phase modulation frequency, typically on the order of a few gigahertz.

To experimentally demonstrate this photonic ADC system, a commercially available rack of 4 cw diode lasers in the $1.5\ \mu\text{m}$ wavelength region were combined together into a single fiber. The optical signal was sent into a polarization controller and an LiNbO_3 electro-optic phase modulator with a V_π of 5 V. A frequency of phase modulation of 8.95 GHz with a modulation depth of approximately 40% was used. The wavelength separation between the laser lines was set to $\Delta\lambda = 0.59\ \text{nm}$ so that the pulses were delayed by $\Delta T = 120\ \text{ps} = pT + \Delta\tau$, yielding $p = 1$ and a pulse spacing $\Delta\tau = 7\ \text{ps}$ after the first spool of fiber of length $L = 11\ \text{km}$. The pulses generated by a single cw laser and phase modulation were captured on an optical autocorrelator indicating a near transform-limited pulsewidth of 13 ps [4].

These pulses were then launched into an LiNbO_3 Mach-Zehnder modulator biased at quadrature with a V_π of 8 V that was driven by a 38 GHz SUT with a 1.5 V amplitude. The modulation frequency was limited by our driving electronics. After 2.5 km of dispersion from the second spool of single-mode fiber, the pulses were spaced 28 ps apart, yielding a time-stretch factor of $M = 4$. Observation of all temporal signals was done using a 45 GHz bandwidth photodetector and a 50 GHz bandwidth digitizing sampling oscilloscope. The observed traces for the four different wavelengths are superimposed on one trace as shown in Fig. 2. We see that, as expected, the peaks of the four pulses fit to a sinusoid of approximately 9 GHz, corresponding to a time-stretch factor of $M = 4$.

The above concept has a limited temporal aperture. The repetition rate of each pulse train corresponding to a certain wavelength is equal to the phase modulation frequency. Hence, in the above experiment, where an $f_m = 8.95\ \text{GHz}$ phase-modulation frequency was used, the pulses corresponding to an individual wavelength arrive at the photodetector with a repeti-

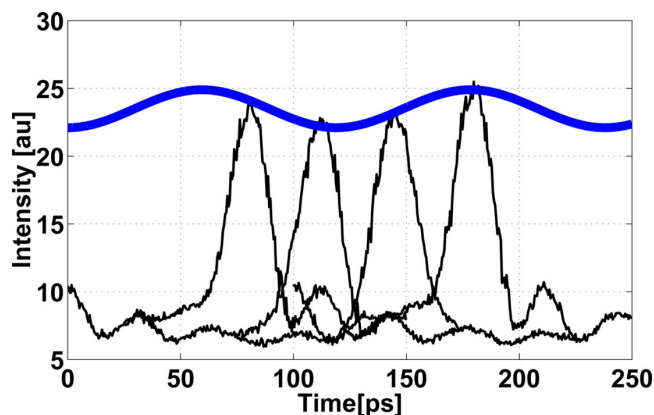


Fig. 2. (Color online) Observed traces for the four different wavelengths are superimposed on one trace. The peaks of the four pulses fit to a sinusoid of approximately 9 GHz, corresponding to a time-stretch factor of $M = 4$.

tion period of $T = 111\ \text{ps}$, which defines the above system's temporal aperture. In addition, simple causality arguments show that it is not possible to sustain time stretching for an infinite time. To overcome this temporal aperture limitation, a number of time demultiplexing schemes have been developed [1,3]. Figure 3 shows a schematic of such an implementation that utilizes a cw multiwavelength source and phase modulation. In this system, a set of optical pulse trains, with each set at a different central wavelength, is generated by electro-optic phase modulation and dispersion as before. However, after intensity modulation, a wavelength division demultiplexing component is used to separate pulse streams by central wavelength into different branches. At the end of each branch, photodetection and electronic ADC sample the pulse stream. The sampling rate of these electronics need only correspond to the repetition rate of each pulse train, which is equivalent to the phase modulation frequency.

The sampled values from the various branches are then combined digitally to reconstruct the original high-frequency waveform. To obtain these data in our experimental setup, each laser was turned on and off in succession without the second stage of dispersion in the system. This mimics the data that would be obtained in each branch if a WDM were used and ADC electronics were placed in each branch.

The sampled pulses corresponding to different wavelength streams are shown superimposed in Fig. 4. We see that the pulses reconstruct the original 38 GHz waveform under test (dark curve). Application of the photonic ADC analysis given by Valley [1] indicates an ADC quantization of 2.5 effective number of bits (ENOB), which can be increased by the addition of optical and electrical gain in this system. Ultimately, this system is subject to the same fundamental limitations on ENOB (≈ 10 bits for moderate optical power levels between 10 and 100 mW) as described by Valley.

Only a portion of the waveform was obtained because only four different pulses exist owing to the use of only four cw lasers. Since the pulse spacing among pulses of different wavelengths is approximately $\Delta\tau = 7\ \text{ps}$, and the repetition period for a pulse stream of a given wavelength is $1/8.95\ \text{GHz} = 112\ \text{ps}$, approximately 15 branches would be needed to create a

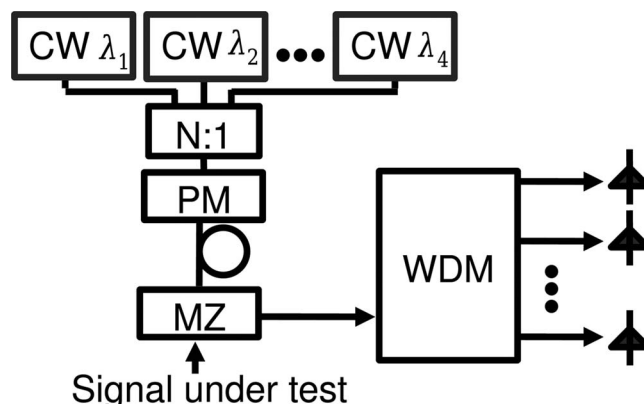


Fig. 3. Extension of the above concept to continuous time photonic ADC.

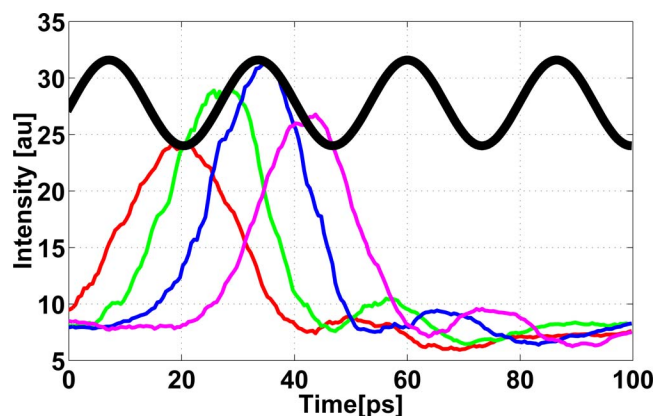


Fig. 4. (Color online) Sampled pulses superimposed onto one trace. The pulse streams corresponding to different central wavelengths are shown in different colors and reconstruct the original 38 GHz waveform under test (dark curve).

multiwavelength pulse stream for continuous time operation. This is practically feasible since laser banks consisting of tens of wavelengths are commercially available owing to the use of such laser banks in present-day WDM optical networks.

The highest sampling frequency achievable is mainly determined by the pulse spacing. To the first order, the pulses right after sampling should be no closer than half their width, determined by the approximation $\tau_{\min} \approx 0.7/2\delta f_m$, where the modulation index $\delta = \pi(V_a/V_\pi)$ and V_a is the amplitude of the phase modulating waveform [4]. Typically, the frequency of modulation f_m is limited to the detection speed of the electronic ADC (approximately ~ 20 GHz using present-day technology). In the systems above, a modulation index of $\delta = \pi$ and a driving frequency of $f_m = 8.95$ GHz were used, corresponding to $\tau_{\min} \approx 12$ ps in agreement with the autocorrelation mentioned above. Since each cycle of the SUT requires two samples, in accordance with the Nyquist sampling theorem, the above systems are capable of sampling electronic signals with a frequency content up to ~ 80 GHz. This is evident in Figs. 2 and 4, since a single cycle of the 38 GHz waveform is sampled by all four pulses.

A modest increase of phase modulation rf driving power to slightly below the damage threshold of the integrated LiNbO_3 phase modulator (approximately 1 W) yields a pulse width of ~ 5 ps, corresponding to a sampling frequency of 200 GHz. In addition, modulation depths of $\delta = 44$ rad using multiple-pass microwave resonant phase modulators have been previously achieved [5]. This type of modulation depth would correspond to a sampling frequency content exceeding 500 GHz. Additionally, in place of several lasers multiplexed together as employed above, a single multiwavelength source can be used instead. A number of easily implemented multiwavelength sources at the telecommunications wavelength of

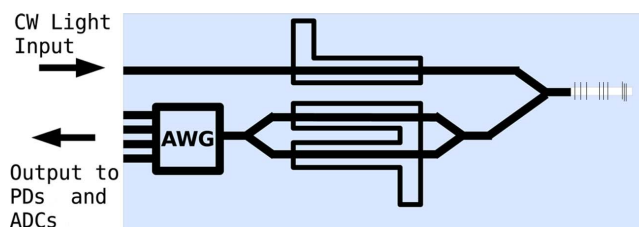


Fig. 5. (Color online) Potential monolithic implementation of the system described.

$1.55 \mu\text{m}$ with equal mode spacing and amplitude using an erbium-doped fiber have been recently proposed [6,7].

Furthermore, this system can be implemented on a single monolithic chip as illustrated in Fig. 5. A single cw laser source is first launched into an electro-optic phase modulator. The phase modulator is driven at the pulse repetition frequency, f_m , and a higher driving frequency. This higher driving frequency will create equally spaced frequency components in the spectral domain and hence act as the multiple laser lines that are spaced by $\Delta\lambda$ mentioned above. This signal is then launched into a dispersive element, such as a fiber Bragg grating that acts to create the pulse stream, similar to the first spool of dispersive fiber in the above system. Afterward, the pulse stream samples the SUT in the Mach-Zehnder modulator. Finally, a spatially dispersive element, such as an arrayed waveguide grating (AWG), routes pulses of different central wavelengths to separate ADC branches. The data obtained from the ADCs are then processed in the digital domain to reconstruct the sampled SUT. Such an implementation would make photonically assisted ADC of signals into the hundreds of gigahertz readily accessible in a compact and inexpensive integrated chip. This type of system, in both the integrated or discrete (such as those demonstrated above), offer a more simple and robust alternative to the conventional use of a mode-locked laser and fixed delay lines. This development can ultimately be employed for numerous applications, such as test and measurement and radar, where fast electrical waveforms need to be sampled in an easy and flexible manner.

References

1. G. C. Valley, *Opt. Express* **15**, 1955 (2007).
2. F. Coppinger, A. S. Bhushan, and B. Jalali, *IEEE Trans. Microwave Theory Tech.* **47**, 1309 (1999).
3. Y. Han, O. Boyraz, and B. Jalali, *Appl. Phys. Lett.* **87**, 24116 (2005).
4. T. Kobayashi, H. Yao, K. Amano, Y. Fukushima, A. Morimoto, and T. Sueta, *IEEE J. Quantum Electron.* **24**, 382 (1988).
5. A. Godil, B. Auld, and D. Bloom, *IEEE J. Quantum Electron.* **30**, 827 (1994).
6. S. Bennet, B. Cai, E. Burr, O. Gough, and A. J. Seeds, in *Optical Fiber Communication Conference*, OSA Technical Digest Series (Optical Society of America, 1999), p. 208.
7. M. P. Fok and C. Shu, *Opt. Express* **14**, 2618 (2006).

Distortion Comparison of Single-Sideband Coherent Analog Optical Links Employing X-Cut and Z-Cut Mach–Zehnder Modulators

Guanghao Zhu, Bart Bortnik, *Student Member, IEEE*, Wei Liu, Harold R. Fetterman, *Fellow, IEEE*, Richard Forber, *Member, IEEE*, and Wen C. Wang

Abstract—A single-sideband coherent analog optical link is implemented using a null-biased Mach–Zehnder (MZ) intensity modulator followed by a narrowband optical bandpass filter. The fidelity performance of such a link is compared between cases with X-cut and Z-cut MZ LiNbO₃ modulators. It is shown that for the case of Z-cut modulators, the converted radio-frequency output contains higher nonlinear distortions. Under the same operating condition, the spurious-free dynamic range of an X-cut link outperforms that of a Z-cut link by 2.6 dB.

Index Terms—Coherent optical link, electrooptic modulation, intermodulation distortion, suppressed carrier.

I. INTRODUCTION

MOST of the analog optical links [1] installed to date are designed to operate in the intensity-modulation and direct-detection mode owing to its ease of implementation. When a LiNbO₃ Mach–Zehnder (MZ) intensity modulator [2] is chosen for this type of link as the signal encoder, it is often true that the static modulator bias is set at the quadrature point in order to maximize the linear signal gain and null the second-order nonlinear distortion at the same time. In addition, it is also often desirable to use high optical power at the modulator input port, to obtain better link performance.

One serious drawback that is intrinsically associated with the quadrature bias and high optical input power is the large component of the unsuppressed optical carrier presented at the modulator output port. The strong residue carrier component will lead to several problems such as limited transmission distance set by the fiber Kerr-nonlinearity [3], and photocurrent nonlinear distortion set by the photodiode small illumination area [4]. These problems can be alleviated using the concept of carrier suppression with the additional benefit of improved spurious-free dynamic range (SFDR) [5], [6]. Experimentally, carrier suppression has been demonstrated using either a low-biased MZ modulator [5], or a quadrature-biased MZ modulator followed by an optical notch filter [7].

An alternative approach that takes the advantage of the concept of a coherent link is to generate a single-sideband (SS) optical

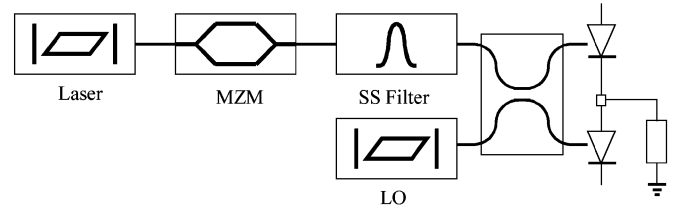


Fig. 1. Schematic of the SS coherent analog optical link. MZM: Mach–Zehnder modulator biased at null. SS Filter: optical bandpass filter that selects only one of the sidebands. LO: local oscillator derived from the input laser. Balanced detection scheme is used.

signal for transmission at the transmitter end and use a local oscillator (LO) for coherent detection at the receiver end [8], [9]. By generating an SS signal, the carrier is suppressed and the nonlinearity related problems can be eliminated. Note that when compared with the low-bias link, although the SS coherent detection link complicates the system implementation, the potential applications can still benefit from several unique advantages including the cancellation of nearly maximized second-order distortion, the removal of the strong SFDR sensitivity on the modulator bias, and the integratability with a balanced detection scheme for better signal-to-noise ratio and a factor of two enhancement of the maximum power handling capacity.

We report here a study of the effect of MZ modulator waveguide layout (X-cut or Z-cut) on the fidelity performance of SS coherent analog link. The major distortion considered in this work is the third-order intermodulation (IMD3) which exists persistently with the signal inside the same band. We show that other than the low-bias direct-detection case [5], [6], when an SS coherent-detection scheme is used [8], [9], X-cut MZ modulators exhibit advantages in terms of achieving higher SFDR values. In general, the state of the art design of the Z-cut modulator gives about 1 dB less insertion loss and about 2 dB higher electrooptic response than the X-cut one [2].

II. LINK ANALYSIS

A schematic of our SS coherent optical link is illustrated in Fig. 1. The output of a continuous-wave laser is connected to the input of an MZ intensity modulator. The MZ modulator is statically biased at the null position in order to maximize the optical power of the first-order sidebands and minimize the optical power of the input carrier. The suppressed-carrier double-sideband output is sent to an optical bandpass filter to select out only one of the first-order sidebands and reject all the others. The generated SS signal is combined with an LO at the receiver

Manuscript received January 31, 2008; revised May 8, 2008. This work was supported in part by the U.S. Navy under Contract N00014-05-M-0240.

G. Zhu, B. Bortnik, W. Liu, and H. R. Fetterman are with the Electrical Engineering Department, University of California, Los Angeles, CA 90095 USA (e-mail: fetter@ee.ucla.edu).

R. Forber and W. C. Wang are with IPITEK Inc., Carlsbad, CA 92008 USA. Digital Object Identifier 10.1109/LPT.2008.927911



Fig. 2. Waveguide layout of an (a) X-cut and a (b) Z-cut MZ modulator.

end through a 3-dB coupler. Note that in this work the LO is derived from the input laser and thus our coherent link is homodyne based. Balanced detection is used to maximize the converted radio-frequency (RF) signal and to cancel the laser relative intensity noise and other distortions.

We start our analysis by first examining the output field of a null-biased MZ modulator with frequency chirp effect being included. The frequency chirp effect is related to the symmetry consideration of the modulator waveguide layout. As we show in Fig. 2, for the case of X-cut MZ modulators, due to the even nature of the waveguide arrangement, the modulation depths experienced by the two MZ arms are equal. However, for the case of Z-cut MZ modulators, the broken balance between the left and right arms leads to unequal modulation responses. In general, the modulation depth difference can be characterized using the frequency chirp parameter α defined as $\alpha = (m_1 - m_2)/(m_1 + m_2)$, where m_1 and m_2 represent the absolute value of modulation depth of MZ arm 1 and 2, respectively. For X-cut modulators $\alpha \approx 0$ and for Z-cut modulators $\alpha \approx 0.7$ [2].

Denoting the MZ modulator input power as P_0 , the common-mode modulation depth as $m = (m_1 + m_2)/2$, and the modulation frequency as ω_m , the slow-varying amplitude of a null-biased MZ modulator with symmetric Y-splits reads

$$A = \frac{\sqrt{P_0}}{2} \sum_{n=-\infty}^{+\infty} \{J_n[(1+\alpha)m] - J_n[-(1-\alpha)m]\} \cdot e^{in\omega_m t + i\frac{n\pi}{2}}. \quad (1)$$

Using the identity $J_n(x) = J_n(-x)$ which holds for even n , one finds that for null-biased Z-cut modulators (nonzero chirp parameter α), the carrier and even order sidebands will not be perfectly cancelled once the modulation is turned ON, i.e., when $m \neq 0$. There will be, however, complete cancellation in the case of the X-cut modulator.

The SS optical signal is then generated by selecting out only the +1st-order sideband of (1) using a narrowband filter with an insertion loss of γ . This SS signal is further combined with an LO signal with optical power P_{LO} through a 3-dB coupler to give a slow-varying envelop

$$\begin{aligned} A_{\pm} &\approx \frac{\sqrt{2P_{LO}}}{2} e^{\pm i\frac{\pi}{2}} + \frac{\sqrt{2\gamma P_0}}{4} \\ &\times \{J_1[(1+\alpha)m] + J_1[(1-\alpha)m]\} e^{i\omega_m t} \\ &\approx \frac{\sqrt{2P_{LO}}}{2} e^{\pm i\frac{\pi}{2}} + \frac{\sqrt{2\gamma P_0}}{4} \\ &\times \left(m - \frac{(1+3\alpha^2)m^3}{8} \right) \cdot e^{i\omega_m t} \end{aligned} \quad (2)$$

where the subscripts \pm refer to the amplitude seen by the two detectors shown in Fig. 1 respectively. From (2), it is evident that

a Z-cut link has more third-order optical nonlinear product (the m^3 term) than that of an X-cut link. This increased third-order optical nonlinear component of a Z-cut link will then give rise to larger IMD3 in the RF domain.

To analyze the IMD3 performance of our coherent link, we apply the technique of the two-tone test. Following the standard procedures [1], the signal power P_{RF} and IMD3 power P_{IMD3} after balanced detection are calculated as

$$P_{RF} = \frac{1}{2} \cdot \eta^2 R \cdot \gamma P_0 P_{LO} \cdot m^2 \quad (3)$$

$$P_{IMD3} = \frac{(1+3\alpha^2)^2}{128} \cdot \eta^2 R \cdot \gamma P_0 P_{LO} \cdot m^6 \quad (4)$$

where η is the photodiode conversion efficiency and R is the photodiode load resistance.

We are thus led to the main conclusion drawn from this work: for SS coherent optical analog links, the RF IMD3 power of a Z-cut is approximately 7.9 dB higher (calculated using $\alpha = 0.7$) than that of an X-cut. As a result, the SFDR of a Z-cut link will be 2.6 dB worse than that of an X-cut link, assuming all the other conditions are the same.

III. EXPERIMENTAL RESULTS

Experiments were conducted to verify the analysis outlined in the previous section. The setup is shown in Fig. 1. A narrow linewidth 1550-nm semiconductor laser was used as the light source of the coherent link. An erbium-doped fiber amplifier was employed to boost the power to ~ 100 mW before the MZ modulator. Two LiNbO₃ MZ modulators were tested in the setup as the optical signal generator, of which one is X-cut and the other is Z-cut. The X-cut modulator has an insertion loss of 3.1 dB and an RFV_{π} of 4.5 V while the Z-cut modulator has an insertion loss of 2.0 dB and an RFV_{π} of 4.4 V. (Note that the specification differences were compensated in all the following experiments by applying different optical and RF power into the modulators.) To generate the SS signal, an optical bandpass filter (insertion loss 6 dB) was used to select the upper ($n = +1$) sideband. The optical bandpass filter has a full-width at half-maximum of 1 GHz and an SS suppression ratio of 40 dB if the baseline modulation frequency is chosen around 10 GHz.

At the receiver end, the LO signal is generated by tapping out a fraction percent of the light from the amplifier output. The narrow linewidth (< 200 kHz) of the light source and the short path length difference (< 5 m) guarantees an excellent coherent relationship between the SS signal and LO signal. A balanced photodetector was used to convert light into current. To maximize the beating signal, a polarization controller was placed before the 3-dB coupler.

Optical spectrum of null-biased X-cut and Z-cut modulators were first measured. The results were plotted in Fig. 3. It can be seen that when the RF modulation is turned ON, a Z-cut modulator generates higher even order sidebands than an X-cut and the optical carrier is no longer well suppressed. This is a result caused by Z-cut's nonzero frequency chirp parameter α as predicted by (1). Note that the incomplete suppression of the optical carrier without RF modulation is due to the finite MZM extinction ratio (> 40 dB), and has negligible effect on the link performance when balanced detection (common-mode subtraction) is

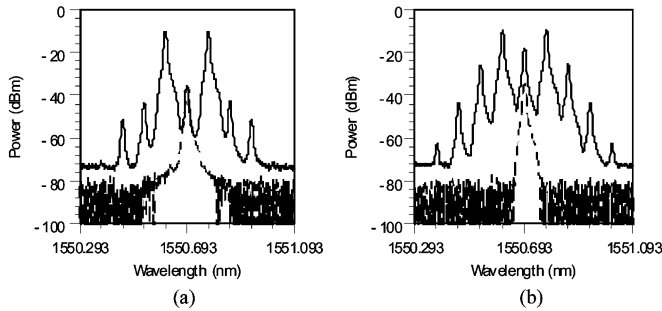


Fig. 3. Measured optical spectrum of (a) a null-biased X-cut modulator and (b) Z-cut modulator. Solid line corresponds to the case with RF modulation. Dashed line corresponds to the case without RF modulation.

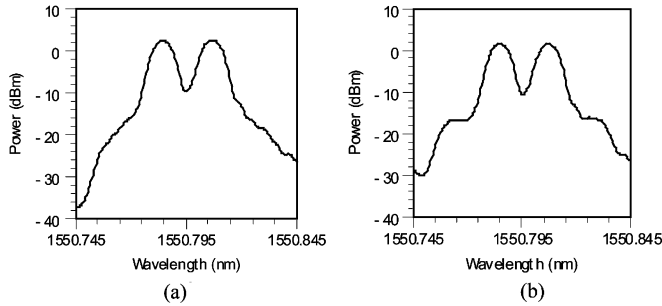


Fig. 4. Measured optical spectrum of SS ($n = +1$) signal employing (a) X-cut modulator and (b) Z-cut modulator with two-tone modulation. The frequency of the two tones were 10 and 13 GHz, respectively.

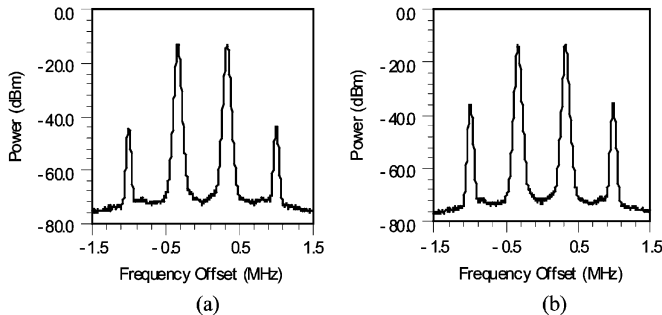


Fig. 5. Measured RF spectrum of SS coherent optical link employing (a) X-cut modulator and (b) Z-cut modulator with two-tone modulation. The zero on the x-axis corresponds to 10 GHz (average frequency of the two tones).

used. By carefully fitting Fig. 3 using (1), the α parameter of the Z-cut modulator is determined to be 0.72.

Two-tone measurements were subsequently carried out to investigate the link fidelity performance. In Fig. 4, we plot the optical spectrum of the first-order ($n = +1$) sidebands of the X-cut and Z-cut modulator when the two-tone signal is applied. It is clear that the Z-cut modulator generates more IMD3 power in the optical domain. However, limited by the optical spectrum analyzer resolution (0.01 nm), the IMD3 difference cannot be quantitatively determined using optical measurements from Fig. 4. This difficulty can be overcome by converting the light into current. As we show in Fig. 5, the IMD3 power differs by

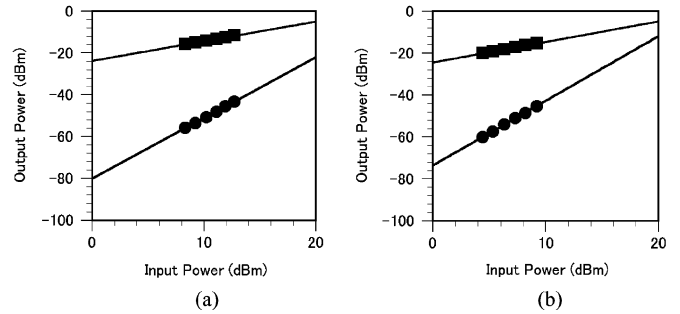


Fig. 6. Fundamental and IMD3 RF power as a function of input RF power for SS coherent optical link employing (a) X-cut modulator and (b) Z-cut modulator measured at 10 GHz. Solid square: signal power. Solid circle: IMD3 power.

approximately 8.4 dB, in good agreement with the theoretical predication of 7.9 dB.

SFDR was measured by averaging over multiple sets of RF data points collected with X-cut and Z-cut modulators. The results are summarized in Fig. 6. The LO current was fixed at 2 mA for each balanced detection photodiode. This gives a shot-noise limited noise floor of -168 dBm/Hz seen by the RF spectrum analyzer. The measured SFDR for the X-cut and Z-cut SS coherent link are 114.4 and 111.6 dB \cdot Hz $^{2/3}$ respectively, revealing a 2.8-dB difference obtained experimentally.

IV. CONCLUSION

We have shown that for the SS coherent optical link, the waveguide layout structure of the MZ modulator is crucial in determining the link fidelity performance. Specifically, an X-cut modulator link gives 2.6-dB SFDR improvement over a Z-cut link and, therefore, is the preferred choice for high SFDR operation.

REFERENCES

- [1] C. H. Cox III, *Analog Optical Links Theory and Practice*. Cambridge, UK: Cambridge Univ. Press, 2004.
- [2] E. L. Wooten, K. M. Kissa, A. Yi-Yan, E. J. Murphy, D. A. Lafaw, P. F. Hallemeier, D. Maack, D. V. Attanasio, D. J. Fritz, G. J. McBrien, and D. E. Bossi, "A review of lithium niobate modulators for fiber-optic communications systems," *IEEE J. Sel. Topics Quantum Electron.*, vol. 6, no. 1, pp. 69–82, Jan./Feb. 2000.
- [3] C. Y. Kuo, "Fundamental nonlinear distortion in analog links with optical amplifiers," *J. Lightw. Technol.*, vol. 1, no. 1, pp. 7–15, Jan. 1993.
- [4] K. J. Williams, R. D. Esman, and M. Dagenais, "Nonlinearities in P-I-N microwave photodetectors," *J. Lightw. Technol.*, vol. 14, no. 1, pp. 84–96, Jan. 1996.
- [5] M. L. Farwell, W. S. C. Chang, and D. R. Huber, "Increased linear dynamic range by low biasing the Mach-Zehnder modulator," *IEEE Photon. Technol. Lett.*, vol. 5, no. 7, pp. 779–781, Jul. 1993.
- [6] E. Ackerman, S. Wanuga, D. Kasemset, A. S. Daryoush, and N. R. Samant, "Maximum dynamic range operation of a microwave external modulation fiber-optic link," *IEEE Trans. Microw. Theory Tech.*, vol. 41, no. 8, pp. 1299–1306, Aug. 1993.
- [7] M. J. LaGasse, W. Charczenko, M. C. Hamilton, and S. Thaniyavarn, "Optical carrier filtering for high dynamic range fiber optic links," *Electron. Lett.*, vol. 30, pp. 2157–2158, 1994.
- [8] G. E. Betts, "High dynamic range coherent analog links using AM SSB," in *Proc. 17th Annu. Conf. LEOS Puerto Rico*, 2004, pp. 130–131.
- [9] Y. C. Hung, B. Bortnik, H. R. Fetterman, R. Forber, and W. Wang, "Suppressed carrier optical transmitter with intracavity modulation for coherent analog optical links," in *Proc. OFC/NFOEC 2007*, Anaheim, CA, 2007, Paper JWA6.

Optical Signal Processor Using Electro-Optic Polymer Waveguides

Byoung-Joon Seo, Seongku Kim, Bart Bortnik, Harold Fetterman, *Fellow, IEEE*, Dan Jin, and Raluca Dinu

Abstract—We have investigated an optical signal processor using electro-optic polymer waveguides operating at a wavelength of 1.55 μm . Due to recent developments, many useful optical devices have become available such as optical filters, modulators, switches, and multiplexers. It will be useful to have a single optical device, which is reconfigurable to implement all of these functions. We call such a device an “optical signal processor,” which will play a similar role to digital signal processors in electrical circuits. We realize such an optical device in a planar lightwave circuit. Since the planar lightwave circuits are based on the multiple interference of coherent light and can be integrated with significant complexity, they have been implemented for various purposes of optical processing such as optical filters. However, their guiding waveguides are mostly passive, and the only viable mechanism to reconfigure their functions is thermal effects, which is slow and cannot be used for high-speed applications such as optical modulators or optical packet switches. On the other hand, electro-optic polymer has a very high electro-optic coefficient and a good velocity match between electrical and optical signals, thus, permitting the creation of high-speed optical devices with high efficiency. Therefore, we have implemented a planar lightwave circuit using the electro-optic polymer waveguides. As a result, the structure is complex enough to generate arbitrary functions and fast enough to obtain high data rates. Using the optical signal processor, we investigate interesting applications including arbitrary waveform generators.

Index Terms—Electrooptic waveguides, optical filter, optical signal processor (OSP), ring resonator.

I. INTRODUCTION

THE structure and features of the investigated optical signal processor (OSP) are based on *optical delay line circuits* or *planar lightwave circuits* (PLC) in a more general term. Optical delay line circuits have been intensively studied for last few decades. A number of different structures have been proposed and demonstrated both theoretically and experimentally with many useful applications such as optical filters [1]–[5], multi/demultiplexers used in wavelength division multiplexing (WDM) systems [6], dispersion compensators [2], [7], pulse code generators [8], and convolution calculators [8].

Manuscript received November 09, 2007; revised June 26, 2008. First published April 17, 2009; current version published July 09, 2009. This work was supported in part by the Air Force Office of Scientific Research and by the Defense Advanced Research Projects Agency MORPH Program.

B. Seo was with the Department of Electrical Engineering, University of California, Los Angeles, CA 90095 USA. He is now with Jet Propulsion Laboratory, Pasadena, CA 91109 USA (e-mail: Byoung-Joon.Seo@jpl.nasa.gov).

S. Kim, B. Bortnik, and H. Fetterman are with the Department of Electrical Engineering, University of California, Los Angeles, CA 90095 USA.

D. Jin and R. Dinu are with Lumera Corporation, Bothell, WA 98041 USA. Digital Object Identifier 10.1109/JLT.2008.2005916

In early days of optical delay line circuit research, optical fiber was widely used as an optical signal delay line medium because of its low loss and low dispersion characteristics [8]. However, the optical signals using optical fibers are mostly treated as incoherent, because it is difficult to adjust the lengths of the optical delay lines with wavelength order accuracy. The shortest delay line has to be longer than the coherent length of the optical source. The signal processing dealing with incoherent optical signals has only positive coupling coefficients because only optical power coupling is considered [9], [10]. As a consequence, its applications are limited. For example, the transfer functions that can be implemented with only positive coefficients are very limited and only allow the realization of low-pass filters [9].

To overcome this limitation and have negative coefficients, several methods have been proposed. Some use optical amplifiers [9], while others use a differential photo-detection scheme [10]. Among these solutions, one of the most promising and effective ways to have negative coefficients is using coherent interference in optical waveguides. Optical delay line circuits using coherent interference utilize optical phase as well as optical power, and hence can express arbitrary coefficients. This enables the processing of signals in a more general way. Furthermore, optical delay line circuits based on optical waveguides are intrinsically smaller than using fibers. In addition, the delay length can be precisely determined so that it can effectively handle high-speed broadband signals. Optical signals processed in waveguide result in more stable operation since they are less sensitive to external perturbation.

Considerable amount of work using optical waveguides has been done to implement optical delay line circuits. Most of them use silica-based waveguides [6], [11]–[14]. The advantages of silica-based waveguide circuits include low propagation loss (0.01 dB/cm), good fiber coupling loss (0.1 dB for low index contrast waveguides), and ease of defining complex structures such as AWGs and Mach–Zehnder arrays. However, they are basically passive structures. The only viable phase control mechanism intrinsically available is the thermo-optic modulation of the index, which is slow ($< \text{few MHz}$) and inconvenient. Because of their slow modulation characteristic, an optical delay line circuit with silica-based waveguides cannot be used for high-speed operations such as modulators and optical packet switches.

On the other hand, the electrooptic polymer is an excellent electrooptic material with a high Pockels' coefficient and has a good optical/microwave velocity match. The capability of the materials has already been demonstrated for a period of years implementing high-speed amplitude modulators and phase modulators with low half-wave voltages, a digital optical switch, and more complex devices such as photonic radio frequency phase shifters [15]–[20]. In addition to generating

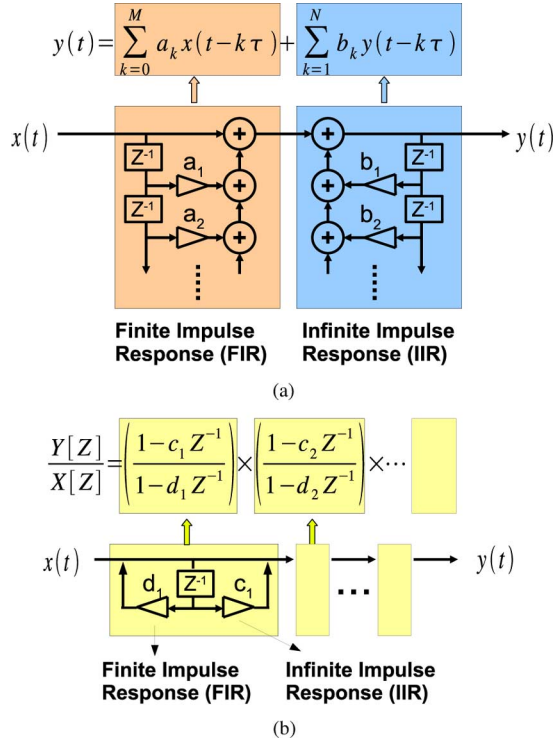


Fig. 1. Example block diagrams of OSP circuits. The input is split into multiple waveguides. The individual optical signal experiences equally different time delays represented by Z^{-1} , and amplitude and phase changes represented by the a_k , b_k , c_k , and d_k coefficients. At the output port, they are combined again to generate an output signal. (a) Transverse form. (b) Lattice form.

arbitrary and complex functionality by employing PLC structures, use of the electrooptic polymer OSP permits operation at high speed. Therefore, not only an electrooptic polymer OSP can be used for the same applications as a PLC, but the OSP is also well suited for high-speed devices and applications.

II. OSP THEORY

The fundamental enabling concept of the OSP stems from the multiple and temporal interference of delayed optical signals. By controlling the amplitude and the phase of the interfered signals, the optical signal can be processed in any arbitrary way. Example block diagrams of OSP circuits are shown in Fig. 1. The input optical signal is launched on the left side and split into multiple waveguides. The individual optical signal experiences equally different time delays represented by τ and Z^{-1} in the diagrams, and amplitude and phase changes represented by the a_k , b_k , c_k , and d_k coefficients. At the output port located on the right side of the diagram, they are combined again to generate an output signal.

Two typical configuration structures are distinguished; *transversal form* [21] and *lattice form* [4], [5] as can be seen in Fig. 1(a) and (b), respectively. The transversal form is a parallel structure since the signal is processed in a parallel way, while the lattice form is a serial structure where signals are processed in series. If we define a waveguide branch *arm*, an arm can be classified into two types: forward feeding arm and backward feeding arm. Since the response of forward feeding arms is finite in time, it is called finite impulse response (FIR). In a

similar way, the response of backward feeding arms is called infinite impulse response (IIR) since it is infinite. The number of the forward feeding arms and of backward feeding arms represent the order of FIR and IIR, respectively. The origin of this terminology is from the digital filter theory in electronics [22]. According to this theory, any arbitrarily response can be obtained when FIR and IIR are combined together. The order of FIR and IIR is associated with how arbitrary an OSP can describe the response.

Several physical values are important for characterizing an OSP. These are the unit delay time, τ , and the number of arms that split or combine light (N and M in Fig. 1(a)). The unit delay time of an OSP is analogous to the sampling time in discrete time signal processing. It represents a time resolution for the OSP to process a signal. Due to this time resolution, the frequency response of an OSP is periodic and the period is proportional to $1/\tau$. This period is called the free spectral range (FSR). The number of optical splitting and combining arms determines the spectral resolution of the OSP within an FSR. As the number of arms increases, a sharper frequency response can be obtained and hence a more arbitrary response is possible. In that sense, it is analogous to the number of eigenfunctions in the frequency domain because the overall frequency response of an OSP is a response combination of the individual arms.

If $x(t)$ and $y(t)$ denote the input and output signal, respectively, an OSP performs as an operator to transform $x(t)$ into $y(t)$. Several modes can be used for describing an OSP. The first method is to use a characteristic equation, already shown in Fig. 1(a). If an OSP has the M number of forward feeding arms and the N number of backward feeding arms, the characteristic equation of the processor can be generally written as (1)

$$y(t) - \sum_{n=1}^N b_n y(t - n\tau) = \sum_{m=0}^M a_m x(t - m\tau) \quad (1)$$

where the coefficients, a_m and b_n , stand for the amplitude and phase changes of the m th forward feeding arm and the n th backward feeding arm, respectively. The coefficients are complex values in general because the signals, $x(t)$ and $y(t)$, stand for coherent optical fields, and thus have both amplitude and phase. The amplitude and the phase of a coefficient correspond to the amplitude and phase change of an individual signal.

The second method for describing this system is the transfer function representation. In general, the coefficients, a_m and b_n , and the delay time, τ , in (1) can be functions of time as well if we change (or modulate) those parameters in time. If their varying rate is comparable to that of the optical signal such as in electrooptic polymer waveguides, their time-dependent effect must be considered. We sometimes apply time-varying signals to the time-delay lines to effectively change τ in our experiments in Section VI. However, we assume that the time-varying rate is small enough or the *delay control mode* (defined later in this section) is only considered in the OSP operation in this paper. In this case, the OSP becomes a linear system and is similar to the digital filter in many ways. Indeed, the OSP has the same transmission characteristics and features as those of a corresponding digital filter. Therefore, the conventional Z transform analysis, which is frequently used with digital filters, can be applied to

the analysis of the OSP. In Z transformation, the transfer function is represented as the rational functions of Z .

If we calculate the Fourier transformation of (1) with respect to the eigenfunctions of $e^{jp\omega\tau}$, where p is any integer and ω is the optical angular frequency and replace the $e^{-j\omega\tau}$ with Z^{-1} , we obtain the transfer function, $H(Z)$, in the Z domain

$$H(Z) = \frac{\sum_{m=0}^M a_m Z^{-m}}{1 - \sum_{n=1}^N b_n Z^{-n}} \quad (2)$$

where $Z^{-1} (= e^{-j\omega\tau})$ stands for one unit delay in the Z domain.

Another convenient and more visual way to describe an OSP is to use a pole/zero diagram [23]. Because the transfer function, $H(Z)$, is a complex function of the complex variable, Z , the value of $H(Z)$ can be plotted on the complex Z space. The zeros are the Z values which make $H(Z) = 0$, and the poles are the ones that make $|H(Z)| = \infty$. Then, another form of $H(Z)$ can be written as

$$H(Z) = A \frac{\prod_{i=1}^M (1 - \rho_i Z^{-1})}{\prod_{j=1}^N (1 - \gamma_j Z^{-1})} \quad (3)$$

where ρ_i and γ_j are the i th zero and j th pole, and A is the amplitude factor.

In general, the coefficients, a_m and b_n , and the delay time, τ , in (1) can be functions of time as well as the input light signal. Three different methods are possible to operate the OSP, depending on which parameters are used for optical processing. They are the *coefficient control mode*, *delay control mode*, and *frequency control mode*.

The *coefficient control mode* performs optical processing via controlling the coefficients, a_m or b_n . When a typical continuous wavelength light is input, the output light can be processed by modulating or controlling these coefficients. The *delay control mode* is via controlling the delay time, τ . For a continuous or varying wavelength light input, the delay time can be controlled or modulated to generate processed output light. The *frequency control mode* utilizes frequency dependence of the OSP due to its delay lines.

Most PLC structures using silica waveguides regard the coefficients and the delay time as constant variables, since their controlling method (mostly thermal tuning) is much slower than the optical light signal. Therefore, the silica waveguides mostly use the *frequency control mode* for their optical signal processing, such as in optical filters [2], [7], [21]. However, if the time-varying or modulating rate of the coefficients or the delay time is comparable to the propagation of the optical signal through the OSP, such as in electrooptic polymer waveguides, their time-dependent effect will be useful and should be considered.

We investigate the OSP applications using the *delay control mode* rather than the *frequency control mode* or the *coefficients control mode* when we discuss its applications in Section VI. If the *frequency control mode* is used in an OSP with the electrooptic polymer waveguides, the OSP can tune such optical filters much faster. However, the filter performance will be limited if electrooptic polymers are used in place of silica waveguides due to its intrinsic optical loss. Furthermore, operating our polymer OSP in the *coefficients control mode* is not particularly interesting. The OSP we investigate is classified into the

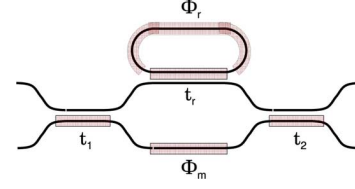


Fig. 2. Unit block of OSP. It is a two-port input and two-port output system consisting of a symmetric Mach-Zehnder interferometer and a racetrack structure. Four electrodes control the locations of a zero and a pole.

lattice form the structure. In the lattice form structure, the c_k and d_k coefficients in Fig. 1(b) are complex functions of actual electrical biases, which makes it difficult to find the relationship between its output function and the electrical biases [4], [5]. In addition, we have not found any useful and unique applications using this mode partly because the optical loss in polymers limits the performance of the OSP building blocks.

One can find that the *frequency control mode* is based on the same principle as the *delay control mode*. In (2), the delay time τ and the optical frequency ω are multiplied together. Therefore, either affects the transfer function in the same way. We can change the delay time using the electrooptic effect with a fixed input optical frequency (wavelength) or the optical frequency can be changed using a fixed delay time. Either approach will generate the same output response. This is the basic concept for the *arbitrary waveform generator*, we investigate in Section VI, and it becomes clear with the driving formula of (5).

III. OSP DESIGN

A. Structure

Since multiple power splitting is hard to obtain and not effective in the optical waveguide, the lattice form structure is considered for the implementation of our OSP. The lattice form is a series structure with a certain type of a unit block. The unit block which we have chosen consists of a symmetric Mach-Zehnder interferometer and a racetrack waveguide as shown in Fig. 2. “Symmetric” means that the lengths of the two waveguide arms of the Mach-Zehnder interferometer are the same. A racetrack structure is used so that the straight waveguide section has an extended coupling region for coupling outside of the ring.

This unit block, originally proposed by Jinguji [5], has two input and two output ports. Any input port can be used for operation, while the two output ports are related to each other by a conjugate power relation. A conjugate power relation means that the total sum of two output powers is the same as the input power if the system is lossless.

This structure generates one zero and one pole simultaneously. The degree of freedom to locate a zero or a pole in the Z space is 2 because a zero or a pole is a complex value, and hence has both amplitude and phase. The locations of the zero and the pole in the Z space are controlled by the four different electrodes. Note that t_1 and t_2 are functionally redundant.

A multiple-block OSP consists of cascaded multiple unit blocks as shown in Fig. 3. With N cascades of unit blocks, our OSP can generate N zeros and pole pairs. Therefore, the degree of freedom of the N cascaded OSP is $N \times 4$, which are controlled by $N \times 4$ electrodes on top of the waveguides.

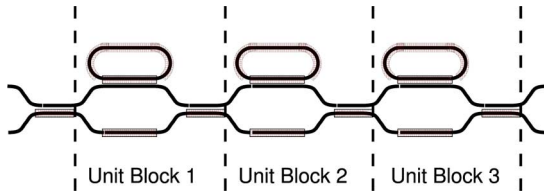


Fig. 3. Multiple structure of OSP. It consists of N cascaded unit blocks.

In the strict sense, the definition of the unit block in Fig. 2 is wrong if the multiple block is considered. It should be one of the divided sections in Fig. 3 except the first block, which is just a configurable coupler. To avoid confusion, we name the structure in Fig. 2 as a “one-block OSP” and one of the divided sections in Fig. 3 as a “unit block.”

The unit block contains two configurable couplers and two phase shifters. They are the “splitting coupler,” the “racetrack coupler,” the “Mach–Zehnder phase shifter,” and the “racetrack phase shifter,” labeled as t_1 , t_r , ϕ_m , and ϕ_r , respectively, shown in Fig. 2. They are used for configuring one zero and one pole generated by a unit block and controlled by microstrip electrodes located on top of the waveguides via the electrooptic effect.

In order to have a useful phase shift at the racetrack phase shifter, the perimeter of the racetrack must be large enough. On the other hand, the round trip loss of the racetrack will be too large if the perimeter is large. Therefore, we design the radius of the racetrack to be 1.2 mm. The interaction lengths of the racetrack coupler and the splitting coupler are designed as 2 mm and 6 mm, respectively. The detail design parameters of the individual building blocks or components are discussed later in this section.

B. Optical Waveguides and Fabrication

The optical waveguide is a crucial part of the OSP. While confining the light inside, it is the basis of the delay lines and couplers. We need to consider two requirements when selecting the type and dimensions of the waveguides. First, they should be highly confined waveguides because of the bending structure in the racetrack. Second, their confinement is low enough so that a reasonable amount of energy can be coupled. Note that these two factors are competing against each other. Furthermore, the waveguides should also be of single mode to ensure no signal degradation occurs via modal dispersion.

For the electrooptic polymer core material, DH6/APC (Lumera Co.) was used. Single-layer films of DH6/APC have shown a high electrooptic coefficient r_{33} of 70 pm/V at 1.31 μm [24]. For lower and upper cladding polymers, UV15LV (Master Bond Co.) and UFC170A (Uray Co.) are used. The indexes at 1.55 μm of the core are measured to be 1.61, and the lower and upper claddings have been measured to be 1.51 and 1.49, respectively [25].

We consider the inverted rib waveguide structure, which is known to be effective in minimizing the scattering loss from sidewall roughness [26]. Fig. 4 shows the cross section of the designed waveguides at a coupler region. The rib width, rib height, and slab thickness are designed to be 2 μm , 1 μm , and 1 μm , respectively. Using the known indexes of the polymer material,

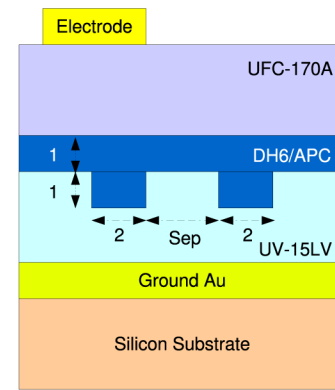


Fig. 4. Cross section of the designed optical waveguide. It is a single-mode waveguide whose confinement is high enough to support a 1 mm radius bending yet low enough to be coupled to an adjacent waveguide.

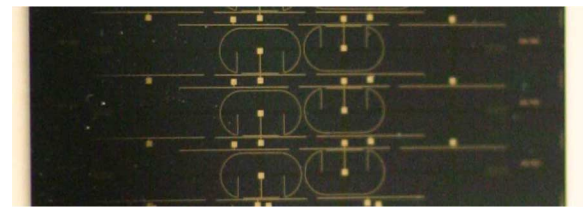


Fig. 5. Top view photograph of fabricated devices. The bright yellow regions are where the driving electrodes are located. The rectangular shape electrodes are DC pads for electric connections using DC contact probes.

we numerically calculate the propagation modes, optical coupling, and bending loss for this optical waveguide structures and find that this waveguide can support 1 μm bending with negligible bending loss and yet can couple effectively to an adjacent waveguide. Similar waveguide structures using similar polymer materials are also used in [27], where bending waveguides with a 1 mm bending radius have a loss of approximately 4 dB/cm at 1.3 μm . Optical waveguide modes were simulated by a commercial software package, Fimmwave (Photo Design Inc.). Both numerical simulations and experiment show that this waveguide supports a single mode.

Fig. 5 shows the top view photograph of the fabricated device. The bright regions (yellow if colored) are where the driving electrodes are located. The rectangular shape electrodes are DC pads for electric connections by DC contact probes. Note that high-frequency design features are not considered in this work.

C. Waveguide Bending

There are three different optical loss mechanism in optical waveguides: material loss, scattering loss, and bending loss. Material loss is power loss absorbed inside the material due to absorptions and imperfections in the bulk waveguiding material. Scattering loss is due to imperfect surface roughness scattering at the interface of the core and cladding in both straight and curved waveguides. Bending loss is power leakage when the waveguide is bent and primarily determined by the waveguide confinement factor.

In calculating the bending loss of a bending waveguides, several approaches have been used. Yamamoto and Koshiba [28], used the *finite element method* (FEM) for the computational window of the bending waveguides and found the steady

state solution of an outgoing leaky wave, where the leaky wave was depicted by the Henkel function of the second kind [28]. Even though this method calculates a very rigorous solution, the computation time can be long due to recursive iterations. The *perfectly matched layer* (PML) has also been used for calculating the bending loss [29]. The advantages of the PML method include that the formulation is based on Maxwell's equations rather than a modified set of equations, and that the application to the *finite difference time domain* (FDTD) method is more computationally efficient, and that it can be extended to nonorthogonal and unstructured grid techniques. However, it is difficult and critical to find a perfectly matched layer boundary condition.

We use the *finite different method* (FDM) and *conformal transformation technique* [30] in order to find the optimal radius and the bending loss of the bending waveguide. The zero boundary condition is assumed for all the boundaries except the leaky side of the waveguide (where the energy is leaking). In the leaky side, we apply a *plane-wave boundary condition* [31]. As a result, we calculate the bending loss as 0.02 dB/cm when the bending radius is 1 mm. This bending loss is much smaller than the propagation loss of the straight waveguide. Therefore, we ignore the bending loss if the bending radius is larger than 1 mm.

D. Configurable Couplers

The cross section of the configurable couplers is shown in Fig. 4. The waveguides are located sep distance apart. The energies carried by the two waveguides are coupled to each other. The driving electrode on top of only one waveguide applies an electric field to change the refractive index of the waveguide and to tune the amount of coupling. In order to optimize the operation of the configurable couplers, the waveguide separation and their interaction length should be designed properly.

We have utilized the change in the velocity match for the coupling mechanism rather than the change in the overlap of the modes. By a change in the index due to the applied electric field, both effects will influence the coupling coefficients. The refractive index of the electrooptic core material used is around 1.6, and its maximum index change, we have utilized in this work, is around 1×10^{-4} . Using numerical waveguide modal simulations, we have found that the velocity match effect is much more dominant than modal overlapping change with this small index change.

We have two different types of configurable couplers for the OSP structure. We name them the "racetrack coupler" and the "splitting coupler." The racetrack coupler is located at the interface between the straight waveguide and the racetrack waveguide and is labeled as t_r in Fig. 2. The splitting couplers are located in and out of the Mach-Zehnder structure and are labeled as t_1 and t_2 in Fig. 2.

The purpose of the racetrack coupler is to tune the amount of resonance in the racetrack and hence to configure the amplitude of the pole. There are two requirements for the racetrack coupler. First is that its interaction length should be small to reduce the optical loss. Since the total optical round trip loss of the racetrack includes the optical loss of the racetrack coupler,

it is important to minimize its optical loss, and hence the interaction length. Second is that it should be designed at the critical coupling state of the racetrack. Since the racetrack is most sensitive to the tuning of the racetrack coupler in its critical coupling state [32], it would be ideal that the transmission coefficient (t_r) of the racetrack coupler is matched to the round trip loss factor (α_{RT}) of the racetrack. The round trip loss factor of the racetrack is expected to be around 0.6–0.7. Therefore, the racetrack coupler should be compact in size and designed such that its transmission coefficient (t_r) becomes around 0.6–0.7. Using optical simulation, we design its interaction length and separation near 2 mm and 4.5 μm , respectively.

The splitting coupler is for controlling the energy splitting between two branches of light at the input port and to the output port. Since the splitting couplers tune the location of the zero, they should be as configurable as possible. Using optical simulation, we design its interaction length and separation near 6 mm and 5.1 μm , respectively.

IV. ONE-BLOCK OSP ANALYSIS

As discussed earlier, the one-block OSP generates a single zero and a single pole simultaneously. The degrees of freedom to locate a zero or a pole in the Z space is two since a zero or a pole is a complex value, and thus has both amplitude and phase. Their locations in the Z space are controlled by the four different electrodes shown by the shaded bars (red if colored) in Fig. 2. With N cascades of the unit block, an OSP can generate N number of zero and pole pairs as shown Fig. 3. The poles of the whole OSP system are the same as those of the individual unit blocks. On the other hand, the zeros of the whole system are not the same as those of the unit blocks since both the output power and the conjugated power of a unit block are cascaded to the next unit block by coupling each other. Because of this problem, it is not trivial to identify the zeros of a multiply cascaded structure. Jinguji demonstrated a synthesis algorithm for analyzing these structures [5]. However, their technique cannot be applied generally to a lossy system since their technique assumed that the unit structure is lossless. Thus, a synthesis method for our structure that includes loss factor has been developed by modifying Jinguji's algorithm, which is not included here due to its mathematical complexity.

However, dealing with just an one-block OSP is relatively easy and straight forward. By using the scattering matrices, we can derive the scattering parameters, which are useful to understand the operation of the one-block OSP. First, before deriving the scattering matrices, we define the scattering matrices of the individual components. And then, we cascade their matrices to find the scattering matrices of the entire one-block OSP. Having defined the individual scattering matrices for the one-block OSP, the scattering matrix, S , for an one-block OSP shown again in Fig. 6 is the multiplication of the individual scattering matrices

$$S = S_1 S_2 S_3 = \begin{pmatrix} S_{11} & S_{21} \\ S_{12} & S_{22} \end{pmatrix} \quad (4)$$

where S_1 and S_3 are the scattering matrices for the two splitting couplers, and S_2 is the Mach-Zehnder section as shown in

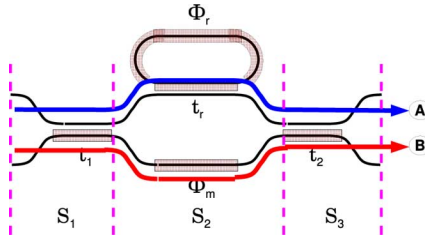


Fig. 6. Unit block of OSP with appropriate symbols for mathematical analysis. The individual scattering matrix transfer function consists of two different terms. One, labeled as “Path A,” is associated with the light beam which propagates through the racetrack and the other, labeled as “Path B,” is with the light beam which propagates through the other Mach-Zehnder arm.

Fig. 6. The calculation is straightforward, and the scattering parameters can be summarized as

$$S_{lm} = \alpha_{lm} \left(\underbrace{\frac{t_r^* - \alpha_{RT} e^{j\tau\omega} e^{j\phi_r}}{1 - t_r \alpha_{RT} e^{j\tau\omega} e^{j\phi_r}}}_{\text{Path A}} + \underbrace{R_{lm} e^{j\phi_m}}_{\text{Path B}} \right) \quad (5)$$

where

$$\begin{aligned} \alpha_{11} &= \alpha_1 \alpha_2 \alpha_r (+1) t_1 t_2 \\ \alpha_{12} &= \alpha_1 \alpha_2 \alpha_r (-j) t_1 c_2^* \\ \alpha_{21} &= \alpha_1 \alpha_2 \alpha_r (-j) c_1 t_2 \\ \alpha_{22} &= \alpha_1 \alpha_2 \alpha_r (-1) c_1 c_2^* \\ R_{11} &= (-1) \frac{c_1^*}{t_1} \frac{c_2}{t_2} \frac{\alpha_m}{\alpha_r} e^{-j\tau_c\omega} e^{j\phi_m} \\ R_{12} &= (+1) \frac{c_1^*}{t_1} \frac{t_2^*}{c_2^*} \frac{\alpha_m}{\alpha_r} e^{-j\tau_c\omega} e^{j\phi_m} \\ R_{21} &= (+1) \frac{t_1^*}{c_1} \frac{c_2}{t_2} \frac{\alpha_m}{\alpha_r} e^{-j\tau_c\omega} e^{j\phi_m} \\ R_{22} &= (-1) \frac{t_1^*}{c_1} \frac{t_2^*}{c_2^*} \frac{\alpha_m}{\alpha_r} e^{-j\tau_c\omega} e^{j\phi_m} \end{aligned} \quad (6)$$

where t and c ($|t|^2 + |c|^2 = 1$) are the transmission and coupling ratio of each coupler, and α represents the optical losses inside the corresponding coupler. $\tau (= \tau_c + \tau_r)$ is the total round trip time, and $\alpha_{RT} (= \alpha_{RT1} \alpha_r)$ is the total round trip loss. α_m and ϕ_m are the optical loss factor and the phase shift in the Mach-Zehnder phase shifter. τ_c and τ_r are the transition time in the racetrack coupler and in the racetrack, α_{RT1} and α_r are the optical loss factor in the racetrack coupler and in the racetrack, respectively. The optical loss factors represent the electric field attenuation on a linear scale and become unity in lossless waveguides.

As seen in the under brackets in (5), the individual scattering matrix transfer function consists of two different terms. One, labeled as “Path A,” is associated with the light beam which propagates through the racetrack and the other, labeled as “Path B,” is for the light beam which propagates through the other Mach-Zehnder arm. The Path A and B terms correspond to two paths indicated in Fig. 6. Therefore, the Path A term contains the transfer function of the racetrack while the Path B term is independent of the optical delay line formed by the racetrack.

The two terms are summed at the output port depending on the coupling ratio of the two splitting couplers. The amplitude of

R_{lm} stands for the normalized intensity of Path B with respect to the maximum intensity of Path A. Note that the amplitude and the phase of Path B beam of light are controlled by the two splitting couplers and the ϕ_m electrode, respectively and that the transfer function and the resonant wavelength of the racetrack (Path A light beam) are controlled by the t_r and the ϕ_r electrodes, respectively. The mathematical representation in (5) is useful for an intuitive and physical understanding of the one-block OSP structure and it is used when we verify the OSP experimentally later in Section V.

Another useful and more mathematical way to represent the scattering matrices is using the concept of poles and zeros. Further simplification of (5) results in

$$S_{lm} = A_{lm} \left(\frac{1 - \rho_{lm} e^{j\tau\omega} e^{j\phi_r}}{1 - \gamma e^{j\tau\omega} e^{j\phi_r}} \right) \quad (7)$$

where

$$\begin{aligned} A_{lm} &= \alpha_{lm} (t_r^* + R_{lm}) \\ \gamma &= \alpha_{RT} t_r \\ \rho_{lm} &= \gamma \frac{1 + t_r R_{lm}}{|t_r|^2 + t_r R_{lm}}. \end{aligned} \quad (8)$$

All transfer functions have the same pole, γ , while ρ_{lm} is the zero obtained from the S_{lm} scattering matrix element.

Note that the phase of γ defined in (7) is not configurable. The definition of the pole should include γ as well as either $e^{j\phi_r}$ or $e^{j\omega\tau}$ in (7) because the two terms contribute the pole phase. However, we define our pole as shown in (7) since it is convenient to understand two similar operation modes; *frequency control mode* or *delay control mode*. In this way, the similarity between two operation modes of the OSP, as we discussed in Section II, becomes clear. In the *frequency control mode*, $e^{j\tau\omega}$ term in (7) is varying and represents the unit delay Z^{-1} in the Z space. In this case, the actual pole becomes $\gamma e^{j\phi_r}$, thus, the pole phase is controlled by the ϕ_r electrode. From a practical point of view, the frequency response of the OSP is periodic with respect to the FSR and the response shifts in the frequency domain with respect to the ϕ_r value. On the other hand, in the *delay control mode*, the delay is controlled by $e^{j\phi_r}$ in (7), which represents the unit delay Z^{-1} in the Z space. In this case, the actual pole becomes $\gamma e^{j\omega\tau}$, thus, the pole phase is controlled by the input optical frequency (ω). With a similar analogy from a practical point of view, the amplitude and phase response of the OSP is periodic with respect to ϕ_r and the response shifts in the ϕ_r (or voltage) domain with respect to the input optical frequency. Note also that the phase of the zero also depends on both parameters in the same manner. By changing any of two parameters, the phases of both pole and zero are changing in the same amount. However, the zero has additional configurable degrees of freedom such as t_1, t_2 , and ϕ_m as seen in (7).

If the zero can be located in entire space and the pole can be located in any region within the unit circle in the Z space, the generality condition is satisfied. The amplitude of a pole depends on the total round trip loss factor (α_{RT}) and transmission coefficient of the racetrack coupler (t_r) as seen in (7). In the lossless case when α_{RT} becomes unity, the pole can be located at any point within the unit circle if t_r can be adjusted from 0

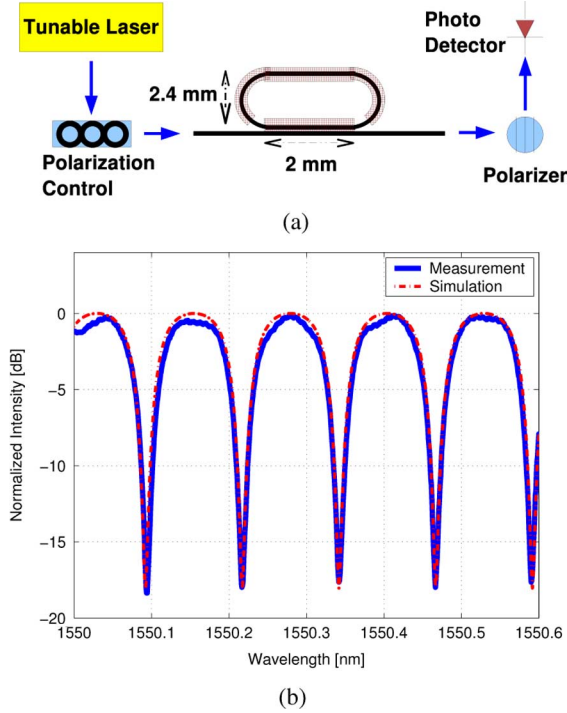


Fig. 7. Experimental setup and spectral response of a racetrack which has the same design as the OSP used. The free spectral range (FSR), extinction ratio, finesse, and Q -factor are measured 0.12 nm (15.5 GHz), 18 dB, 3.36, and 4.34×10^4 , respectively. (a) Experimental setup. (b) Measured and simulated spectral response.

to 1. However, polymer waveguides intrinsically have a certain amount of intrinsic optical loss and the configurable amount of t_r is difficult to design to have complete configurability. In this case, the actual implementable amplitude of the pole locations becomes limited. The phase of the pole depends on the optical phase change controlled by the ϕ_r phase shifter. Since the interaction length of the ϕ_m is designed 9.12 mm, 360° of the optical phase change can be obtained with applied voltage, hence any arbitrary phase of the pole is possible.

Once we determine the pole location, the zero depends on the transmission coefficients of the splitting couplers and optical phase shift in the Mach–Zehnder phase shifter as seen in (7). Since the splitting couplers are designed long enough to have as large tuning ratio as possible and the interaction length for the ϕ_m electrode is relatively long (5 mm), the phase and amplitude of the zero can cover almost entire range of the Z space. We discuss the generality of the fabricated OSP with experimental data later in Section V.

V. COMPONENTS VERIFICATION

There are several individual components or building blocks of the OSP. They are the racetracks, configurable couplers, and phase shifters. The OSP will function correctly once all these components are working correctly. Therefore, it is important to characterize and verify the individual components before integrating them. In order to verify the components, we also fabricated individual components.

First, we characterize the racetrack. Fig. 7 shows the spectral response of a racetrack and its experimental measurement setup.

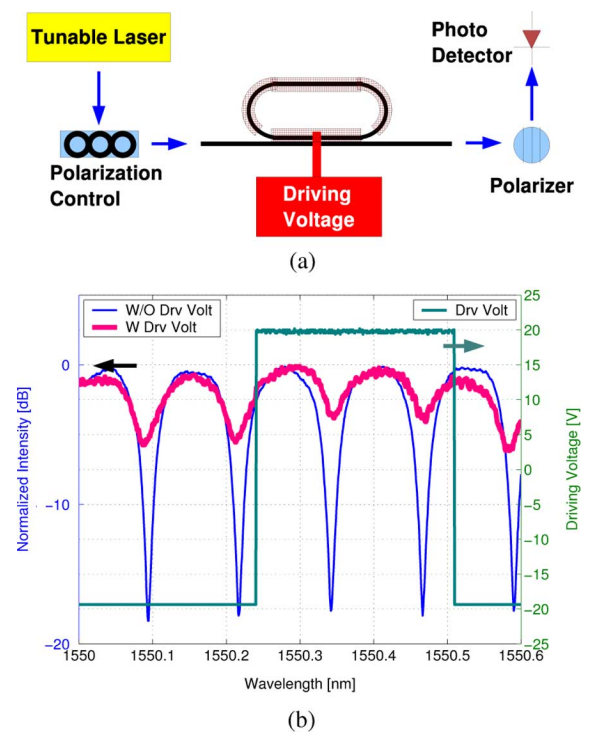


Fig. 8. Experimental setup and spectral response of a racetrack when ± 20 V is applied to the racetrack coupler. By fitting the measured response, we find that t_r becomes 0.535 ± 0.25 with an applied voltage to the racetrack coupler of ± 20 V. (a) Experimental setup. (b) Measured spectral response.

The racetrack measured has the same design as the OSP, where the bending radius of the racetrack is 1.2 mm and the interaction length of the racetrack coupler is 2 mm. An AQ4321D (Ando) is used for the tunable laser source at $1.55 \mu\text{m}$ with TM mode polarization control. As seen in Fig. 7(b), the measurement is done in a 0.6 nm wavelength span and the free spectral range (FSR), extinction ratio, finesse and Q -factor (loaded) are measured 0.12 nm (15.5 GHz), 18 dB, 3.36 and 4.34×10^4 , respectively. Using these values, the effective group refractive index, α_{RT} value, t_r value, total round trip optical loss and the optical loss inside the ring are calculated as 1.66, 0.608, 0.535, 4.4 dB and 3.85 dB/cm, respectively. Fig. 7(b) also shows the simulated spectral response using these values. Since the propagation loss of the straight waveguide is measured around 2 dB/cm, the excess loss inside the racetrack is expected to be from scattering loss due to the roughness at the interface between core and cladding materials. A similar propagation loss inside the racetrack has been obtained using 1 mm bending radius and similar electrooptic polymer material [27].

We applied voltages of ± 20 V on the t_r electrode to verify the operation of the racetrack coupler as seen in Fig. 8(a). Fig. 8(b) shows the spectral response while varying the driving voltages. The spectral response when no voltage is applied is shown as well for purpose of comparison. As seen in Fig. 8(b), the response (extinction ratio) is changed depending on the voltage. By fitting the measured response, we find that t_r becomes 0.535 ± 0.25 with an applied voltage to the racetrack coupler of ± 20 V. We also find that the local minima shift with applied voltage.

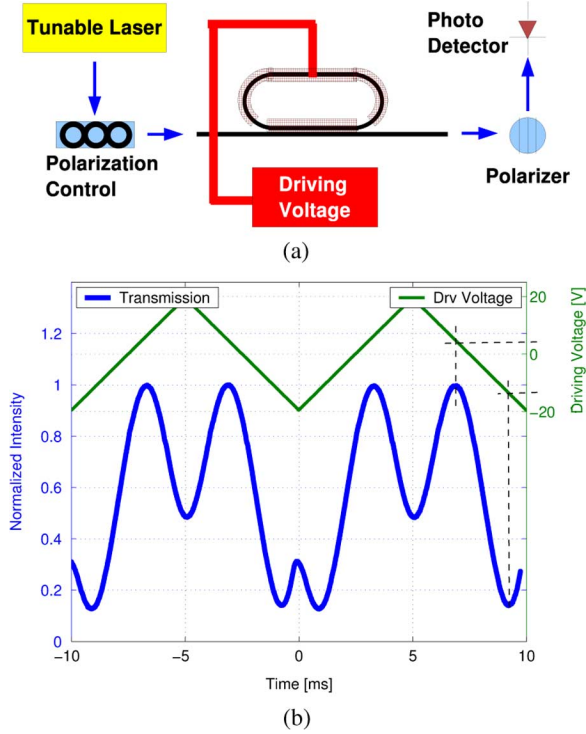


Fig. 9. Intensity response of a racetrack when ± 20 V peak-to peak triangular signal is applied to the racetrack phase shifter. The measurement shows that the half-wave voltage (V_π) of the ϕ_r phase shifter is 18.3 V. The corresponding r_{33} coefficient is also calculated as 23 pm/V. (a) Experimental setup. (b) Measured intensity.

For verification of the racetrack phase shifter, we fix the input optical wavelength at $1.55 \mu\text{m}$ and apply ± 20 V peak-to-peak triangular signal to the ϕ_r electrode. Its experimental setup and response are shown in Fig. 9(a) and (b), respectively. The measurement shows that the half-wave voltage (V_π) of the racetrack phase shifter is 18.3 V. The corresponding r_{33} coefficient is also calculated as 23 pm/V.

Two different types of couplers are considered in the OSP as we discuss in Section III. They are the racetrack couplers and the splitting couplers. For the racetrack couplers, the separation widths of $4.5 \mu\text{m}$, $4.6 \mu\text{m}$ and, $4.5 \mu\text{m}$ are considered between two waveguides and their interaction length is 2 mm. The splitting coupler has a separation of $5.1 \mu\text{m}$ and interaction length of 6 mm. Fig. 10 shows the measured S_{11} and S_{12} responses of the racetrack couplers. From the measured response, we calculate the transmission coefficients for the couplers, which are also shown in Fig. 10(d). Comparing to the simulated coupler in Section III, the measurements show that the measured transmission coefficients are smaller than the simulated values. Furthermore, the different polarity of voltages leads to different output response even though output responses should be even functions with respect to applied voltages since the waveguides are symmetric. This implies that two waveguides inside the couplers are mismatched already due to imperfect fabrication, which has also been found in conventional electrooptic Mach-Zehnder devices [33].

Fig. 11 shows measured S_{11} and S_{12} responses of the splitting couplers. Since the interaction length is designed large enough

(6 mm), both outputs reach their maximum and minimum intensities during the application of the triangular voltage waveform on the electrodes. The turn on/off voltage of the splitting coupler is 30 V and its extinction ratio is approximately 10 dB, implying that its transmission coefficient, t_1 or t_2 , can be configurable between 0.4 and 0.9 with an applied voltage of 30 V.

The Mach-Zehnder phase shifter (or ϕ_m phase shifter) is for tuning the phase of *Path B* in Fig. 6. For verification of the Mach-Zehnder phase shifter, we also apply a ± 20 V peak-to-peak triangular signal to the ϕ_m electrode. Its experimental setup and response are shown in Fig. 12(a) and (b), respectively. The measurement shows that the half-wave voltage (V_π) of the Mach-Zehnder phase shifter is 33 V. The corresponding r_{33} coefficient is calculated as 20 pm/V.

Based on the earlier discussion in this section, we summarize the parameters and their configurable range with applied voltages in Fig. 13.

- 1) The FSR of the racetrack is 0.12 nm (15.5 GHz) and the α_{RT} value is 0.608. The transmission coefficient, t_r , varies between $0.535 - 0.25$ and $0.535 + 0.25$ with ± 20 V applied voltage to the t_r electrode.
- 2) The phase, ϕ_r , can be fully configurable (0 to 2π) with ± 30 V applied voltage to the ϕ_r electrode.
- 3) The phase, ϕ_m , of the Mach-Zehnder phase shifter can be fully configurable (0 to 2π) with ± 33 V applied voltage to the ϕ_m electrode.
- 4) The splitting coupler, t_1 and t_2 , can be configurable between 0.4 and 0.9 with 30 V.

Based on measurements summarized in Fig. 13 and (7), we can find possible locations of the pole and the zero of the fabricated one-block OSP. We find the amplitude of the pole $|\gamma|$ can be between 0.17 and 0.48 and the phase of the pole can be fully configured with either ϕ_r or ω depending on the operation mode. Therefore, the pole can be located and configured inside the shaded area in Fig. 14.

On the other hand, location of the zero depends on that of the pole. According to (7), the zero has an offset from the pole; $(1 + t_r R_{lm}) / (|t_r|^2 + t_r R_{lm})$. Since this offset is a complex number as well, it is a vector in the Z space. Location of the zero is determined by this offset vector. The offset vector depends on two parameters; R_{lm} and t_r . First, assume that $|R_{lm}|$ is infinity implying all the input light goes through *Path B* and there is no power flow in *Path A*. *Path A* and *Path B* are shown in Fig. 6. In this case, the offset vector becomes 1 and the location of the zero is same as that of the pole, thus the zero cancels the pole and there will be no zero and no pole. If $|R_{lm}|$ is 0, then, the offset vector becomes real number $1/|t_r|^2$ and the zero will be α_{RT}/t_r^* , which is the same zero which the transfer function of the racetrack structure represents.

However, $|R_{lm}|$ is bounded due to the bounded transmission coefficients of the splitting couplers. As in (5), $|R_{lm}|$ is the electric field amplitude ratio between *Path A* and *Path B*, which is configured by the splitting couplers. From the bounded transmission coefficients of the splitting couplers, we find the maximum and minimum values of $|R_{lm}|$ as

$$0.2 < |R_{lm}| < 0.9 \quad (9)$$

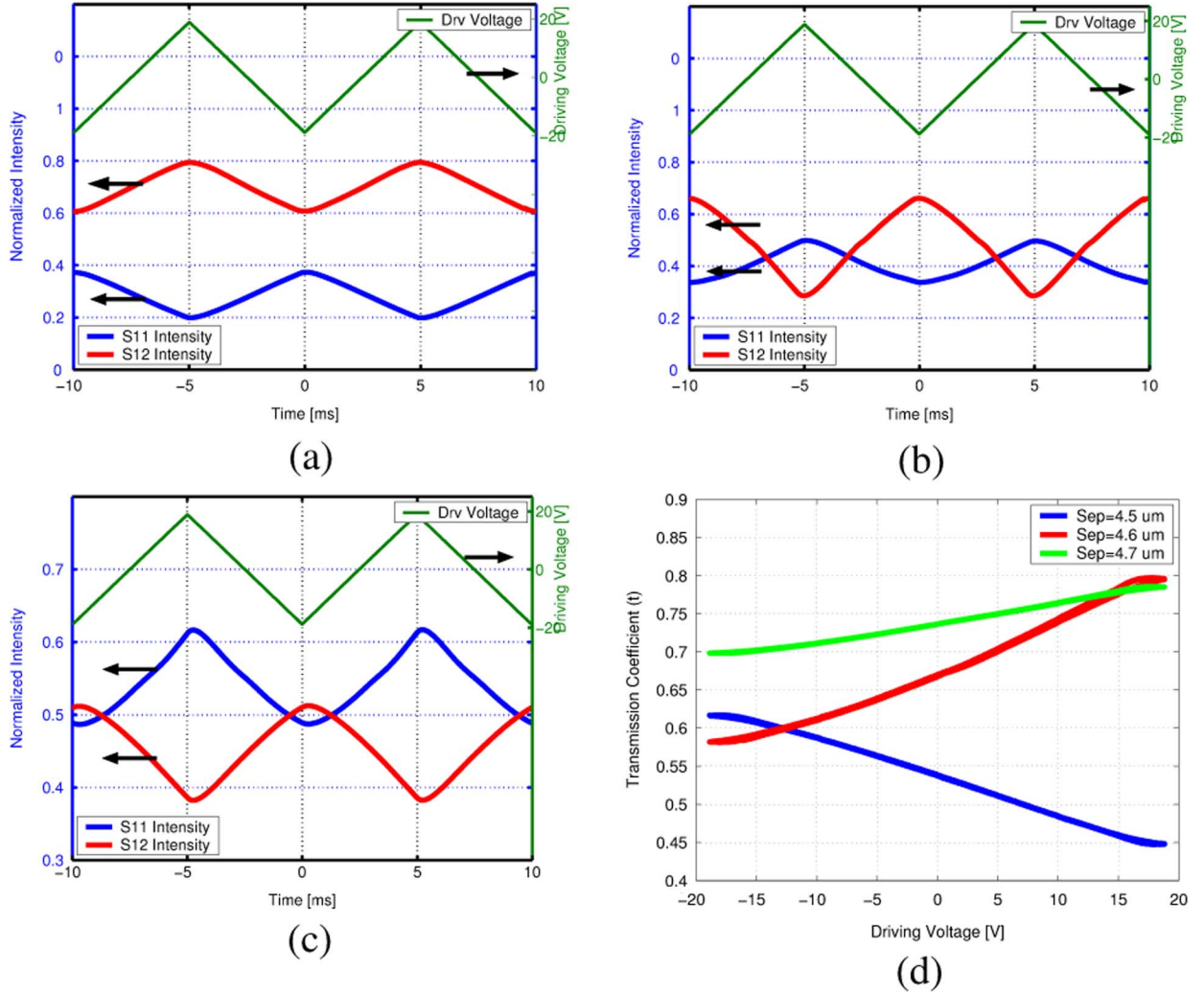


Fig. 10. Experimental measurements of S_{11} and S_{12} scattering parameters for the different racetrack couplers. (a) Sep = $4.5 \mu\text{m}$. (b) Sep = $4.6 \mu\text{m}$. (c) Sep = $4.7 \mu\text{m}$. (d) Measured t_r .

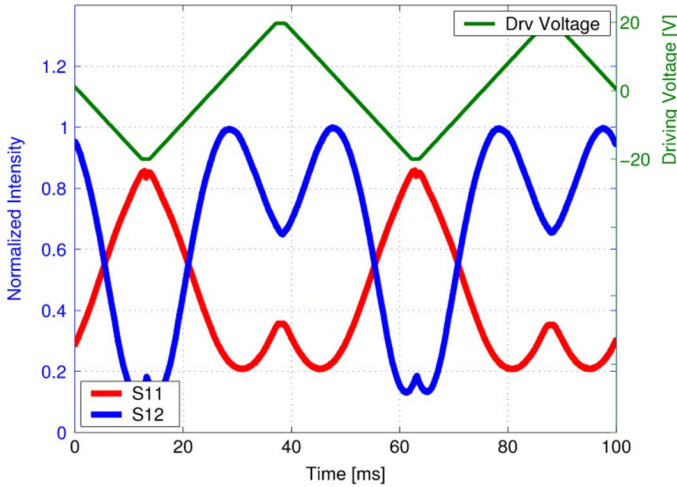


Fig. 11. Experimental measurements of S_{11} and S_{12} scattering parameters for the splitting coupler.

On the other hand, the phase of R_{lm} depends on ϕ_m . Since ϕ_m can be configured completely from 0 to 2π by $\pm 33 \text{ V}$ as shown in Fig. 13, the phase of R_{lm} is also configured completely from 0 to 2π . Therefore, the zero can be located in the entire Z space

except near two points, which are the pole and the zero of the racetrack (α_{RT}/t_r^*). The shaded area in Fig. 15(a) shows conceptually possible zero locations when the pole and the zero of the racetrack are given as shown. We use computer simulations to find the possible locations of the zeros that can be implemented by the fabricated one-block OSP. Fig. 15(b), (c) and (d) show their results in the Z space when the pole has the minimum (0.17), middle (0.325), and maximum (0.48) possible amplitude, respectively. For three plots, a dot closer to the origin and the other dot are indicating the pole and the zero of the racetrack, respectively. The zero cannot be located inside the two circles, which indicate boundaries set by the bounded $|R_{lm}|$. As the pole locates near to the unit circle, the zero can be located throughout the entire Z space.

VI. APPLICATIONS OF OSP

Due to its intrinsic arbitrariness, the OSP can be used for many applications. As for the potential high-speed analog applications, we investigate *Arbitrary waveform generators* and *Linearized modulators* using our one-block OSP.

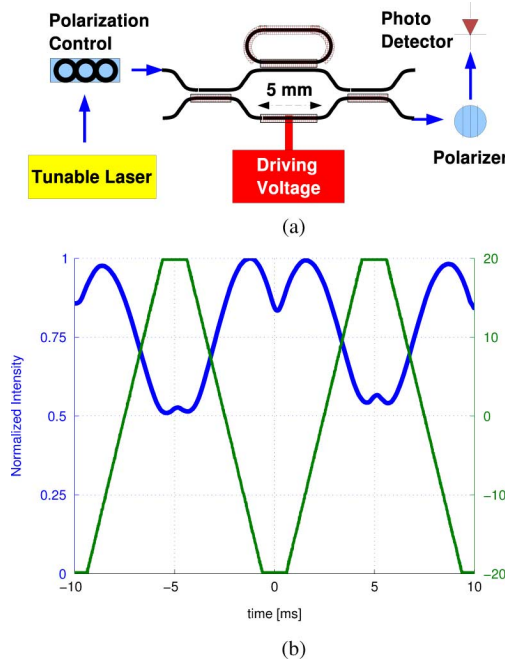


Fig. 12. Intensity response of a racetrack when a ± 20 V peak-to-peak triangular signal is applied to the ϕ_m electrode. The measurement shows that the half-wave voltage (V_π) of the Mach-Zehnder phase shifter is 33 V. The corresponding r_{33} coefficient is calculated as 20 pm/V. (a) Experimental setup. (b) Measured intensity.

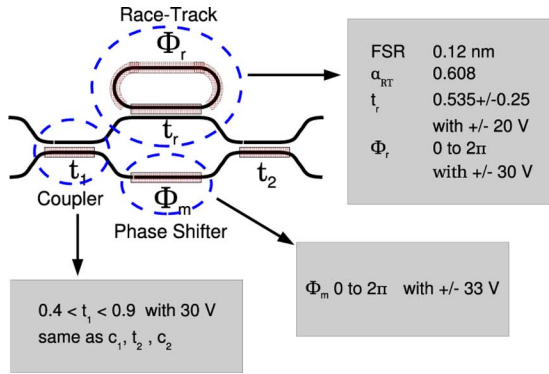


Fig. 13. Summary of one-block OSP. Based on the measurement of individual components, configurable parameters are summarized with their configurable amount and driving voltages.

A. Arbitrary Waveform Generator

It is known to be possible to implement arbitrary optical filters using PLC structures such as a notch filter, a linear dispersion filter, and a bandpass filter [2]–[5]. Such filters have been experimentally investigated in silica waveguides, where thermal tuning was used to change the index of refraction. Since the OSP employs the PLC for its structure and it is based on the fast electrooptic effect, much higher data rates (more than tens of gigahertz rate) can be accessible using the OSP. Therefore, not only is the OSP useful in fast reconfigurable optical filters, but also the OSP can be used for high-speed arbitrary waveform generators. High-speed arbitrary waveform generators are useful for modulator linearization and correction of amplifier distortion.

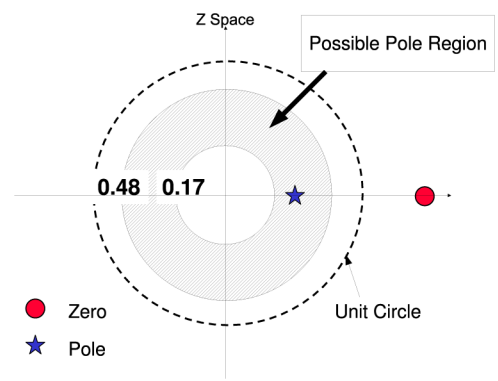


Fig. 14. Pole locations in Z space which can be implemented by one-block OSP. The amplitude of poles is bounded from 0.17 to 0.48 while the pole phase is configured from 0 to 2π as indicated in the shaded region.

Assume that we apply a sawtooth signal to an one-block OSP at the ϕ_r electrode and its peak-to-peak voltage is two times the half-wave voltage of the racetrack phase shifter. Then, during one cycle of the voltage signal, the output amplitude response of the OSP takes on the optical filter shape as a function of time. By changing other biases, the output response will also change, and hence the OSP generates arbitrary waveforms. The degree of arbitrariness of the generated signal depends on the number of unit blocks if a multiple block OSP is used and the generality of the OSP.

The detailed concept and theory of the arbitrary waveform generators have been investigated by Fetterman and Fetterman [34]. If we summarize [34], its principle of operation is based on the similarity of two operation modes of the OSP as we discussed in Section II; *frequency control mode* and *delay control mode*. According to (5), the transfer functions, S_{tm} , depend on both optical frequency and ϕ_r . If the OSP is operated with a fixed ϕ_r value and varying optical frequency (*frequency control mode*), the OSP performs optical filter as described in [2]–[5]. On the other hand, if the OSP is operated with a fixed optical frequency and varying ϕ_r value (*delay control mode*), the response of the OSP with respect to ϕ_r should be the same as an optical filter shape.

Since the OSP is based on high-speed electrooptic polymer, it can generate high-speed arbitrary waveforms. However, a sawtooth signal is difficult to obtain at high frequencies with high power [17]. Instead, we examine a simple sinusoidal signal input. Using a sinusoidal input, the OSP generates the desired output shape with proper adjustment of the parameters; t_1 , t_r , and ϕ_m .

Fig. 16 shows a measured rectangular signal generated by the one-block OSP and its experimental setup. The continuous laser source at $1.55 \mu\text{m}$ is applied to the one-block OSP with polarization control and the TM mode output of S_{22} is measured by the photodetector and the oscilloscope. First, we apply a ± 20 V peak-to-peak sinusoidal voltage input to the ϕ_r electrode. When the other biases are properly adjusted by voltage supplies as shown in Fig. 16(a), we obtain the OSPs transfer function as a function of the applied voltage as shown in Fig. 16(b). We then apply a ± 10 V peak-to-peak sinusoidal voltage input with a proper offset bias to the ϕ_r electrode while the other biases are properly adjusted. We utilize the sharp transition region in

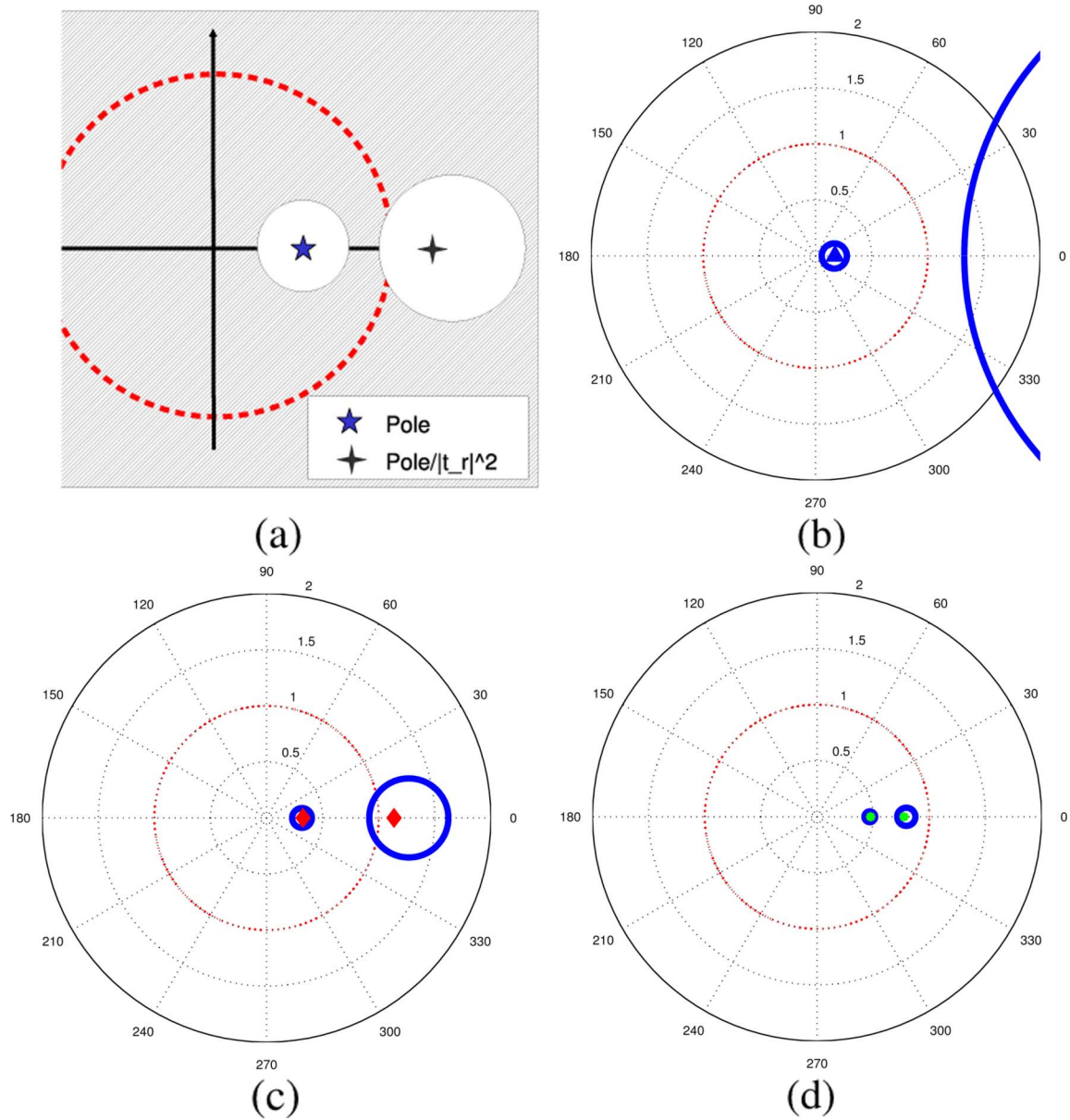


Fig. 15. The shaded area in (a) shows conceptually possible zero locations when the pole and the zero of the racetrack ($\text{Pole}/|t_r|^2$) are given. (b), (c), and (d) show simulation results of the possible zero locations in the Z space when the pole has the minimum (0.17), middle (0.325), and maximum (0.48) amplitude, respectively. For three plots, a dot closer to origin and the other dot are indicating the pole and the zero of the racetrack, respectively. The zero cannot be located inside the two circles, which indicate boundaries set by the bounded $|R_{tm}|$. (a) Poles considered (b) $\gamma = 0.17$ (c) $\gamma = 0.325$ (d) $\gamma = 0.48$.

the transfer function in Fig. 16(b) to generate the sharper rectangular output signal. As shown in Fig. 16(c), a rectangular voltage signal is obtained.

As the number of unit blocks increases, a more rectangular the shape is possible. Furthermore, this waveform can be quickly changed to another desired shape with different sets of parameters due to the fast electrooptic effect. In Section VI-B, we use the similar transfer function in Fig. 16(b) to generate another signal: a linear signal.

B. Linearized Modulator

Another useful application of the OSP is a linearized electrooptic modulator. Electrooptic modulators are one of the most important devices of lightwave communications. The most common scheme for this device is the use of a Mach-Zehnder

interferometer. However, the inherent disadvantage of this technique is a large nonlinear distortion that limits the dynamic range in analog applications [35]. Several efforts have been performed to increase the dynamic range of the optical modulator including dual-polarization techniques [36], parallel or series cascaded configurations [37], [38], and electronic predistortion schemes [39]. A dual-section directional coupler modulator using electrooptic polymer waveguides has also been developed [40].

The one-block OSP can also perform as a linearized amplitude modulator if the applied electric field modulates the optical phase inside the racetrack (*delay control mode*). When multiple coherent lights interfere, the overall intensity response is nonlinear (sinusoidal) as the optical phase changes in one of the interfered light beams. Therefore, the intensity response

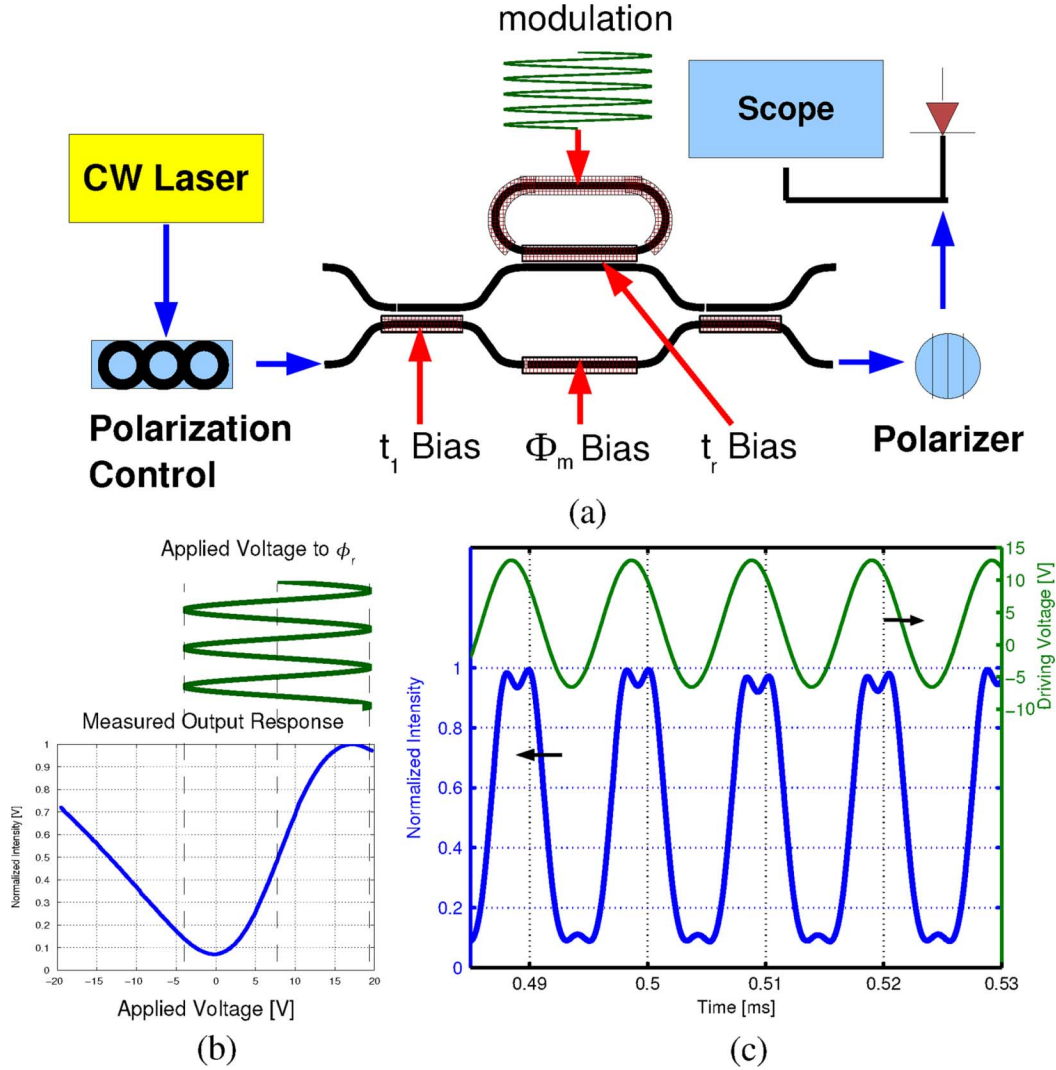


Fig. 16. Rectangular signal generation using an one-block OSP and its experimental setup. (a) A ± 10 V peak-to-peak sinusoidal voltage input with a proper offset bias is applied to the ϕ_r electrode and other biases are properly adjusted by voltage supplies. (b) We obtain a proper transfer function for the rectangular signal generation. (c) We utilize the sharp transition region in the transfer function to generate a rectangular output signal. (a) Experimental setup. (b) Transfer function measured. (c) Rectangular signal generated.

in a simple Mach-Zehnder structure is always nonlinear since the applied electric field changes the optical phase of the interfered lights in “linear” way. The fundamental concept in the linearized modulator using the one-block OSP lies in the OSP’s “nonlinear” response of the optical phase to the applied electric field. The optical phase change inside the racetrack recursively changes the overall optical phase leading to a nonlinear response, which compensates the nonlinear response of the phase modulation under proper conditions, thus, generating a “linear” intensity response overall. Note that this principle is analogous to that of the arbitrary waveform generator as discussed in Section VI-A. The linear amplitude response is a specific kind of arbitrary waveform generation.

A ring resonator assisted Mach-Zehnder (RAMZ) structure, which is similar to the one-block OSP, has been proposed to function as a linearized modulator [41] and is studied in detail including the influence of optical loss [42]. They found that the higher order nonlinear harmonic terms can vanish (up to 5th order) with proper design of the waveguide structures. As seen in (7), the transfer function with respect to the ϕ_r phase change

depends on the pole and the zero. Therefore, its linearity can be calculated by a common Taylor expansion technique using various poles and zeros. The first and higher order harmonic terms are calculated by

$$P_n = \frac{d^n |S_{lm}|^2}{d\phi_r^n} \quad (10)$$

where P_n is the n ’th high-order harmonic term and n is an integer larger than 0. Instead of using the analytical Taylor expansion technique, we utilize a numerical method to calculate the high-order nonlinear harmonic terms with various poles, zeros and biases. As a result, we find the most linear region of the response (in terms of smallest higher order terms [42]) when the pole, the zero, and the bias are $0.27\angle -1.037$ rad, $1\angle 0$ and 2.2019 rad, respectively. In this case, the third, fourth, and fifth harmonic terms vanish while the first and second harmonic terms are calculated as $0.287/\text{rad}^1$, $0.001/\text{rad}^2$, respectively. The calculation shows that the most linearized modulation occurs away from the pole location, implying that a small resonance is

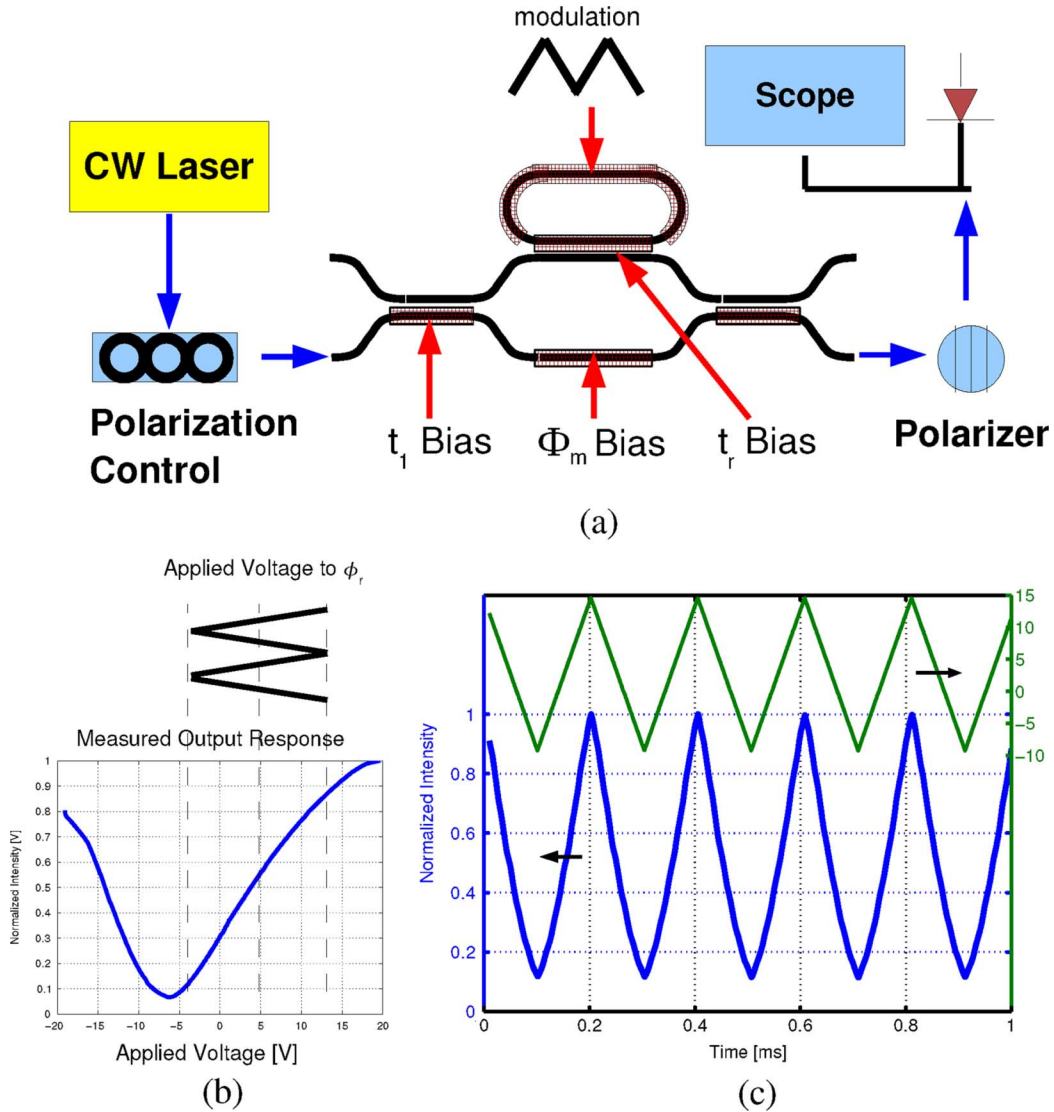


Fig. 17. Linear signal generation using an one-block OSP and its experimental setup. (a) A ± 12 V peak-to-peak triangular voltage input with a proper offset bias is applied to the ϕ_r electrode and the other biases are properly adjusted by voltage supplies. (b) We obtain a proper transfer function for linear signal generation. (c) We utilize the linear transition region in the transfer function to generate a linear output signal. (a) Experimental setup. (b) Transfer function measured. (c) Linear signal generated.

required for linearization. The relatively small correction of the nonlinear response from phase change is sufficient. Therefore, the optical loss issue is somewhat mitigated in the linearized modulator.

In order to demonstrate a linearized modulator, we use the same experimental setup as shown in Fig. 16 except that we utilize the linear slope of the transfer function and we apply a triangular signal rather than a sinusoidal signal since a triangular signal allows easier verification of linearity. As shown in Fig. 17(c), the output response linearly follows the input signal. More rigorous methods should be applied to check the linearity of a modulator such as two-tone test measurement method [43]. However, our purpose is to demonstrate the various features of the OSP.

VII. CONCLUSION

We have investigated an optical signal processor using electrooptic polymer waveguides. We have also shown that

practical applications can be made using the current state of polymer technology. Since the OSP is based on both polymers' high-speed and PLCs' complex features, it is expected to be a powerful technology for optical communications and optical computing.

However, the optical signal processor investigated in this work is limited in terms of structural complexity and operation speed; only an one-block OSP is considered for its implementation and our experiment is done at low frequencies. Similar electrooptic polymers have been used to obtain signal bandwidth more than 100 GHz [17]–[19], [44]. Therefore, the potential operation speed of the fabricated device in the work is comparable to that of those devices. In order to have a high-speed feature, we need to additionally consider high-speed design of the microtrip electrodes, such as electrode width for impedance matching and electrode thickness for reducing conductor losses at high frequency. However, due to intrinsic good velocity match characteristics of electrooptic polymers,

designing of high-speed electrodes is not a major challenge for high-speed operation. Our actual next step is to build multiple blocks of OSP. After that, we can integrate them with high-speed microstrip design for higher speed.

In order to realize more complex (or multiple) OSP structures, it is important to reduce optical propagation losses in electrooptic polymer waveguides. Since the OSP considered in this work has a racetrack structure to implement the infinite impulse response (IIR), the high optical loss not only degrades the total insertion loss but also leads to a restriction in implementing a general OSP. Current propagation losses of the straight waveguide are around 1.1–1.7 dB/cm [26]. To overcome the propagating loss limitation of the electrooptic polymer, a passive-to-active transition technique has been proposed [45]. This technique uses the hybrid silica/polymer structure with a vertical adiabatic transition between the silica and electrooptical polymer materials. Another approach is to use low loss polymer material with an adiabatic transition in the same layer [46]. This method is expected to reduce the coupling loss due to an excessive index mismatch between the two materials. If the index of the passive material is similar to the active material, standard butt coupling is also promising [47]. Furthermore, recently development of polymers with very high electrooptic r_{33} coefficients of more than 300 pm/V have been investigated. The r_{33} coefficient of 300 pm/V is more than a factor of 10 larger than the one in this work. This development poses the promising possibility of implementing much more compact and complex OSP structures.

REFERENCES

- [1] C. K. Madsen and J. H. Zhao, *Optical Filter Design and Analysis: A Signal Processing Approach*. NJ: Wiley-Interscience, 1999.
- [2] C. K. Madsen and G. Lenz, "Optical all-pass filters for phase response design with applications for dispersion compensation," *IEEE Photon. Technol. Lett.*, vol. 10, no. 7, pp. 994–996, Jul. 1998.
- [3] C. K. Madsen, "General IIR optical filter design for WDM applications using all-pass filters," *IEEE J. Lightw. Technol.*, vol. 18, no. 6, pp. 860–868, Jun. 2000.
- [4] K. Jinguiji and M. Kawachi, "Synthesis of coherent two-port lattice-form optical delay-line circuit," *IEEE J. Lightw. Technol.*, vol. 13, no. 1, pp. 73–82, Jan. 1995.
- [5] K. Jinguiji, "Synthesis of coherent two-port optical delay-line circuit with ring waveguides," *IEEE J. Lightw. Technol.*, vol. 14, no. 8, pp. 1882–1898, Aug. 1996.
- [6] N. Takato, T. Kominato, A. Sugita, K. Jinguiji, H. Toba, and M. Kawachi, "Silica-based integrated optic Mach–Zehnder multi/demultiplexer family with channel spacing of 0.01–250 nm," *IEEE J. Sel. Areas Commun.*, vol. 8, no. 6, pp. 1120–1127, Aug. 1990.
- [7] G. Lenz, B. J. Eggleton, C. K. Madsen, and R. E. Slusher, "Optical delay lines based on optical filters," *IEEE J. Quantum Electron.*, vol. 37, no. 4, pp. 525–532, Apr. 2001.
- [8] K. P. Jackson, S. A. Newton, B. Moslehi, M. Tur, C. C. Cutler, J. W. Goodman, and H. J. Shaw, "Optical fiber delay-line signal processing," *IEEE Trans. Microw. Theory Tech.*, vol. MTT-33, no. 3, pp. 193–210, Mar. 1985.
- [9] B. Moslehi and J. W. Goodman, "Novel amplified fiber-optic recirculating delay line processor," *IEEE J. Lightw. Technol.*, vol. 10, no. 8, pp. 1142–1147, Aug. 1992.
- [10] J. Capmany, J. Casbn, J. L. Martin, S. Sales, D. Pastor, and J. Marti, "Synthesis of fiber delay line filters," *IEEE J. Lightw. Technol.*, vol. 13, no. 10, pp. 2003–2012, Oct. 1995.
- [11] Y. P. Li and C. H. Henry, "Silica-based optical integrated circuits," *IEE Proc. Optoelectron.*, vol. 143, no. 5, pp. 263–280, 1996.
- [12] K. Kato and Y. Tohmori, "PLC hybrid integration technology and its application to photonic components," *IEEE J. Sel. Topics Quantum Electron.*, vol. 6, no. 1, pp. 4–13, Jan./Feb. 2000.
- [13] T. Miya, "Silica-based planar lightwave circuits: Passive and thermally active devices," *IEEE J. Sel. Topics Quantum Electron.*, vol. 6, no. 1, pp. 38–45, Jan./Feb. 2000.
- [14] R. Adar, C. H. Henry, R. F. Kazarinov, R. C. Kistler, and G. R. Weber, "Adiabatic 3-dB couplers, filters, and multiplexers made with silica waveguides on silicon," *J. Lightw. Technol.*, vol. 10, no. 1, pp. 46–50, Jan. 1992.
- [15] C. Zhang, L. R. Dalton, M. C. Oh, H. Zhang, and W. Steier, "Low V_{π} electrooptic modulators from CLD-1: Chromophore design and synthesis, material processing, and characterization," *Chem. Mater.*, vol. 13, pp. 3043–3050, 2001.
- [16] H. Zhang, M.-C. Oh, A. Szep, W. H. Steier, C. Zhang, L. R. Dalton, D. H. Chang, and H. R. Fetterman, "Push-pull electro-optic polymer modulators with low half-wave voltage and low loss at both 1310 and 1550 nm," *Appl. Phys. Lett.*, vol. 78, no. 20, pp. 3136–3138, 2001.
- [17] I. Y. Poberzhskiy, B. Bortnik, S.-K. Kim, and H. R. Fetterman, "Electro-optic polymer frequency shifter activated by input optical pulses," *Opt. Lett.*, vol. 28, no. 17, pp. 1570–1572, Sep. 2003.
- [18] D. H. Chang, H. Erlig, M. Oh, C. Zhang, W. H. Steier, L. R. Dalton, and H. R. Fetterman, "Time stretching of 102-ghz millimeter waves using novel 1.55 μ m polymer electrooptic modulator," *IEEE Photon. Technol. Lett.*, vol. 12, no. 5, pp. 537–539, May 2000.
- [19] B. Bortnik, Y.-C. Hung, H. Tazawa, B.-J. Seo, J. Luo, A. K.-Y. Jen, W. H. Steier, and H. R. Fetterman, "Electrooptic polymer ring resonator modulation up to 165 ghz," *IEEE J. Sel. Topics Quantum Electron.*, vol. 13, no. 1, pp. 104–110, Jan./Feb. 2007.
- [20] J. Han, B.-J. Seo, S.-K. Kim, H. Zhang, and H. R. Fetterman, "Single-chip integrated electro-optic polymer photonic RF phase shifter array," *J. Lightw. Technol.*, vol. 21, no. 12, pp. 3257–3261, Dec. 2003.
- [21] K. Sasayama, M. Okuno, and K. Habara, "Coherent optical transversal filter using silica-based waveguides for high-speed signal processing," *J. Lightw. Technol.*, vol. 9, no. 10, pp. 1225–1230, Oct. 1991.
- [22] A. V. Oppenheim and R. W. Schaffer, *Discrete-Time Signal Processing*. New York: Prentice-Hall, 1989.
- [23] C. J. Kaalund and G.-D. Peng, "Pole-zero diagram approach to the design of ring resonator-based filters for photonic applications," *J. Lightw. Technol.*, vol. 22, no. 6, pp. 1548–1559, Jun. 2004.
- [24] C. C. Teng and H. T. Man, "A simple reflection technique for measuring the electro-optic coefficient of poled polymers," *Appl. Phys. Lett.*, vol. 56, pp. 1734–1736, 1990.
- [25] P. Rabiei, W. H. Steier, C. Zhang, and L. R. Dalton, "Polymer micro-ring filters and modulators," *J. Lightw. Technol.*, vol. 20, no. 11, pp. 1968–1975, Nov. 2002.
- [26] S.-K. Kim, H. Zhang, D. H. Chang, C. Zhang, C. Wang, W. H. Steier, and H. R. Fetterman, "Electrooptic polymer modulators with an inverted-rib waveguide structure," *IEEE Photon. Technol. Lett.*, vol. 15, no. 2, pp. 218–220, Feb. 2003.
- [27] H. Tazawa, Y.-H. Kuo, I. Dunayevskiy, J. Luo, A. K.-Y. Jen, H. R. Fetterman, and W. H. Steier, "Ring resonator-based electrooptic polymer traveling-wave modulator," *J. Lightw. Technol.*, vol. 24, no. 9, pp. 3514–3519, Sep. 2006.
- [28] T. Yamamoto and M. Koshiba, "Numerical analysis of curvature loss in optical waveguides by the finite-element method," *J. Lightw. Technol.*, vol. 11, no. 10, pp. 1594–1583, Oct. 1993.
- [29] N.-N. Feng, G.-R. Zhou, C. Xu, and W.-P. Huang, "Computation of full-vector modes for bending waveguide using cylindrical perfectly matched layers," *J. Lightw. Technol.*, vol. 20, no. 11, pp. 1976–1980, Nov. 2002.
- [30] M. Heiblum and J. Harris, "Analysis of curved optical waveguides by conformal transformation," *IEEE J. Quantum Electron.*, vol. QE-11, no. 2, pp. 75–83, Feb. 1975.
- [31] A. Nesterov and U. Troppenz, "Plane-wave boundary method for analysis of bent optical waveguides," *J. Lightw. Technol.*, vol. 21, no. 10, pp. 1–4, Oct. 2003.
- [32] J. M. Choi, "Ring fiber resonators based on fused-fiber grating add-drop filters: Application to resonator coupling," *Opt. Lett.*, vol. 27, no. 18, pp. 1598–1600, Sep. 2002.
- [33] K. Geary, S.-K. Kim, B.-J. Seo, and H. R. Fetterman, "Mach–Zehnder modulator arm length mismatch measurement technique," *J. Lightw. Technol.*, vol. 23, no. 3, pp. 1273–1277, Mar. 2005.
- [34] M. R. Fetterman and H. R. Fetterman, "Optical device design with arbitrary output intensity as a function of input voltage," *IEEE Photon. Technol. Lett.*, vol. 17, no. 1, pp. 97–99, Jan. 2005.
- [35] T. R. Halemane and S. K. Korotky, "Distortion characteristics of optical directional coupler modulators," *IEEE Trans. Microw. Theory Tech.*, vol. 38, no. 5, pp. 669–673, May 1990.

- [36] L. M. Johnson and H. V. Roussel, "Reduction of intermodulation distortion in interferometric optical modulators," *Opt. Lett.*, vol. 13, no. 10, pp. 928–930, Oct. 1998.
 - [37] D. J. M. Sabido, M. Tabara, T. K. Fong, C.-L. Lu, and L. G. Kazovsky, "Improving the dynamic range of a coherent am analog optical link using a cascaded linearized modulator," *IEEE Photon. Technol. Lett.*, vol. 7, no. 7, pp. 813–815, Jul. 1995.
 - [38] J. L. Brooks, G. S. Maurer, and R. A. Becker, "Implementation and evaluation of a dual parallel linearization system for am-scm video transmission," *J. Lightw. Technol.*, vol. 11, no. 1, pp. 34–41, Jan. 1993.
 - [39] R. B. Childs and V. A. O'Byrne, "Multichannel AM video transmission using a high-power Nd:YAG laser and linearized external modulator," *IEEE J. Sel. Areas Commun.*, vol. 8, no. 7, pp. 1369–1376, Sep. 1990.
 - [40] Y.-C. Hung and H. R. Fetterman, "Polymer-based directional coupler modulator with high linearity," *IEEE Photon. Technol. Lett.*, vol. 17, no. 12, pp. 2565–2567, Dec. 2005.
 - [41] X. Xie, J. Khurgin, J. Kang, and F.-S. Chow, "Linearized Mach-Zehnder intensity modulator," *IEEE Photon. Technol. Lett.*, vol. 15, no. 4, pp. 531–533, Apr. 2003.
 - [42] J. Yang, F. Wang, X. Jiang, H. Qu, M. Wang, and Y. Wang, "Influence of loss on linearity of microring-assisted Mach-Zehnder modulator," *Opt. Exp.*, vol. 12, no. 18, pp. 4178–4188, Sep. 2004.
 - [43] P.-L. Liu, B. J. Li, and Y. S. Trisno, "In search of a linear electrooptic amplitude modulator," *IEEE Photon. Technol. Lett.*, vol. 3, no. 2, pp. 144–146, Feb. 1991.
 - [44] D. Chen, H. R. Fetterman, A. Chen, W. H. Steier, L. R. Dalton, W. Wang, and Y. Shi, "Demonstration of 110 GHz electro-optic polymer modulators," *Appl. Phys. Lett.*, vol. 70, no. 25, pp. 3335–3337, 1997.
 - [45] D. H. Chang, T. Azfar, S.-K. Kim, H. R. Fetterman, C. Zhang, and W. H. Steier, "Vertical adiabatic transition between a silica planar waveguide and an electro-optic polymer fabricated with gray-scale lithography," *Opt. Lett.*, vol. 28, no. 11, pp. 869–871, Jun. 2003.
 - [46] K. Geary, S.-K. Kim, B.-J. Seo, Y.-C. Huang, W. Yuan, and H. R. Fetterman, "Photobleached refractive index tapers in electrooptic polymer rib waveguides," *IEEE Photon. Technol. Lett.*, vol. 18, no. 1, pp. 64–66, Jan. 2006.
 - [47] W. Yuan, S. Kim, H. R. Fetterman, W. H. Steier, D. Jin, and R. Dinu, "Hybrid integrated cascaded 2-bit electrooptic digital optical switches (doss)," *IEEE Photon. Technol. Lett.*, vol. 19, no. 7, pp. 519–521, Apr. 2007.
- Byoung-Joon Seo** received the B.A. degree in electrical engineering from Seoul National University, Seoul, Korea, in 1998 and the M.S. and Ph.D. degrees from the University of California, Los Angeles, in 2001 and 2007, respectively, both in electrical engineering.
- He was a Research Engineer with Woori Technology, Seoul, Korea, from 1998 to 2001. Since April 2007, he has been with Jet Propulsion Laboratory, Pasadena, CA, where his research has concentrated on optical telescopes.
- Seongku Kim**, photograph and biography not available at the time of publication.
- Bart Bortnik**, photograph and biography not available at the time of publication.
- Harold Fetterman**, photograph and biography not available at the time of publication.
- Dan Jin**, photograph and biography not available at the time of publication.
- Raluca Dinu**, photograph and biography not available at the time of publication.

A Broadband Linearized Coherent Analog Fiber-Optic Link Employing Dual Parallel Mach-Zehnder Modulators

Guanghao Zhu, Wei Liu, and Harold R. Fetterman, *Fellow, IEEE*

Abstract—A composite optical transmitter based on dual parallel Mach-Zehnder modulators is proposed to linearize double-sideband suppressed-carrier coherent analog fiber-optic links. The optimization condition for achieving the best spurious-free dynamic range (SFDR) is discussed, with a simple and exact expression for the maximized SFDR being derived. Unlike other existing linearization schemes, the proposed technique has the advantages of broadband operation and shot-noise-limited signal-to-noise ratio at the same time. For a lossless link employing a transmitter laser with moderate optical power of 100 mW, a broadband SFDR as high as $144 \text{ dB} \cdot \text{Hz}^{4/5}$ is theoretically predicted.

Index Terms—Analog optical link, coherent detection, intermodulation distortion, linearized modulator, suppressed carrier.

I. INTRODUCTION

IN THE design of analog fiber-optic links, an important figure of merit that often needs to be optimized is the spurious-free dynamic range (SFDR). This SFDR is defined as the ratio of the power of the maximally allowed signal, to the power of its accompanying noise, provided that there are no detectable nonlinear distortions present. To improve the SFDR, various methods [1]–[4] have been proposed. The general idea behind these linearization schemes is to introduce certain predistortions that compensate for the existing ones with the cost of increased system complexity. For example, direct detection links with improved linearity have been demonstrated by predistorting the optical signal using two Mach-Zehnder modulators (MZMs) connected in parallel [2] or in series [3], and by employing incoherent mixing using two polarization modes [1] or two different wavelengths [4].

We note that the linearization techniques studied previously have only attempted to increase the link's SFDR by reducing the strength of the nonlinear distortions and little attention has been paid to addressing the issue of signal-to-noise ratio (SNR) at the same time. In general, the SFDR is proportional to the SNR and thus by improving the SNR, the SFDR will also be improved. It is possible to reconfigure some of those previously studied linearized links in such a way that the output SNR is optimized

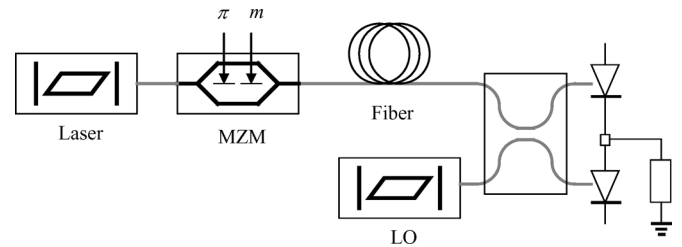


Fig. 1. Schematics of a DSSC coherent analog fiber-optic link without linearization. This link can be linearized by replacing the single MZM transmitter with a dual parallel MZM transmitter depicted in Fig. 2.

to the shot-noise level while still maintaining third-order intermodulation distortion (IMD3) free operation. However, second- and fourth-order nonlinearities are usually introduced by those SNR optimization processes and the link's broadband property is lost even if it existed before.

Here we propose and analyze a linearized coherent analog fiber-optic link, which is broadband and has an SNR inherently set at the fundamental shot-noise level. The proposed link is based on the double-sideband suppressed-carrier (DSSC) modulation format with linearization achieved by employing a dual parallel MZM transmitter. To recover the transmitted analog signal, we take advantage of balanced detection, which results in shot-noise-limited link characteristics.

II. DSSC COHERENT FIBER-OPTIC LINK

The schematics of a DSSC coherent analog fiber-optic link without linearization is shown in Fig. 1. The link's optical transmitter consists of a highly coherent laser connected to a chirpless MZM [5] which is biased at the transmission null, and modulated by an analog signal. Owing to the modulator's null bias, the optical carrier is completely suppressed. When the analog modulation is turned ON, a DSSC signal is generated and subsequently transmitted through the fiber-optic link. At the receiver end, since the optical carrier is absent, to recover the signal in the RF domain a phase-locked local oscillator (LO) with the same optical frequency as that of the transmitter laser is used to beat with the DSSC signal. The beating is accomplished by using a 3-dB coupler followed by a balanced detector. To achieve the maximum beating current, we assume that the phase difference between the LO and the signal has been locked at $\pi/2$.

For purposes of the analysis, we denote the amplitude of the transmitter laser and the LO as A_{in} and A_{LO} , respectively. Neglecting optical losses, the amplitude of the received DSSC signal can be written as $A_{in} \sin(m/2)$, where m is the push-pull

Manuscript received April 20, 2009; revised July 01, 2009. First published September 09, 2009; current version published October 14, 2009. This work was supported by the U.S. Air Force Office of Scientific Research.

The authors are with the Electrical Engineering Department, University of California, Los Angeles, CA 90095 USA (e-mail: gzhu@ee.ucla.edu; liuwei5088@gmail.com; fetter@ee.ucla.edu).

Digital Object Identifier 10.1109/LPT.2009.2031166

differential modulation phase of the applied analog signal. After balanced detection, the generated photocurrent is given by

$$I = 2\eta A_{\text{in}} A_{\text{LO}} \sin \frac{m}{2} \approx i_1 m + i_3 m^3 \quad (1)$$

where η denotes the photodetection efficiency, $i_1 = \eta A_{\text{in}} A_{\text{LO}}$ and $i_3 = -\eta A_{\text{in}} A_{\text{LO}}/24$. In the derivations, the Taylor expansion of $\sin x$ has been used. From (1), it is seen that all the even order nonlinear distortions are canceled. This allows the link to be broadband linearized by only removing the third-order term.

Noise considered here includes detector thermal noise, photocurrent shot-noise, and laser relative intensity noise (RIN). By employing the balanced detection scheme, the contribution from RIN can be removed and the noise power density of the generated photocurrent can be written as

$$N = 2qI_{\text{LO}}R + 4k_B T \quad (2)$$

where q is the electron charge, $I_{\text{LO}} = \eta A_{\text{LO}}^2$ is the current that corresponds to the total power of the LO, R is the load of the photodetector, and $4k_B T$ is the thermal noise. It follows from (2) that the DSSC coherent link becomes shot-noise-limited when the LO current is made larger than a few milliamperes (mAs).

Neglecting the thermal noise and plugging (1) and (2) into the generalized formula [6] $\text{SFDR}^{3/2} = 2/3 \cdot |i_1/i_3| \cdot i_1^2 R/N$ derived for an IMD3 limited link, we are led to

$$\text{SFDR}^{3/2} = \frac{8I_{\text{in}}}{q} \quad (3)$$

where $I_{\text{in}} = \eta A_{\text{in}}^2$ is the photocurrent that corresponds to the total power of the transmitter laser. Equation (3) predicts that the SFDR of a DSSC coherent link scales proportionally to the optical power of the transmitter laser, with no limitations imposed by the laser RIN. The avoidance of RIN is of great importance for designing links with high SFDR specifications. Previously, this can be done either by lowering the bias of the MZM [7] or by employing balanced detection to the quadrature biased MZM with dual outputs [8]. However, we note that the former approach suffers from the nearly maximized second-order RF distortion and the latter one requires special detectors that are viable with high optical power of the unsuppressed carrier. These problems are now overcome in the DSSC coherent link.

III. LINK LINEARIZATION USING DUAL PARALLEL MZMS

To linearize the DSSC coherent link, we propose to replace the single MZM transmitter shown in Fig. 1 by a dual parallel MZM transmitter shown in Fig. 2. In the proposed linearized transmitter, the laser field with amplitude A_{in} is first split into two parts with a power split ratio $\cos^2 \alpha : \sin^2 \alpha$ and then enters the two chirpleless MZMs in parallel. In order to suppress the optical carrier and other even order modulation terms, the bias of the two MZMs are both set at null. After being amplitude modulated with different push-pull phases m and $\gamma^{-1}m$ in the top and bottom MZMs, respectively, the two laser fields then recombine destructively at the output coupler with a power split ratio $\cos^2 \beta : \sin^2 \beta$. Physically, the destructive interference can be achieved by embedding a π biased phase shifter in one of the light paths. Due to the imposed π phase shift, the third-order

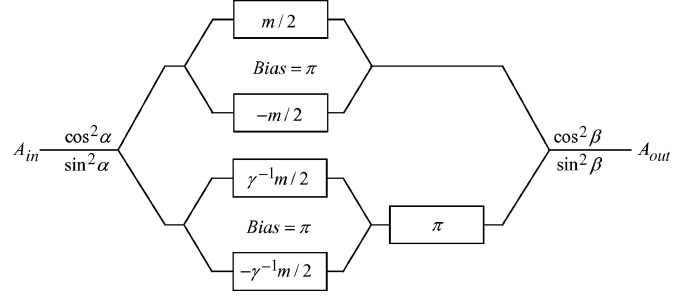


Fig. 2. Layout of a linearized optical transmitter based on the dual parallel MZMs. $\cos^2 \alpha : \sin^2 \alpha$ and $\cos^2 \beta : \sin^2 \beta$ denote the power split ratio.

components of the laser fields generated from the two MZMs will have opposite sign and under appropriate conditions (amplitude being matched) will cancel each other completely. We note that to avoid the cancellation of the signal at the same time, γ has to be different than one. Owing to the redundancy, we limit our discussions here to the case where $\gamma < 1$.

By referring to Fig. 2, the amplitude of the optical field at the linearized transmitter's output port can be calculated as $A_{\text{out}} = A_{\text{in}} \cos \alpha \cos \beta \sin(m/2) - A_{\text{in}} \sin \alpha \sin \beta \sin(\gamma^{-1}m/2)$. To linearize A_{out} , it follows from the Taylor expansion of $\sin x$ that we must require

$$\tan \alpha \tan \beta = \gamma^3. \quad (4)$$

When (4) is satisfied, the photocurrent generated by the balanced detector can be written as

$$I = 2\eta A_{\text{out}} A_{\text{LO}} \approx i_1 m + i_5 m^5 \quad (5)$$

where the coefficients are $i_1 = \eta A_{\text{in}} A_{\text{LO}} \cdot \cos \alpha \cos \beta \cdot (1 - \gamma^2)$ and $i_5 = \eta A_{\text{in}} A_{\text{LO}} \cdot \cos \alpha \cos \beta \cdot (1 - \gamma^{-2})/1920$, respectively.

Equation (5) shows that the link is broadband linearized and limited by the fifth-order intermodulation distortion (IMD5). To obtain its corresponding SFDR, we apply the generalized formula [6] $\text{SFDR}^{5/4} = \sqrt{2}/5 \cdot |i_1/i_5|^{1/2} \cdot i_1^2 R/N$ yielding

$$\text{SFDR}^{5/4} = \frac{8\sqrt{15}}{5} \cos^2 \alpha \cos^2 \beta \cdot \gamma(1 - \gamma^2)^2 \cdot \frac{I_{\text{in}}}{q}. \quad (6)$$

The SFDR in (6) can be maximized by first optimizing its value with respect to α and β , and then with respect to γ , under the constraint that the linearization condition (4) being always imposed. The optimization task with respect to α and β can be worked out by directly considering the mathematical identity $\cos^2 \alpha \cdot \cos^2 \beta = (1 + \tan^2 \alpha + \tan^2 \beta + \tan^2 \alpha \tan^2 \beta)^{-1}$ together with the inequality $\tan^2 \alpha + \tan^2 \beta \geq 2 \tan \alpha \tan \beta$. It follows from these two trigonometric conditions and (4) that $\cos^2 \alpha \cos^2 \beta \leq (1 + \gamma^3)^{-2}$, where the maximum is reachable when $\alpha = \beta$, i.e., when the input and output couplers are made identical. Note that although a symmetry argument, i.e., wherein the input/output couplers are mathematically exchangeable, can lead to a conclusion that there will be an extremum when the two couplers are equal. However, symmetry considerations alone cannot prove that such an extremum is the global maximum.

With the twin coupler condition being met, the SFDR reads

$$\text{SFDR}^{5/4} = \frac{\gamma(1 - \gamma^2)^2}{(1 + \gamma^3)^2} \cdot \frac{8\sqrt{15}}{5} \cdot \frac{I_{\text{in}}}{q}. \quad (7)$$

The value of γ that maximizes the SFDR can be obtained by setting the first-order derivative (with respect to γ) of (7) to be zero. The solution is $\gamma = (3 - \sqrt{5})/2 \approx 0.382$. In addition, from (4) the corresponding coupler power split ratio is 0.947 : 0.053, indicating the majority of the laser field will pass the top MZM.

By plugging the optimum value of γ back into (7), the formula for the maximized SFDR is finally derived as

$$\text{SFDR}^{5/4}|_{\max} = \frac{2\sqrt{15}}{5} \cdot \frac{I_{\text{in}}}{q}. \quad (8)$$

Similar to (3), (8) points out that the broadband linearized SFDR is immune to the laser RIN and thus can be increased indefinitely by boosting up the transmitter laser power. Practically, the proposed technique is limited mainly due to the optical damage [6] occurring in the electrooptic modulators. Another limitation may also come from the nonlinearity [6] of the photodetectors, which is not considered in this work. We note that in order to demonstrate high SFDR, our technique does not require photodetectors to be compatible with high incident power, as long as they can handle LO power at the level of a few milliwatts (mWs), since the strong carrier of the signal has been suppressed.

It is of interest to compare the SFDR performance of the linearized DSSC coherent link to other existing broadband linearized links such as the one proposed by Korotky *et al.* [2]. Their approach also employs a dual parallel MZM transmitter but is implemented using direct detection techniques. Keeping the notation unchanged and applying similar derivation procedures to Korotky *et al.*'s scheme, it is found once again that when the twin coupler condition is satisfied, the IMD5-limited SFDR is optimized with the result

$$\text{SFDR}^{5/4} = \frac{\gamma(1 - \gamma^2)^2}{(1 + \gamma^{3/2})^2(1 + \gamma^3)} \frac{\sqrt{15}}{5} \frac{I_{\text{in}}}{q} \cdot \left(1 + \frac{1 + \gamma^3}{(1 + \gamma^{3/2})^2} \frac{\text{RIN} \cdot I_{\text{in}}}{4q}\right)^{-1}. \quad (9)$$

Manipulation of (9) shows that when the input laser power is high and the condition $\text{RIN} \cdot I_{\text{in}} \gg 4q$ is fulfilled, by choosing again $\gamma = (3 - \sqrt{5})/2$, the SFDR in the direct detection scheme will be maximized as $\text{SFDR}^{5/4}|_{\max} = \sqrt{15}/5 \cdot \text{RIN}^{-1}$, a level that is fixed by the input laser RIN and can no longer be increased by increasing the laser power. This compares with the unlimited SFDR performance in (8) for a DSSC coherent link.

In Fig. 3, we plot the IMD5-limited SFDR as a function of the transmitter laser power $P_{\text{in}} (P_{\text{in}} = A_{\text{in}}^2)$, calculated with a 1-Hz bandwidth for a lossless DSSC coherent link and direct detection link, both employing dual parallel MZM transmitter with design that maximizes the SFDR. Responsivity $\eta = 1$ A/W is assumed in the calculation. The plotted curves demonstrate that the linearized DSSC coherent link outperforms the linearized direct detection link significantly at high laser power level, even if the laser RIN can be made as low as -170 dB/Hz. Remarkably,

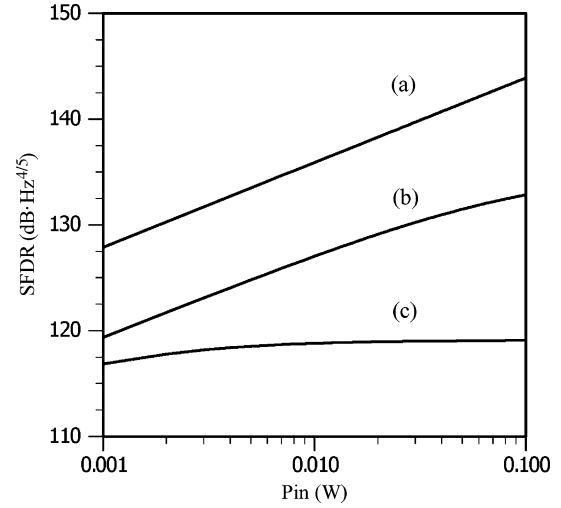


Fig. 3. Calculated IMD5-limited SFDR for a lossless (a) DSSC coherent link, direct detection link with (b) $\text{RIN} = -170$ dB/Hz, and (c) $\text{RIN} = -150$ dB/Hz.

when the transmitter laser power is set moderately at 100 mW, a broadband SFDR as much as $144 \text{ dB} \cdot \text{Hz}^{4/5}$ is potentially achievable in the linearized DSSC coherent link.

IV. CONCLUSION

We have proposed and analyzed a broadband linearized DSSC coherent analog fiber-optic link using the dual parallel MZM transmitter with balanced detection. The linearized link is inherently shot-noise limited, which enables high SFDR operation by using high laser power.

REFERENCES

- [1] L. M. Johnson and H. V. Roussel, "Reduction of intermodulation distortion in interferometric optical modulators," *Opt. Lett.*, vol. 13, no. 10, pp. 928–930, 1988.
- [2] S. K. Korotky and R. M. Ridder, "Dual parallel modulation schemes for low-distortion analog optical transmission," *IEEE J. Sel. Areas Commun.*, vol. 8, no. 7, pp. 1377–1381, Sep. 1990.
- [3] G. E. Betts, "Linearized modulator for suboctave-bandpass optical analog links," *IEEE Trans. Microw. Theory Tech.*, vol. 42, no. 12, pp. 2642–2649, Dec. 1994.
- [4] E. I. Ackerman, "Broadband linearization of a Mach-Zehnder modulator," *IEEE Trans. Microw. Theory Tech.*, vol. 47, no. 12, pp. 2271–2279, Dec. 1999.
- [5] G. Zhu, B. Bortnik, W. Liu, H. R. Fetterman, R. Forber, and W. C. Wang, "Distortion comparison of single-sideband coherent analog optical links employing X-cut and Z-cut Mach-Zehnder modulators," *IEEE Photon. Technol. Lett.*, vol. 20, no. 18, pp. 1548–1550, Sep. 15, 2008.
- [6] C. H. Cox, III, *Analog Optical Links Theory and Practice*. Cambridge, U.K.: Cambridge Univ. Press, 2004.
- [7] M. L. Farwell, W. S. C. Chang, and D. R. Huber, "Increased linear dynamic range by low biasing the Mach-Zehnder modulator," *IEEE Photon. Technol. Lett.*, vol. 5, no. 7, pp. 779–782, Jul. 1993.
- [8] L. T. Nichols, K. J. Williams, and R. D. Esman, "Optimizing the ultrawide-band photonic links," *IEEE Trans. Microw. Theory Tech.*, vol. 45, no. 8, pp. 1384–1389, Aug. 1997.

Nonlinear intermodulation distortion suppression in coherent analog fiber optic link using electro-optic polymeric dual parallel Mach-Zehnder modulator

Seong-Ku Kim,^{1,2,*} Wei Liu,¹ Qibing Pei,² Larry R. Dalton,³ and Harold R. Fetterman¹

¹Department of Electrical Engineering, University of California Los Angeles, 64-147 Engineering IV Building, Los Angeles, California 90095-1594, USA

²Department of Materials Science and Engineering, 3121-H Engineering V Bldg 420 Westwood Plaza, Los Angeles, California 90095-1594, USA

³Department of Chemistry, University of Washington, Box 351700 Seattle, Washington 98195-1700, USA
[*kimsku@ee.ucla.edu](mailto:kimsku@ee.ucla.edu)

Abstract: A linearized dual parallel Mach-Zehnder modulator (DPMZM) based on electro-optic (EO) polymer was both fabricated, and experimentally used to suppress the third-order intermodulation distortion (IMD3) in a coherent analog fiber optic link. This optical transmitter design was based on a new EO chromophore called B10, which was synthesized for applications dealing with the fiber-optic communication systems. The chromophore was mixed with amorphous polycarbonate (APC) to form the waveguide's core material. The DPMZM was configured with two MZMs, of different lengths in parallel, with unbalanced input and output couplers and a phase shifter in one arm. In this configuration each of the MZMs carried a different optical power, and imposed a different depth of optical modulation. When the two optical beams from the MZMs were combined to generate the transmitted signal it was possible to set the IMD3 produced by each modulator to be equal in amplitude but 180° out of phase from the other. Therefore, the resulting IMD3 of the DPMZM transmitter was effectively canceled out during two-tone experiments. A reduction of the IMD3 below the noise floor was observed while leaving fifth-order distortion (IMD5) as the dominant IMD product. This configuration has the capability of broadband operation and shot-noise limited operation simultaneously.

©2011 Optical Society of America

OCIS codes: (130.3120) Integrated optics devices; (230.4110) Modulators; (130.5460) Polymer waveguides.

References and links

1. B. M. Haas, and T. E. Murphy, "A simple, linearized, phase-modulated analog optical transmission system," *IEEE Photon. Technol. Lett.* **19**(10), 729–731 (2007).
2. A. Djupsjobacka, "A linearization concept for integrated-optic modulators," *IEEE Photon. Technol. Lett.* **4**(8), 869–872 (1992).
3. S. K. Korotky, and R. M. de Ridder, "Dual parallel modulation schemes for low-distortion analog optical transmission," *IEEE J. Sel. Areas Comm.* **8**(7), 1377–1381 (1990).
4. G. Zhu, W. Liu, and H. R. Fetterman, "A broadband linearized coherent analog fiber optic link employing dual parallel mach-zehnder modulators," *IEEE Photon. Technol. Lett.* **21**(21), 1627–1629 (2009).
5. H. Seong-Ku Kim, H. Zhang, D. H. Chang, C. Zhang, C. Wang, W. H. Steier, and H. R. Fetterman, "Electrooptic polymer modulators with an inverted-rib waveguide structure," *IEEE Photon. Technol. Lett.* **15**(2), 218–220 (2003).
6. W. Yuan, S. Kim, H. R. Fetterman, W. H. Steier, D. Jin, and R. Dinu, "Hybrid integrated cascaded 2-bit electrooptic digital optical switches (DOSs)," *IEEE Photon. Technol. Lett.* **19**(7), 519–521 (2007).
7. B. Li, R. Dinu, D. Jin, D. Huang, B. Chen, A. Barklund, E. Miller, M. Moolayil, G. Yu, Y. Fang, L. Zheng, H. Chen, and J. Vemagiri, "Recent advances in commercial electro-optic polymer modulator," *OFC/OC 2007*, 115–117 (2007).

8. S. Kim, W. Lui, Q. Pei, L. R. Dalton, and H. R. Fetterman, "Suppression of intermodulation distortion in coherent system using polymeric dual parallel Mach Zehnder Modulators," in Conference on CLEO/QELS 2010, Technical paper ATuB2 (2010).
-

1. Introduction

Most techniques to modulate an optical carrier in analog fiber optic links composed of external Mach-Zehnder (MZ) modulators. The MZ modulators have intrinsically a nonlinear transfer function that distorts the transmitted signal, limiting the link's dynamic range [1]. For external modulators, several approaches for improving the linearity of the devices have been suggested [2]. The two most common depend upon adjustment of the transfer function to fit a triangular function, or the elimination of the cubic term in the Taylor-expansion of the transfer function. Over the years, eliminating the cubical term has been shown to be the most successful. Linearization concepts using a DPMZM scheme have been explored in Ref [2], [3]. These approaches eliminate the cubic terms by using IMD3 cancellation along with an intensity modulation direct detection method.

In a recent paper [4], the optimization condition of the double-sideband suppressed-carrier (DSSC) coherent analog fiber optic link using a DPMZM transmitter to achieve the high spurious-free dynamic range (SFDR) was theoretically discussed. For a lossless link employing a transmitter laser with optical power of 1W, a SFDR as high as 152dB·Hz was derived by assuming the photo-conversion efficiency of 1A/W. In this letter, we demonstrate a linearized DPMZM transmitter that suppresses the nonlinear term in third order based on an amplitude modulation coherent detection scheme. In our experiment, a DPMZM transmitter was fabricated, using a new EO polymer material as a core layer that is both thermally and chemically stable. A two-tone test was performed on this complex structure which included three MZMs, five Y couplers, and a phase shifter. It was able to cancel the dominant IMD distortion in third order based on our dual parallel modulation scheme, resulting in a IMD reduction along with a modest signal decrease. We also discuss the advantages of the proposed linearization scheme, in a polymer photonic integrated device, which was confirmed by our experimental demonstration.

2. Polymeric materials, device fabrication and individual component test

The EO polymer structure, cross-section, and EO material properties of the device are illustrated in Fig. 1. The device's design parameters and procedures follow the previous publications [5,6]. The core material is a guest-host system which is a mixture of B10LC103 (or B10, Lumera co.) and amorphous polycarbonate [7]. The loading density for B10 is 30wt% and it has a refractive index of 1.6727 for TE and 1.6671 for TM polarizations. The B10 structure in APC has high thermal stability and exhibited 90% of the r_{33} retention after a thermal treatment of 85°C for 120h. The long term photo-stability of the B10 device when illuminating at 100mW continuous optical input has been achieved by not only engineered and more stable molecular structure but also packaging the modulators with a non-oxygen exposed environment [7]. The B10-APC layer is inserted between a lower (UV15LV) and upper cladding (UFC170A) as shown in Fig. 2. To achieve a high poling efficiency in an EO polymer, the stacked layer was poled under a high electric field. The device poling for the B10-APC thin film was performed using contact poling with a push-pull poling geometry where a diluted APC solution covered the entire surface of the device (a 4-inch wafer) to prevent the dielectric breakdown. A poling electric field of 80V/ μm at a temperature of 148°C was applied to the device for 15 min. After the poling process, the thin layer of APC was quickly removed using Acetone, and then a thin gold layer of the poling electrode was removed using a wet etching technique. The driving electrode was formed using Cr/Au deposition, and gold-electroplating. After etching of the photoresist and the seed layer of Cr and Au layers, the wafer was diced into individual devices to test. To reduce the RF signal losses the electrode thickness of the devices were increased by a pulsed gold electro-plating technique, and evaluated to be 2.0~2.5 μm thick.

As shown in Fig. 3, all the devices including MZMs, the directional coupler modulator, and phase shifter were tested separately to evaluate their operational characteristics after cutting out each component. The total device length was about 54 mm, and the total fiber-to-fiber insertion loss was estimated to be ~25dB. The MZs are intentionally different in length and the directional coupler modulator consists of a low frequency MZM with a coplanar output to give a variable splitting ratio. The output coupler was fixed in the experiment at 50:50 to simplify the fabrication. Ideally it would be for optimized at β as indicated below. In previous devices the B10 polymer optical materials were stable for over 100 days with 100mW of continuous laser illumination, and had been incorporated in modulators having high bandwidth and a low operating voltage, push-pull configuration [7]. Finally, a complete B10-APC based DPMZM transmitter was examined as shown in the next section.

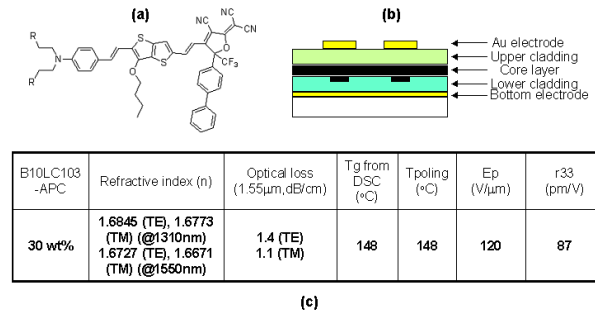


Fig. 1. EO material and device structure. (a) chemical structure of guest material, B10LC103 (or B10), (b) device cross-section, and (c) material properties of B10-APC.

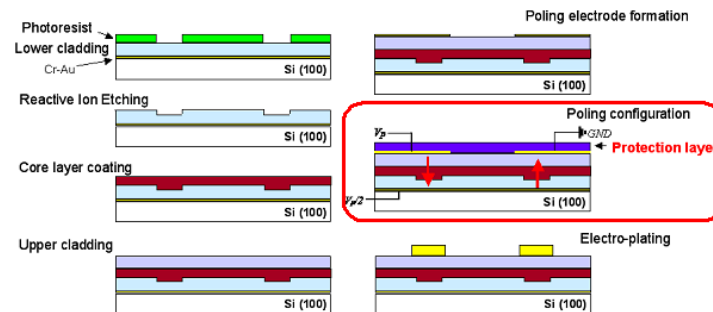


Fig. 2. Schematic diagram of the device fabrication process. A thin layer of a protection layer made of a diluted APC in TCE solution was applied to prevent from unwanted dielectric breakdown during the poling procedure. The electrode contact poling process (a circle) was done in a lab-made nitrogen purged box. The slab height of each layer such as lower cladding, core layer, and upper cladding was measured to be 2.5 μm thick, respectively. Different waveguide widths was chosen to be 3, 3.5, and 4 μm wide.

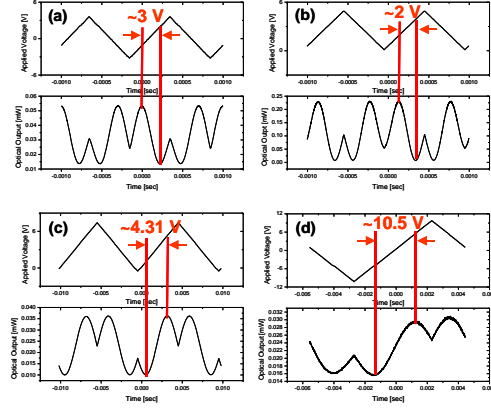


Fig. 3. Half-wave voltage measurements of all the components that used to construct a DPMZM transmitter (as shown in Fig. 4 and 5). Each component was diced from the same internal chip. (a) a Mach-Zehnder modulator 1 (MZ1), $V_{\pi} = 3\text{V}$ with an interaction length of 2cm, (b) MZ2, $V_{\pi} = 2\text{V}$ with an interaction length of 2.5cm, (c) a directional coupler modulator, $V_{\pi} = 4.31\text{V}$ with an interaction length of 1.5cm, and (d) a phase shifter, $V_{\pi} = 10.5\text{V}$ with an interaction length of 0.5cm. The device measurements were performed at a low-frequency of 1KHz.

3. Linearized DPMZM transmitter, and characterization

Previously, a composite optical transmitter based on DPMZM structure was proposed and theoretically analyzed for double-sideband suppressed coherent analog optic fiber links [4]. In this study we fabricated and tested a DPMZM transmitter as depicted in Fig. 4 and Fig. 5. Two MZMs are fed from a single optical source with a variable MZM optical coupler, and the outputs are combined to form a single transmitted signal. The two MZMs are biased at a null point such that the carrier and all even order modulation terms are suppressed [8]. The two control voltages on the directional coupler and the phase shifter are then chosen based upon the different modulation depths m and $\gamma^{-1}m$ of the two MZMs. The voltage on the directional coupler permits the output of the two IMD3 terms to be made equal in magnitude. The phase shifter permits them to be made 180° out of phase with each other. The IMD3 terms are now suppressed using the optical fields that recombine destructively at the output port. Overall, this condition can be found experimentally to induce the third order portion of the signal to be almost cancelled completely [1–4].

The calculated amplitude of the optical field at the DPMZM transmitter's end [4] is

$$A_{out} = A_m \cos \alpha \cos \beta \sin \frac{m}{2} - A_m \sin \alpha \sin \beta \sin \frac{\gamma^{-1}m}{2} \quad (1)$$

where m is the modulation depth of the applied analog signal, and the coefficient of α and β are related to the splitting ratios in the input and the output port. Expanding Eq. (1) to linearize the amplitude A_{out} , one can find that the third order terms can be cancelled when

$$\tan \alpha \tan \beta = \gamma^3 \quad (2)$$

Therefore, the current generated by the balanced detector can be written as $I = 2\eta A_{out} A_{LO} \approx i_1 m + i_5 m^5$, which means that the fifth order distortion will be dominant factor after the cancellation of IMD3 component. When α is equal to β meaning that the input and output coupler are made identical, the maximum linearity can be reached as described in Ref. [4]. In this demonstration, a Y-junction output combiner is used for simplicity. Therefore, the obtainable maximum linearity is somewhat limited because β is set to a non-ideal condition.

Figure 4(b) shows the experimental measurement setup for the nonlinearity test. The two-tone RF signals of 5GHz and 5.00002GHz are first combined and divided equally, and then applied to the modulator electrodes via GSG probes (Cascade Microtech, Inc.). The DC bias voltages for the two MZMs were controlled separately. The modulated optical signals from each of the MZMs were sent to a combiner, and then a 3-dB fiber coupler for coherent detection. A local oscillator was also used to down-convert the generated signal via the 3-dB coupler. The local oscillator was generated from the input laser using a 12.25278 GHz. Optical modulator along with a FBG to isolate one part of the sidebands. After mixing in the photodetector, the RF fundamental and the nonlinear products are amplified, and then measured by the spectrum analyzer. The two IMD3 signals are added destructively when they are π out of phase. The reduction of more than 30dB brings the IMD3 signal below the noise floor.

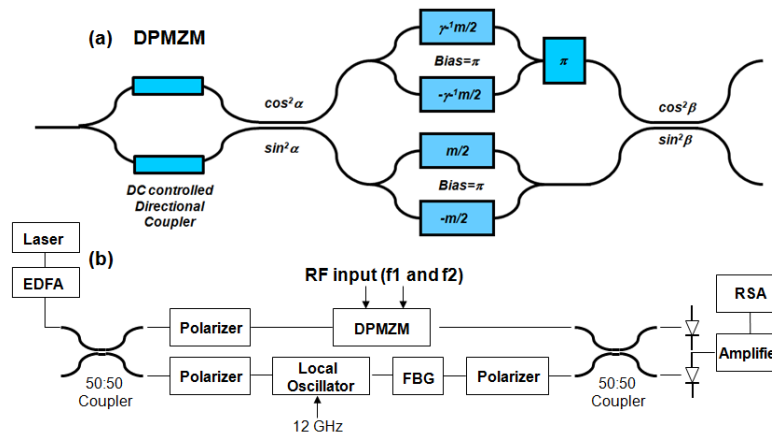


Fig. 4. Schematic layout of (a) a linearized DPMZM transmitter, and (b) a test setup. It includes a DPMZM transmitter, the laser source of 1550nm, the erbium-doped fiber amplifier (EDFA), the local oscillator (LO), and the optical filter (FBG). The LO is generated using an optical modulator, operating at 12.25278 GHz along with an optical filter (FBG) to separate the sideband. The EDFA was used to develop sufficient optical power. Polarization controllers are utilized before and after the DPMZM and the LO. The LO is used to beat the generated DSSC signal to an IF frequency (7.25278GHz). To achieve the maximum beating current, the LO has been appropriately tuned, and the beating is done using a 3 dB coupler followed by an amplifier and either a photodetector or balanced photodetector for RIN suppression.

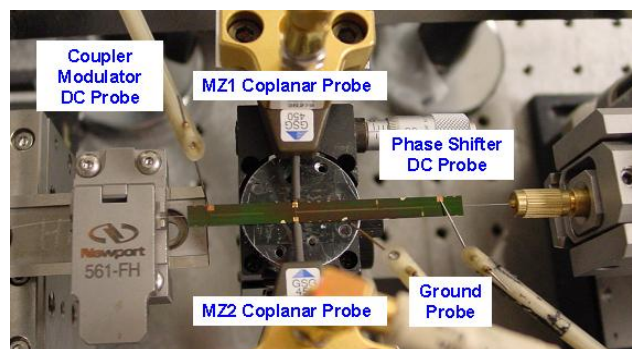


Fig. 5. Photograph of the polymeric DPMZM optical transmitter. The DPMZM is fiber-aligned in both sides, and the two MZM electrodes are contacted with GSG probes, respectively. For electrical contacts for the directional coupler, the phase shifter, and the ground contact, low-frequency pico-probes were utilized.

The experimental setup for the high-frequency measurement is shown in Fig. 5. A light source from a CW laser operating at 1550 nm was launched via optical fiber into the waveguide, coupled-out via the output optical fiber, and subsequently mixed in balanced photodetector. The optical signal and the local oscillator (LO), generated via sideband modulation, used the same laser source to ensure phase coherency during the photodetection. A linear polarizer for the coupler and two DC bias controllers at the two MZMs were carefully used to control the polarization states of the DPMZMs and the LO while observing the detected output RF spectrum. Then the nonlinear distortion cancellation was realized as shown in Fig. 6. Figure 6(a) mixing (at 12GHz-5GHz~7GHz) illustrates the measured RF electrical spectrum of the output signal when the internal phase shifter was used to make the fundamental maximum. Figure 6(b) plots the two-tone IMD result when the output linear polarizer and the bias controller of the phase shifter were adjusted for optimum IMD3 cancellation. On the other hand, while obtaining the maximum linearity, the fundamental output power was decreased by approximately 10dB. However, it is clear that the third-order IMD was significantly suppressed, (>30dB of IMD3 suppression along with a fundamental reduction of ~10dB) using the amplitude modulation and coherent detection of the polymer integrated DPMZM transmitter. The decrease of the IMD3 is a consequence of the phase cancellation of the coefficient of the IMD3 term as indicated in Eq. (8) in Ref. [4] and not a change in the optical power in either MZM.

Figure 7 shows the fundamental and IMD3 power as a function of input power. Without linearization, the power of the fundamental and IMD3 signal have an increment of 1dB and 3dB for every 1dB rise in input power, indicating that the IMD3 is the limiting distortion product. When the input power reaches ~13.4dBm by controlling the biases of the directional coupler and the phase shifter, a partial reduction of IMD3 was performed as illustrated in Fig. 7. After further increasing the input power, the IMD5 power appeared as a measurable quantity. The increase of 5dB in IMD5 power for every 1dB rise reveals that the third-order IMD is being suppressed and the fifth-order IMD is now the limiting product, and the corresponding SFDR has estimated ~7dB enhancement in this experiment.

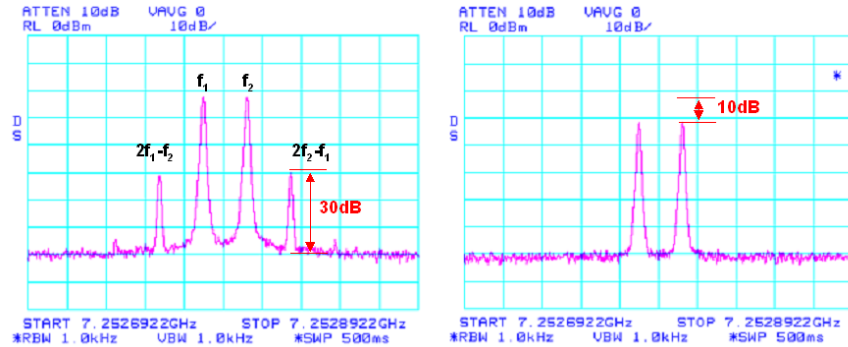


Fig. 6. Experimental results for two-tone IMD test. (a) without and (b) with linearization. The IMD3 was suppressed by >30dB to the noise level, while the fundamental power was sacrificed by ~10dB. The improved linearity was achieved at the expense of a small decrease in the fundamental amplitude signal due to a partial cancellation when the dominant distortion from the MZMs is subtracted [3].

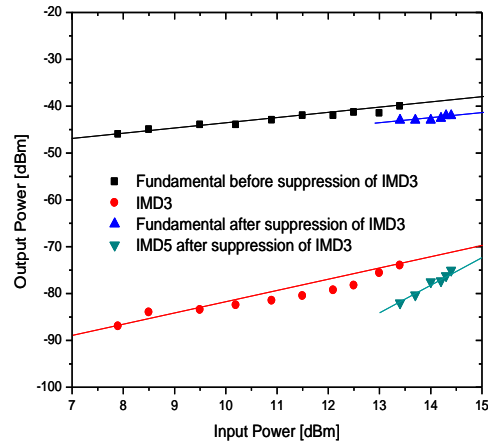


Fig. 7. Output power versus input RF power from the two-tone RF spectrum. (■) with slope = 1 represents the fundamental signal without linearization, and (●) with slope = 3 represents the third order intermodulation distortion without linearization, (▲) with slope = 1 and (▼) with slope = 5 are the fundamental and IMD5 signal after linearization process. It is note that the suppression of IMD3 has not been optimized with β to obtain maximum distortion suppression. However, the SFDR enhancement of ~7dB in above experiment was determined.

4. Conclusion

In conclusion, we have fabricated and examined an EO polymeric DPMZM transmitter for a broadband linearized DSSC coherent analog fiber optic link. The linearized scheme used involves cancellation of the IMD3 signal to produce high linearity. By adjusting the DC bias of the components in the DPMZM transmitter, the observed IMD3 product of the MZMs was almost completely eliminated along with a 10dB reduction in the fundamental. This proof-of-concept experiment illustrates the validity of making a linearized modulator for a coherent system using an EO polymeric DPMZM transmitter. Because of the use of a balanced detector in this coherent link approach, the RIN noise in the system can be effectively removed, and the SFDR will improve directly with increasing laser power.

Photoassisted Corona Poled YLD-124/DR1-co-PMMA Electrooptic Device Using Photoisomerization

Seong-Ku Kim, Qibing Pei, Harold R. Fetterman, Ben C. Olbright, and Larry R. Dalton

Abstract—A photoassisted corona poling technique (PACP) was applied to a binary chromophore system that was composed of YLD-124 and DR1-co-PMMA to enhance the poling efficiency of an electrooptic (EO) polymer device. The DR1 chromophores as a photoaddressable host material were resonantly irradiated by a polarized pumping green laser beam at a wavelength of 532 nm which is within its molecular absorption band. This process caused the DR1 chromophore's reorientation via a *cis-trans* photoisomerization process. The coupled YLD-124 system's dipoles were then poled with the assistance of a static electrical field applied to the EO core layer. In this letter, we report the experimental demonstration of the photoassisted corona poling scheme in a binary chromophore system that improved Mach-Zehnder optical modulator performance by lowering its V_π . It was shown that the device's V_π was reduced by 21%–23% compared to a regular device that was only corona poled without the green light assistance.

Index Terms—Binary chromophore system, electrooptic polymer, optical modulator, optical waveguide, photoassisted corona poling, photoisomerization.

I. INTRODUCTION

THE orientation of dipolar molecules under a static electric field is a widely utilized technique to create noncentrosymmetric polymer materials [1]. Two types of static field poling techniques usually used are contact electrode poling and corona poling methods. In particular, the corona poling consists of applying a high voltage between a needle point and a bottom electrode across a sample to be poled. The positive high voltage initiates a corona discharge that leads to ionization of the surrounding ambient gas and the deposition of the positive electric charges at the surface of the EO core film. This induces a high internal electric field across it. The corona poling method can be more effective when cooperating with a photoassisted poling in the case of binary chromophore systems consisting of

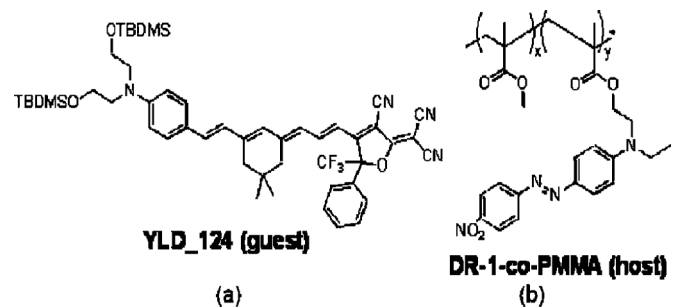


Fig. 1. Chemical structure of the binary chromophore system [3], [4]. (a) YLD-124 (guest chromophore); (b) DR1-co-PMMA (host material, side-chain attached DR1 chromophore host, $T_g = 125^\circ\text{C}$) in which PMMA is polymethylmethacrylate. Tert-butyldimethylsilyl (TBDMS) groups were attached to the π -conjugation system to enhance the chromophore's solubility and minimize dipole-dipole interactions between molecules [5]. A standard chromophore loading density of 25% by weight of YLD-124 in DR1-co-PMMA was chosen. About 16 wt% of DR1 chromophore was loaded into PMMA.

a guest chromophore doped into a coupled chromophore-containing host which is a photoisomerizable material system.

Photoassisted poling can occur at temperatures far below [1], [2] or slightly below T_g [3], [4] when the nonlinear chromophores undergo the reversible photoisomerization in the presence of a direct current (dc) field. When the polar order orientation of the *trans*-isomer occurs via the photoinduced *cis* \rightarrow *trans* thermal relaxation, an efficient polar orientation can be subsequently built after successive cycles of *trans* \leftrightarrow *cis* isomerization in the presence of a static field [1]. Essentially, the relaxation from the optically induced *trans-cis-trans* isomerization is isotropic. Using laser light polarized orthogonal to the poling electric field permits the chromophores to be pumped into orientation (Weigert effect) [4] where their optical transition matrix is zero and their dipoles are either parallel, or antiparallel to the applied electric poling field. The static field then permits the poling of the enhanced number of chromophores available with dipoles along the applied field. Coupling between the chromophores in the binary system then transfers the orientation to the guest YLD-124 molecules. The azobenzene derivatives is a very well known example of photoisomerizable molecules, resulting in such photoisomerization of $N = N$ double bond as shown in Fig. 1. The photoassisted poling parameters such as the isomers' anisotropy, pump intensity, polarization, strength of poling field, and memory of the molecular orientation during isomerization must be considered to realize the optimized device fabrication [1].

Manuscript received October 15, 2010; revised March 05, 2011; accepted March 16, 2011. Date of publication April 05, 2011; date of current version June 02, 2011. The work of S.-K. Kim, Q. Pei, and H. R. Fetterman was supported by the AFOSR under the direction of Dr. H. Schlossberg.

S.-K. Kim and H. R. Fetterman are with Department of Electrical Engineering, University of California at Los Angeles, Los Angeles, CA 90095 USA (e-mail: kimsku@ee.ucla.edu).

Q. Pei is with Department of Materials Sciences and Engineering, University of California at Los Angeles, Los Angeles, CA 90095 USA.

B. C. Olbright and L. R. Dalton are with Department of Chemistry, University of Washington, Seattle, WA 98195 USA.

Color versions of one or more of the figures in this letter are available online at <http://ieeexplore.ieee.org>.

Digital Object Identifier 10.1109/LPT.2011.2134843

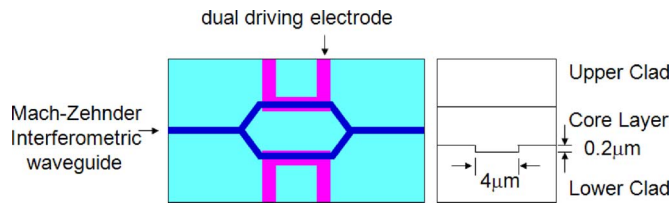


Fig. 2. Top and cross-sectional view of the optical push-pull Mach-Zehnder modulator. The waveguide width and etching depth are of 4 and 0.2 μm , respectively. The refractive index of the core layer was 1.58 at a wavelength of 1550 nm [4], and the thickness of each layer was $\sim 2.5 \mu\text{m}$, respectively. Some of the detailed optical properties of claddings were reported in [7].

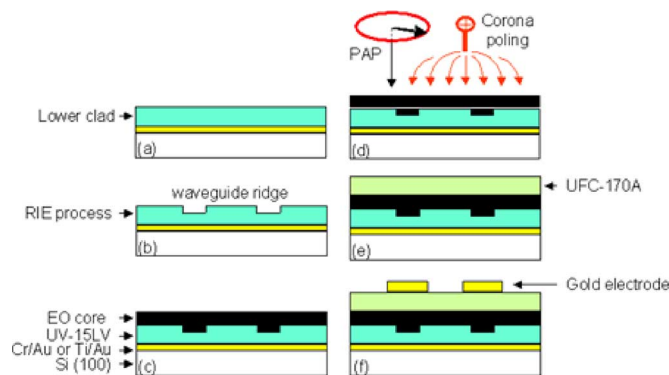


Fig. 3. Schematic diagram of the fabrication procedure for photoassisted corona poled optical device. Noncentrosymmetric polar order can be efficiently created using this PACP scheme. Chromophores whose transition dipole moment is not perpendicular to the polarization direction of irradiated light are excited across the EO polymer layer. The applied electric field perpendicular to the light polarization plane forces a polar reorientation of the molecules along the direction of the corona static electric field.

Previously, Prof. L. R. Dalton's group [3] has introduced a binary chromophore organic material, which demonstrates that both charge transport for electronic properties and charge perturbation for nonlinear optical properties can be systematically modified. A binary chromophore system such as shown in Fig. 1 can then have the ability to enhance the poling efficiency of the guest chromophore compared to regular conventional electric field poling of the same material when a polarized light is utilized to selectively excite the host chromophores [4]. This is a direct result of the coupling between the guest and host chromophores, and has been confirmed through the *in situ* reflection ellipsometry experiments and the modified attenuated total reflection (ATR) measurements [3], [4].

In this letter, the photoassisted corona poling (PACP) of a binary chromophore system consisting of a photoaddressable chromophore host (DR1-co-PMMA) and a nonphotoaddressable guest chromophore (YLD-124) is experimentally introduced, and the reduction in the driving voltage by 21–23% was demonstrated at a wavelength of 1550 nm.

The device structure and fabrication procedure are depicted in Figs. 2 and 3. The core film was prepared from solutions containing 0.12 g of dye DR1-co-PMMA, 0.25 g of YLD-124 chromophore, and 1.72 g of solvent, trichloroethane. The mixture was stirred at room temperature (RT) for about 4 hours to ensure that a homogeneous solution was present. Spin coating conditions for UV15LV (lower cladding, $n = 1.503$),

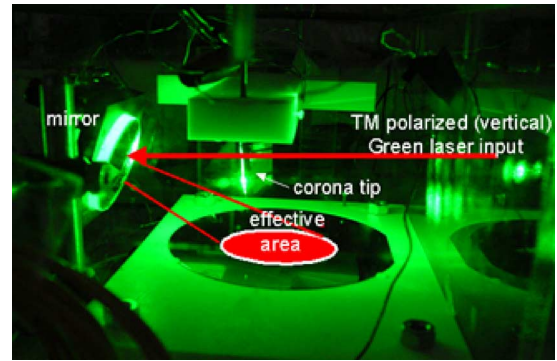


Fig. 4. Photoassisted corona poling (PACP) experimental setup. The typical corona needle-to-plane distance was about 2.5 cm and the applied dc voltage was $\sim 6 \text{ kV}$. Before the poling, the box was filled with nitrogen gas and kept for a couple of hours for stabilization of gas flow. The effective area for the green light illumination was approximately estimated to be $\sim 6.28 \text{ cm}^2$.

YLD-124/ DR1-co-PMMA, and UFC170A (upper cladding, $n = 1.488$) were respectively 3200 rpm/30 sec, 700 rpm/2 sec, and 6000 rpm/40 sec to form each layer. The waveguide patterns were defined using optical photolithography and oxygen dry-etching. After the core layer coating (Fig. 3(c)), the film was annealed at 45°C for 1 min immediately on a hot-plate.

The PACP was performed as depicted in Figs. 3(d) and 4. The EO thin films were placed in the center of a heater with and without the green light assistance. The substrate temperature was controlled by a lab-made heater and the temperature controller (Omega, model CN3201). A 25 μm diameter chromium wire was held at 2.5 cm above the film. The poling current was monitored to be 3–6 μA using a Keithley 485 current meter, and the thin film was heated at 94°C, not its glass transition temperature, to permit the EO molecules set to freely rotate throughout the coupling between their permanent dipole and the static field. During the poling, a heating process was used consisting of three steps. The sample was heated up at 6.7°C/min from room temperature to 94°C (Step1), and kept there for 10 min (Step 2), and finally reduced to RT (Step 3). For the photoassisted poling, the green light from a 530 nm laser source was used to illuminate the samples for 30 sec before ending the poling Step 2. The corona voltage was kept at 6 kV throughout the entire procedure. The PACP process was done in a nitrogen purged box. In this experiment, two sets of modulators in which each set was consisted of 16 modulators were fabricated and diced to test their electrooptical properties.

The TM polarized mode optical field was passed through optics to expand the size of the beam diameter as shown in Fig. 4. Initially, the diameter of the beam was a spot of 2 mm wide. The incident beam (Spectral-Physics, Millennia $S \times J$, diode-pumped CW visible laser, $\lambda = 532 \text{ nm}$, max. power = 15 Watt) was reflected by the mirror to illuminate the wafer surface with an elliptical effective area. The incident beam was vertically polarized and its extinction ratio was calculated to be $\sim 20 \text{ dB}$. The polarized green light was irradiated onto the film surface at an angle relative to the surface normal ($\sim 45^\circ$). The high voltage corona tip and the heater were integrated together in a nitrogen purged box. The initial beam was 1 W, the optical loss through the optic lens was estimated to about 20%,

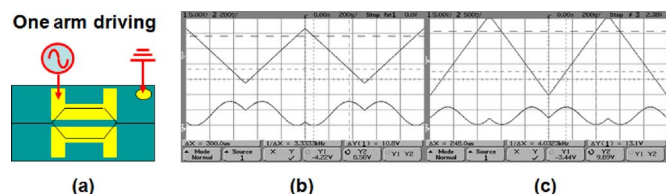


Fig. 5. Low-frequency electrooptic response of the PACPed optical polymer modulators at a TM-polarized 1550-nm wavelength. (a) Schematic diagram of the fabricated optical modulator. The device in (b) has been treated by photoassisted poling. (b) and (c) exhibited ~ 10 V, and ~ 13 V of V_{π} , respectively. (a) MZ modulator. (b) 6-KV 1-W Green Laser. (c) 6 KV only.

and the beam intensity on the illuminated surface was calculated to be ~ 100 mW/cm². This green light irradiation forces the photoaddressable chromophore (DR1) to change its geometrical shape throughout the *trans-cis* photoisomerization mechanism. This causes the DR1 molecules to be reoriented along with the axis of the applied electric field. Finally, after orientational transfer to the guest chromophores and applied static electric poling, the induced dipolar polarization is locked in place when the sample was cooled.

Due to the strong electrostatic force applied to the film, the charged particles may carry large kinetic energy when they pass through the high electric potential between the corona and the ground electrode, and then accumulated on the film surface. In some cases, it was observed that the accumulated charges on the surface of the polymer thin film leads the surface condition of the core layer to be a hydrophobic state, such that the upper cladding could not cover the poling area where it was strongly poled. In order to avoid this difficulty, the surface of the sample was slightly dry-etched to get rid of such regions. In addition, the poling temperature was also an important factor that can affect the surface morphology of the core layer. For example, with a temperature of $> 100^{\circ}\text{C}$, the surface of the thin core layer became rippled after 3–5 min poling with 6 KV along the green light illumination. The waveguides were then found to be completely damaged. Throughout this experiment, it was confirmed that the applied corona voltage, substrate temperature, and poling duration were critical and required to be optimized.

The V_{π} measurement setup was consisted of a laser source (ANDO, AQ4321D tunable laser) operating at a 1550 nm wavelength, a PDA400 (THORLAB) photodetector with a HP8153 power meter, an Agilent 54624A oscilloscope, and an HP3314A function generator as the driving source. The incident power was sent to a 4 μm -diameter small core fiber that was butt coupled to the optical waveguide throughout a polarizer (polarITE, General Photonics). The waveguide output was sent to a lens ($\times 40$) coupled to the photodetector head or to an infrared camera (FIND-R-SCOPE 1800 nm, 85400 A, Optical Systems). The output signal from the power meter was displayed on a digital oscilloscope. Fig. 5 shows the modulation curves of EO MZ modulators that were fabricated using two chromophore systems, YLD-124/DR1-co-PMMA. The total device length was 2.5 cm and the measured fiber-to-lens was ~ 14 dB for TM polarization. The low frequency measurement revealed that the driving voltage of the devices poled with the green light illumination was 10.2–10.8 V; while, the devices without the light

assistance exhibited 13.0–13.1 V in a single driving operation. This implied that $\sim 21\%$ reduction in the driving voltage can be achievable. This improvement can be explained by the selectively modification of the host order subjected to the PACP [4]. From the UV-visible absorption spectrum of unpoled YLD-124/DR1-co-PMMA matrix, adding YLD-124 into the host material made a very little change in the absorption spectra of the DR1 chromophore, meaning that the environmental homogeneity of the host chromophores is not altered. The enhancement in the poling efficiency by selective poling of the host material is therefore possible as reported by Prof. L. R. Dalton's group [4]. Mathematically, it can be shown that the r_{33} coefficient is only a function of the molecular density, first hyperpolarizability of the chromophores, the noncentrosymmetric order parameter, and local field effects [4], [6]. In this experiment, two modulators as shown in Fig. 5 have essentially the same EO material in the core and the cladding. However, only the device in Fig. 5(b) experienced the photoassisted poling procedure. Thus, the improvement in the V_{π} can be only explained due to the ordering effects, $\langle \cos^3 \theta \rangle$, i.e., the average degree of order induced among dipolar chromophores [6]. Previously, using a loading density of 25 wt% YLD-124 in DR1-co-PMMA, the r_{33} coefficient exceeded over 100 pm/V evaluated from a modified attenuated total reflection (ATR) has been reported [4]. However, in a real device fabricated here it was estimated to be ~ 20 pm/V which is far below the predicted one due to the poling difficulty of the core layer.

In conclusion, by taking the advantage of the two chromophore system subjected to both optical poling and corona poling, the device poling efficiency in binary EO polymer materials can be increased due to selectively enhanced host order. In this letter, the supercooling method (flash cooled method) [4] was not employed to maintain the maximum EO effect during the poling. Therefore, further improvement should be possible when the PACP is employed with supercooling methods. Finally, our experimental results demonstrate the potential of the PACP process and show that it can be an alternative approach in polymeric EO device fabrication.

REFERENCES

- [1] Z. Sekkat and W. Knoll, *Photoreactive Organic Thin Films*. Diego, CA: Academic, 2002, pp. 332–333.
- [2] Z. Sekkat, J. Wood, and E. F. Aust, "Light-induced orientation in a high glass transition temperature polyimide with polar azo dyes in the side chain," *J. Opt. Soc. Amer. B*, vol. 13, no. 8, pp. 1713–1724, 1996.
- [3] L. R. Dalton, P. A. Sullivan, D. H. Bale, and B. C. Olbricht, "Theory-inspired nano-engineering of photonic and electronic materials: Non-centrosymmetric charge-transfer electro-optic materials," *Solid-State Electronics*, vol. 51, pp. 1263–1277, 2007.
- [4] B. C. Olbricht, P. A. Sullivan, G. A. Wen, A. Mistry, J. A. Davies, T. R. Ewy, B. E. Eichinger, B. H. Robinson, P. J. Reid, and L. R. Dalton, "Laser-assisted poling of binary chromophore materials," *J. Phys. Chem. C*, vol. 112, pp. 7983–7988, 2008.
- [5] Y. Shi, W. Lin, D. J. Olson, J. H. Bechtel, H. Zhang, W. H. Steier, C. Zhang, and L. R. Dalton, "Electro-optic polymer modulators with 0.8 V half-wave voltage," *Appl. Phys. Lett.*, vol. 77, no. 1, pp. 1–3, 2000.
- [6] K. A. Firestone, P. Reid, R. Lawson, S.-H. Jang, and L. R. Dalton, "Advances in organic electro-optic materials and processing," *Inorganica Chimica*, vol. 357, pp. 3957–3966, 2004.
- [7] H. Zhang, "Novel Devices Based on Electro-Optic Polymers," Ph.D., University of Southern California, Los Angeles, CA, 2001.

High-Speed InAs Quantum-Dot Electrooptic Phase Modulators

Wei Liu, Richard S. Kim, Baolai Liang, Diana L. Huffaker, *Fellow, IEEE*, and Harold R. Fetterman, *Fellow, IEEE*

Abstract—In this letter, we report results of direct current (dc) and radio-frequency (RF) characteristics of self-assembled InAs quantum-dot (QD) electrooptic modulators. Although dc modulation results have been reported in the literature, these are the first high-frequency designs and measurements. These QD modulator wafers were grown by molecular beam epitaxy (MBE) and phase modulator devices were fabricated with coplanar traveling-wave electrodes. For the 800- μm -long modulators, the half-wave voltage V_π was measured as 11.4 V at 1.55 μm and 7.34 V at 1.32 μm . The phase variation is 21.9°/(mm·V). The linear electrooptic coefficient r_{41} is calculated to be 35.4 pm/V for QDs. These modulators have a 3-dB bandwidth of 10 GHz. A signal-to-noise ratio of 9 dB was measured at 20 GHz.

Index Terms—Electrooptic modulator, half-wave voltage, quantum-dot (QD) modulator, semiconductor quantum dots (QDs), 3-dB bandwidth.

I. INTRODUCTION

SEMICONDUCTOR quantum dot (QD) materials have attracted intense interest for making electrooptic modulators because of their high electrooptic coefficient (>20 pm/V) due to the quantum confined stark effect (QCSE). This capability can lead to devices with low-driving voltages and high speed operations. Compared with widely-used commercial LiNiO_3 modulators, the semiconductor QD modulators have advantages such as small size, ability to integrate with other photonic devices and potential low cost. So far, several groups have reported dc characteristics for QD modulator [1]–[4], such as phase retardation measurements and electrooptic coefficient measurements. However, few reports have been made on high frequency (>5 GHz) characteristics. In terms of the wavelength, many researchers have focused on 1.3 μm wavelength using the electroabsorption effect [2]–[4]. Research at 1.55 μm has just started in recent years using the electrooptic effect [1]. Electrooptic modulators are more promising comparing with electroabsorption modulators for their high speed, and high power saturation.

In this letter, we report dc characteristics as well as radio frequency (RF) measurements of the QD phase modulators at 1.55 μm . The half wave voltage (V_π) is 11.4 V for the 800 μm

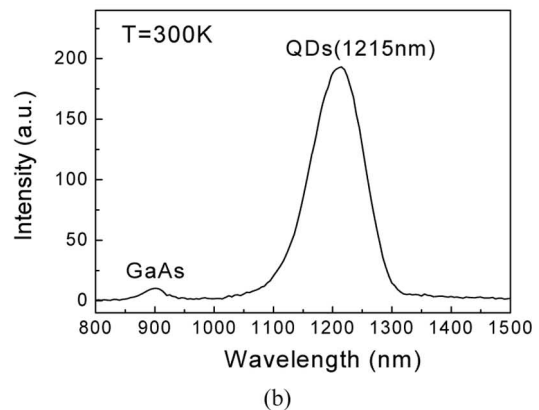
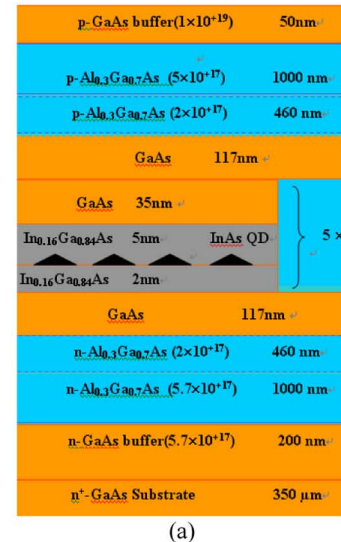


Fig. 1. (a) Schematic of the modulator wafer with five layers of QDs. (b) Photoluminescence spectrum for the QD modulator wafer.

-long modulator. With coplanar waveguide traveling-wave electrodes, these phase modulators have a 3 dB-bandwidth of 10 GHz. To the best of our knowledge, this is the first high frequency report on QD electrooptic modulators. These phase modulators show great potential in high speed photonic integrated circuits.

II. DEVICE STRUCTURES AND FABRICATION

The QD modulator wafers were grown by MBE. Fig. 1(a) shows the schematic illustration of the QD modulator structure. The QD wafers were grown on an n-GaAs (100) substrate followed by an n-GaAs buffer layer, two n- $\text{Al}_{0.3}\text{Ga}_{0.7}\text{As}$ cladding layers, a QD active region, two p- $\text{Al}_{0.3}\text{Ga}_{0.7}\text{As}$ cladding layers and a thin p-GaAs contact layer. The QD active region consists of 5 stacked InAs/InGaAs QD layers. Each layer of QDs is formed by deposition of 2.1 monolayer (ML) InAs at 480°C.

Manuscript received May 16, 2011; revised August 19, 2011; accepted August 22, 2011. Date of publication September 15, 2011; date of current version November 04, 2011. This work was supported by the Air Force Office of Scientific Research (AFOSR) under Dr. H. Schlossberg and by the Department of Defense (DoD) (through NSSEFF N00244-09-1-0091) under Dr. D. Huffaker.

W. Liu, R. S. Kim, D. L. Huffaker, and H. R. Fetterman are with the Electrical Engineering Department, University of California, Los Angeles, CA 90095 USA (e-mail: liuwei5088@gmail.com).

B. Liang is with California NanoSystems Institute, University of California, Los Angeles, CA 90095 USA.

Color versions of one or more of the figures in this letter are available online at <http://ieeexplore.ieee.org>.

Digital Object Identifier 10.1109/LPT.2011.2168201

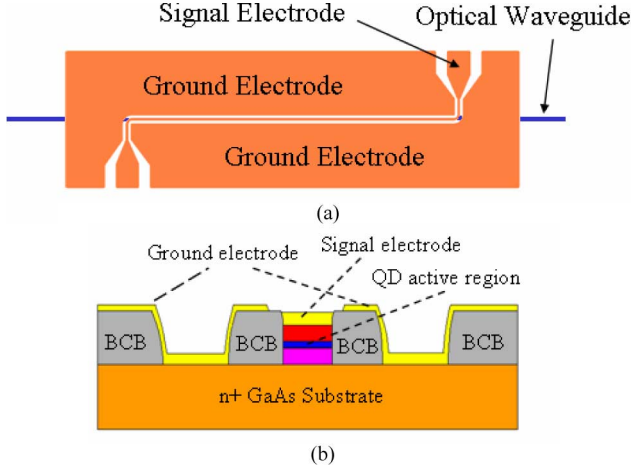


Fig. 2. (a) Top view and (b) cross-section view of the QD modulator.

Fig. 1(b) shows the photoluminescence (PL) spectrum of the QD wafer at room temperature 300 K. The QD PL peak is at 1215 nm, which is ~ 335 nm away from the test wavelength $1.55 \mu\text{m}$. The large wavelength separation was chosen for low absorption loss at $1.55 \mu\text{m}$. Because of the large wavelength separation, the first order electrooptic effect (Pockels effect) dominates, leaving the second order (Kerr effect) negligible. There is another PL peak around 900 nm, which is attributed to the GaAs emission. From Fig. 1(b), we can see that the QD PL is much stronger than that of GaAs, which indicates high quality growth of the QDs.

The QD modulators were fabricated with p-contact metal deposition, waveguide dry-etching, n-contact metal deposition, BCB polymer coating, BCB dry-etching, and gold electrode plating. Standard optical ridge waveguide structures were fabricated in these QD modulators. The ridge width varied from $3 \mu\text{m}$ to $8 \mu\text{m}$, and ridge height was $4 \mu\text{m}$. These devices had modulation regions of $800 \mu\text{m}$ long. The top view and cross-section view of the phase modulator are shown in Fig. 2. A thick BCB polymer layer was used to isolate ground and signal electrodes and reduce capacitance. The Electrode was plated to be ~ 800 nm thick to reduce microwave attenuation from the gold electrodes and facilitate high speed operation. The faces of the modulators are cleaved without any antireflective coatings.

III. EXPERIMENT SETUP AND RESULTS

The dc modulation experiment setup was conducted using a polarizer and an analyzer. Laser light was coupled into the modulator through a lens fiber, and the emitted light was gathered through a $40\times$ objective lens. The income light was linearly polarized at 45° relative to the device, which gave equal vertical and horizontal components of the E-field vector. Another polarizer was placed after the coupling objective lens as an analyzer. A signal generator was used to send a triangular modulation to the phase modulator at 100 kHz. The Optical signal was detected using a photodiode detector, and was displayed on an oscilloscope. The results are shown in Fig. 3. The half wave voltages $V_\pi = 11.4$ V were measured at $1.55 \mu\text{m}$. This corresponds to less than $1 \text{ V}\cdot\text{cm}$ modulation efficiency. This means that for a 2-mm-long Mach-Zehnder modulator using push-pull

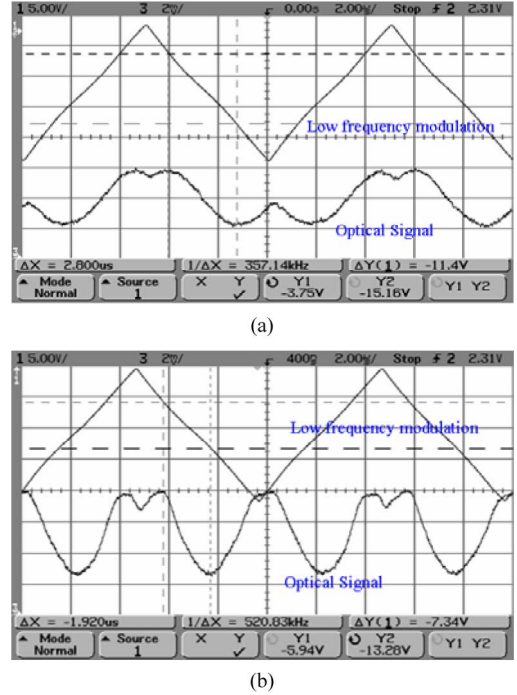


Fig. 3. (a) DC modulation characteristics at $1.55 \mu\text{m}$ and (b) dc modulation characteristics at $1.32 \mu\text{m}$.

drive, the half wave voltage V_π can be reduced to less than 2.5 V , and reverse bias voltage can be also reduce. This is an important result for low driving voltage applications. We also measured $V_\pi = 7.34 \text{ V}$ at $1.32 \mu\text{m}$. As the operation wavelength becomes closer to fluorescence peak, V_π reduces rapidly.

Using similar method described in [2], we measured phase variation per millimeter as a function of reverse bias voltage, and the result is shown in Fig. 4. A slope of 21.9° per millimeter per volt was measured. The phase variation is $\sim 70\%$ larger than the number in [1]. We obtained an excellent linear fit curve, which indicates our assumption that the linear Pockels effect is present with negligible second order Kerr effect is correct. The linear electrooptic coefficient r_{41}^{QD} was extracted by fitting the data using (1)

$$\Delta\Phi = \frac{\pi L n_0^3}{\lambda} \left(\Gamma_{\text{QD}} r_{41}^{\text{QD}} + \Gamma_{\text{GaAs}} r_{41}^{\text{GaAs}} \right) E \quad (1)$$

Where $\Delta\Phi$ is the phase retardation by electrooptic effect, n_0 is the average refractive index, E is the electric field in the undoped region, Γ_{QD} and Γ_{GaAs} are the confinement factors for QD layers and GaAs buffering layers, and r_{41}^{QD} and r_{41}^{GaAs} are the linear electrooptic coefficients for QD and GaAs. The electrooptic coefficient $r_{41}^{\text{QD}} = 35.4 \text{ pm/V}$ is significantly larger than that of GaAs bulk, which is $\sim 1.3 \text{ pm/V}$. This data also agrees with the data (34 pm/V) in [1].

The high frequency measurement setup is shown in Fig. 5(a). The $1.55 \mu\text{m}$ laser light was coupled into and out of the modulator both through lens fibers, and a HP 8350a sweep oscillator was used to generate the RF modulation. The RF modulation signal was amplified 10 dBm in power with a RF amplifier, and then combined with a reverse dc bias (-4 V) using a bias tee. A 40 GHz -bandwidth GSG probe was employed to send the modulation signal to the devices. The optical signal was detected

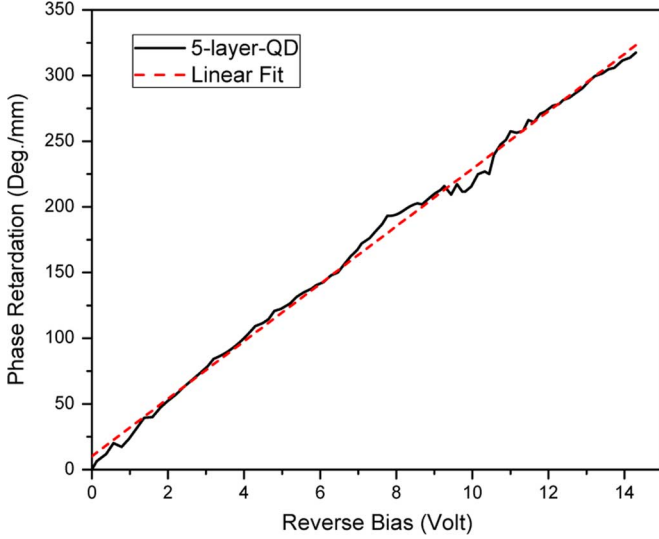


Fig. 4. Phase varies as a function of bias at $1.55 \mu\text{m}$. Solid line is experimental data. Dashed line is linear fit of experimental data.

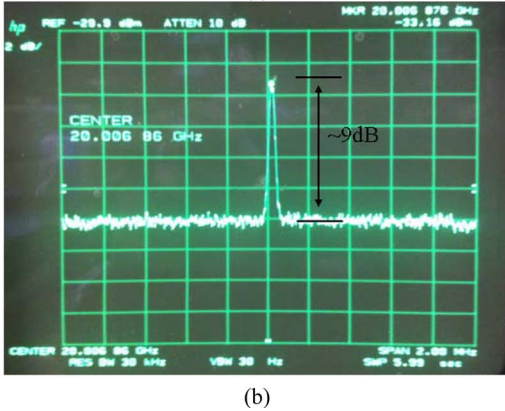
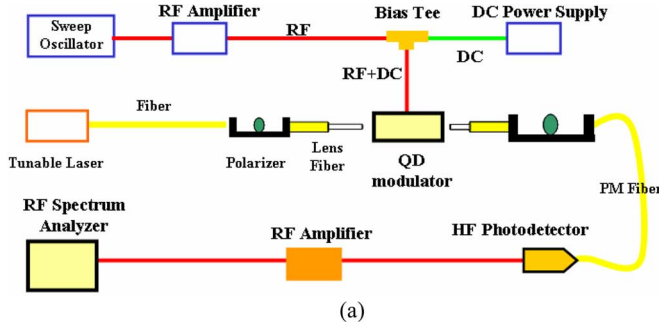


Fig. 5. (a) Experiment setup for high-frequency measurement. (b) Measured optical signal at 20 GHz.

through a high speed photodetector, and amplified through two low noise amplifiers. The result was plotted on a HP 8566B RF spectrum analyzer. Optical signals can be detected from 2 to 20 GHz using this setup. Fig. 5(b) shows the optical signal intensity measured at 20 GHz. A signal to noise ratio of ~ 9 dB was detected. This demonstrates our QD modulators can be potentially used up to 20 GHz. We also evaluated the insertion loss by measuring different lengths of devices with same coupling condition, and the insertion loss is ~ 6.5 dB/mm. The insertion loss is mainly due to the aggregate scattering loss from waveguide

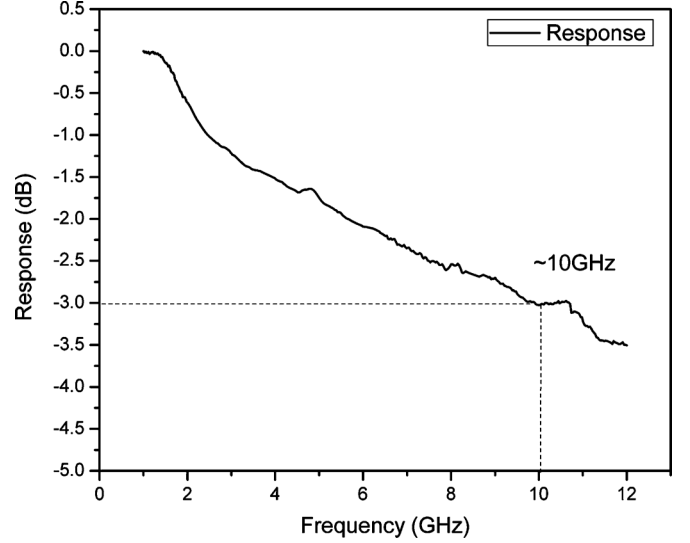


Fig. 6. Measured frequency response of the QD modulator.

sidewalls and the QDs. The loss can be significantly reduced by optimizing device fabrication process and the QD MBE growth.

The frequency response was measured with a network analyzer (HP8720ES), a high-speed photodetector, and a low-noise amplifier. A calibration run was done including all the wires and RF amplifiers. The result is shown in Fig. 6. We obtain a 3 dB-bandwidth of $f_{-3 \text{ dB}} = 10$ GHz. The roll-off is mainly due to the microwave attenuation and ohmic losses in the gold electrodes. The velocity mismatch between microwave signal and optical signal is small as a result of the short electrodes.

IV. CONCLUSION

We have grown and fabricated QD electrooptic phase modulators on GaAs substrate. V_π is 11.4 V at $1.55 \mu\text{m}$ and 7.34 V at $1.32 \mu\text{m}$ for an $800 \mu\text{m}$ -long device. By making the device longer with a push-pull drive, V_π can be significantly reduced. The phase variation is measured to be $21.9^\circ/(\text{mm}\cdot\text{V})$, and the electrooptic coefficient 35.4 pm/V . These modulators show a 3 dB-bandwidth of 10 GHz and an optical signal to noise ratio of 9 dB at 20 GHz. The insertion loss for the QD material is ~ 6.5 dB/mm.

REFERENCES

- [1] G. Moreau, A. Martinez, D.-Y. Cong, K. Merghem, A. Miard, and A. Lemaitre, "Enhanced In(Ga)As/GaAs quantum dot based electro-optic modulation at $1.55 \mu\text{m}$," *Appl. Phys. Lett.*, vol. 91, pp. 091118-1–091118-3, 2007.
- [2] J. Tatebayash, N. Nuntawong, P. S. Wang, Y.-C. Xin, L. F. Lester, and D. L. Huffaker, "Strain compensation technique in self-assembled InAs/GaAs quantum dots for applications to photonic devices," *J. Phys. D, Appl. Phys.*, vol. 42, pp. 073002–073014, 2009.
- [3] D. B. Malins, A. Gomez-Iglesias, E. U. Rafailov, W. Sibbett, and A. Miller, "Electroabsorption and electrorefraction in an InAs quantum-dot waveguide modulator," *IEEE Photon. Technol. Lett.*, vol. 19, no. 15, pp. 1118–1120, Aug. 1, 2007.
- [4] C. Y. Ngo, S. F. Yoon, W. K. Loke, Q. Cao, D. R. Lim, V. Wang, and Y. K. Sim, "Characteristics of $1.3 \mu\text{m}$ InAs/InGaAs/GaAs quantum dot electroabsorption modulator," *Appl. Phys. Lett.*, vol. 94, pp. 143108-1–143108-3, 2009.

High Frequency In(Ga)As Quantum Dot Electrooptic Phase Modulators

Wei Liu, Baolai Liang, Diana Huffaker, Harold Fetterman

Department of Electrical Engineering, University of California, Los Angeles, CA 90095, USA

Email: liuwei5088@gmail.com

Abstract: we report new high frequency In(Ga)As traveling-wave quantum dot (QD) phase modulators with 3dB-bandwidths of over 10GHz. For InGaAs QD chain modulators, the half-wave voltages are 4.84V and 5.31V along [011] and [01-1] directions.

OCIS codes: (130.4110) Modulators; (250.7360) Waveguide modulators

1. Introduction

Semiconductor quantum dot (QD) materials have become more and more attractive for making high speed electrooptic (EO) modulators. It has been reported that QD materials have shown large EO effect due to the quantum confined Stark effect (QCSE) [1, 2]. Recent results have shown that the InGaAs QDs can be vertically and laterally aligned [3-5]. QD chains arranged along [01-1] direction have observed in the growth of multilayers of QDs on GaAs (100). The formation mechanism is related to the surface diffusion and strain relaxation during the growth [3-5]. The inter-dot coupling along the QD chain [01-1] is much stronger than along [011]. The QD wavefunctions become anisotropic along different directions, and eventually lead to different device performances. Most of the QD modulator research in literature focused on low frequency or DC response [1, 2]. In the present paper, we extended the traditional InAs QD modulators to high frequency traveling-wave configurations. These modulators show 3dB-bandwidths of over 10GHz. Next, we applied the high frequency traveling-wave designs to new InGaAs QD chain material structures, and the anisotropic properties of devices fabricated along different directions were observed.

2. QD growth and device fabrication

The two QD modulator structures we examined, as shown in Fig. 1, are grown on an n-GaAs (100) substrate by molecular beam epitaxy (MBE). The active region consists of multi-layers of stacked QDs clad by GaAs separate confinement GaAs heterostructures (SCH) sandwiched between AlGaAs cladding layers. Fig. 1 (a) shows the traditional InAs QD structures having a undoped active region consisting of 5 stacked InAs QD layers. Fig. 1 (b) is the new InGaAs QD chain structures, which consists of 16 layers of InGaAs QDs.

Fig. 2 shows the photoluminescence (PL) spectra of the QD wafers at room temperature 300K. The InAs QD PL peak is at 1215nm as shown in Fig. 2. (a). Fig. 2 (b) shows the PL for InGaAs QD chain modulator wafer. From Fig. 2 (b), the PL intensity along [01-1] is ~10% higher than that of the [011] direction. This means PL intensity is higher along the QD chain direction, and consistent with the EO effects we measured. The PL peaks for these devices are far away from the operation wavelength 1.55 μ m to reduce absorption loss.

p-GaAs buffer(1×10^{19})	50nm	p-GaAs buffer(1×10^{19})	50nm
p-Al _{0.3} Ga _{0.7} As (5×10^{17})	1000 nm	p-Al _{0.3} Ga _{0.7} As (5×10^{17})	1000 nm
p-Al _{0.3} Ga _{0.7} As (2×10^{17})	460 nm	p-Al _{0.3} Ga _{0.7} As (2×10^{17})	460 nm
GaAs	117nm	GaAs	117nm
GaAs	35nm	GaAs	17nm
In _{0.16} Ga _{0.84} As 5nm	5 ×	In _{0.5} Ga _{0.5} As QD	16 ×
In _{0.16} Ga _{0.84} As 2nm			
GaAs	117nm	GaAs	2nm
n-Al _{0.3} Ga _{0.7} As (2×10^{17})	460 nm	n-Al _{0.3} Ga _{0.7} As (2×10^{17})	460 nm
n-Al _{0.3} Ga _{0.7} As (5.7×10^{17})	1000 nm	n-Al _{0.3} Ga _{0.7} As (5.7×10^{17})	1000 nm
n-GaAs buffer(5.7×10^{17})	200 nm	n-GaAs buffer(5.7×10^{17})	200 nm
n ⁺ -GaAs Substrate	350 μ m	n ⁺ -GaAs Substrate	350 μ m

(a)

(b)

Fig. 1. (a) Schematic of the InAs QD modulator wafer (b) Schematic of the InGaAs QD chain modulator wafer

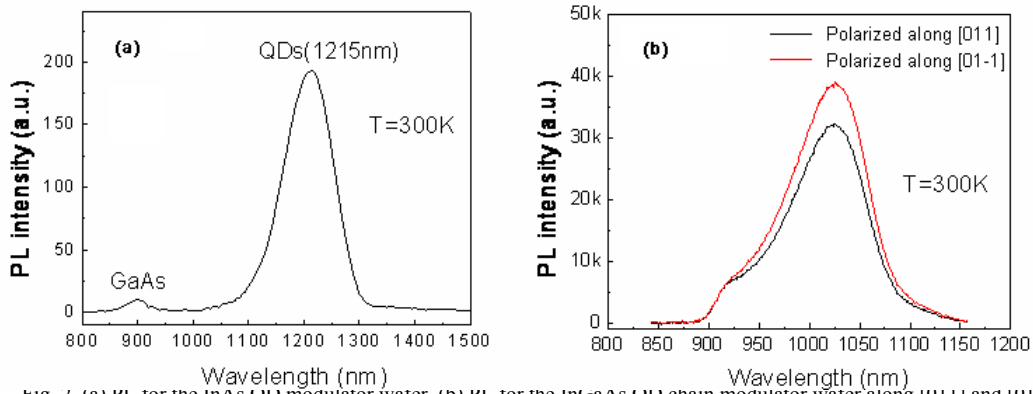


Fig. 2. (a) PL for the InAs QD modulator wafer. (b) PL for the InGaAs QD chain modulator wafer along [011] and [01-1]

The QD modulators were fabricated with p-contact metal deposition, waveguide dry-etching, n-contact metal deposition, BCB polymer coating, BCB dry-etching, and gold electrode plating. Standard optical ridge waveguide structures were fabricated in these QD modulators. The ridge width varied from $3\mu\text{m}$ to $10\mu\text{m}$, and ridge height was $\sim 4\mu\text{m}$. The atomic force microscopy (AFM) picture of the QD chain wafer is shown in Fig. 3 (a). From Fig. 3 (a), the QD chains are clearly aligned along [01-1], and the wafer is no longer symmetric. The cross-section view of the phase modulators are shown in Fig. 3 (b). A thick BCB polymer layer was used to isolate ground and signal electrodes and reduce capacitance.

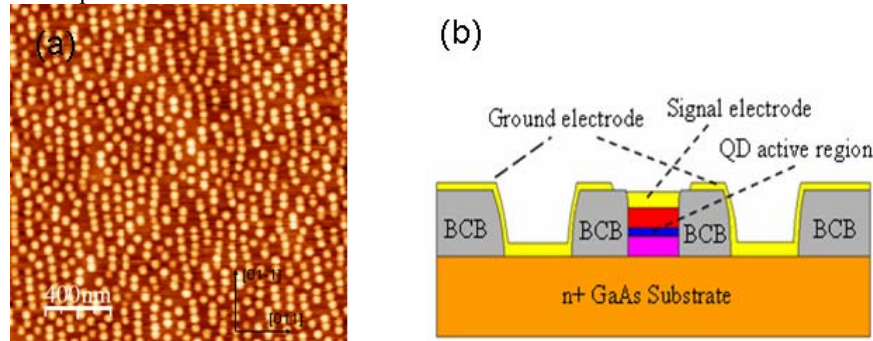


Fig. 3. (a) AFM image of the InGaAs QD chain structure (b) Cross-section view of the phase modulator

3. Experiment Setup and Results

The DC modulation experiment setup was conducted using a polarizer and an analyzer. Laser light was coupled into the modulator through a lens fiber, and the emitted light was gathered through a 40X objective lens. The income light was linearly polarized at 45° relative to the device, which gave equal vertical and horizontal components of the E-field vector. Another polarizer was placed after the coupling objective lens as an analyzer. A signal generator was used to send a triangular modulation to the phase modulator at 100kHz. The Optical signal was detected using a photodiode detector, and was displayed on an oscilloscope.

We initially measured the modulation efficiency of $\sim 9.0\text{V} \cdot \text{mm}$ for $800\mu\text{m}$ -long InAs QD modulators. Next we tested InGaAs QD chain modulators arranging along different directions, and the results are shown in Fig. 4. For 1.5mm -long InGaAs QD chain modulators, the half wave voltage V_π is 4.84V along [011] direction, and 5.31V along [01-1] direction. The correspondent modulation efficiencies are $\sim 7.3\text{V} \cdot \text{mm}$ and $\sim 8.0\text{V} \cdot \text{mm}$. This means that for a 2mm -long In(Ga)As Mach Zehnder modulator using push-pull drive, V_π can be reduced to less than 2.5V . Therefore, QD modulators are potentially suitable for low drive-voltage applications.

The half wave voltage V_π is inverse proportional to EO coefficient, and the polarization plane is perpendicular to the light traveling direction. By comparing the experiment results in Fig. 4 (a) and Fig. 4 (b), the EO coefficient r_{41} along [01-1] is $\sim 10\%$ higher than that along [011] direction. As a result, devices fabricated along [011], in which light is polarized along [01-1], are desirable because of the lower modulation voltage. To further reduce V_π , longer QD chains are preferred. This requires improving the QD growth conditions. We also evaluated the insertion loss by comparing the total losses for devices with different lengths, and the insertion loss is $\sim 6.5\text{dB/mm}$ for InAs QD modulators. The insertion loss reduces to 4.4dB/mm for InGaAs QD chain modulators due to optimizing device

fabrications. The insertion loss is mainly due to the aggregate scattering loss from waveguide sidewalls and the QDs. The loss can be significantly reduced by optimizing device fabrication process and the QD MBE growth.

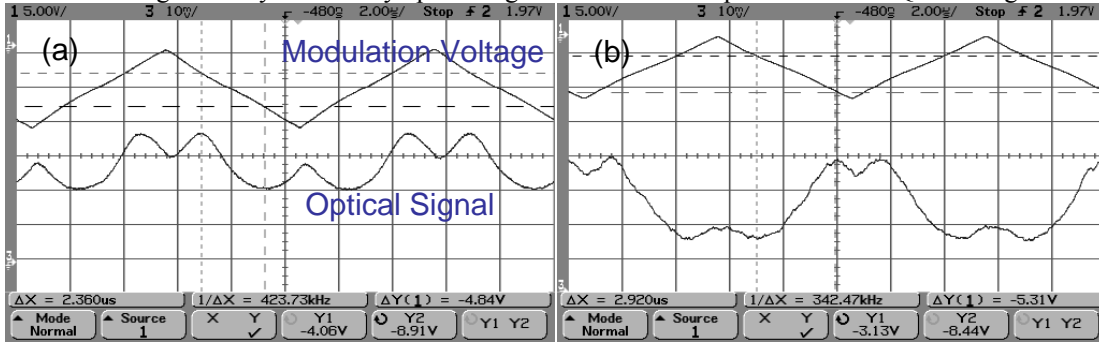


Fig. 4. The half-wave voltage measurement for 4 μ m-wide 1.5mm-long device (a) [011] modulator, V_{π} =4.84V (b) [01-1] modulator, V_{π} =5.31V

The frequency response was measured with a network analyzer (HP8720ES), a high-speed photodetector, two low-noise amplifiers and a 40GHz GSG probe. Calibration runs are included to eliminate the influences from the cables and RF amplifiers, and the measurement results are shown in Fig. 5. The 3dB-bandwidth bandwidth is \sim 10GHz for 800 μ m-long InAs QD modulators, and is \sim 12.2GHz for 800 μ m-long InGaAs QD chain modulators. The improvement for QD chain modulators is mainly due to the better electrode fabrication which reduces the ohmic loss in the gold electrodes. As the 3dB-bandwidth is mainly determined by the electrode design, there is no significant difference between [011] and [01-1] modulators. The roll-off is mainly due to the ohmic losses in the n conducting layers and the gold electrodes.

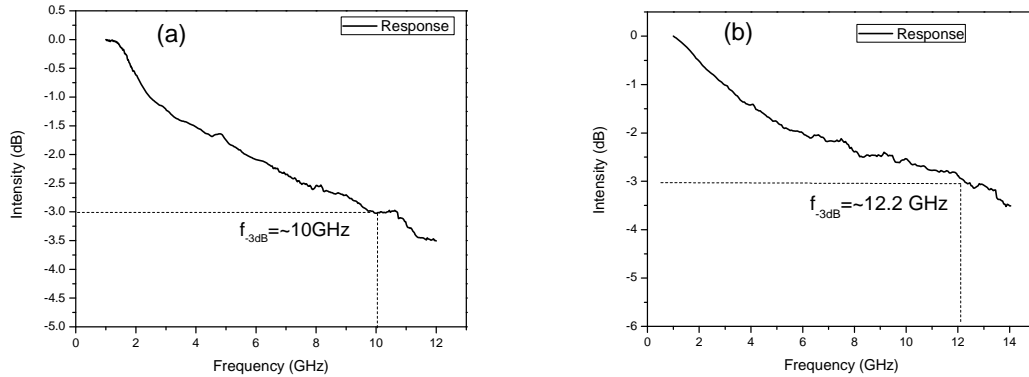


Fig. 5 Frequency response for the 800 μ m-long QD modulators. (a) InAs QD chain modulator (b) InGaAs QD chain modulator

4. Conclusion

In conclusion, we have designed, fabricated, and demonstrated traveling-wave InAs QD modulators and new InGaAs QD chain modulators. Our experimental results show that the 3dB-bandwidths of these QD modulators are over 10GHz, and are limited by the electrode losses. The anisotropic properties of devices fabricated along different directions are observed for QD chain modulators. The EO effect is \sim 10% higher along QD chain [01-1] direction. The modulation efficiencies are \sim 7.3V \cdot mm for [011] modulators and \sim 8.0V \cdot mm [01-1] modulators. By making device longer and using push-pull drive, the half wave voltage V_{π} can be reduced to less than 2.5V for Mach Zehnder modulators. Therefore, In(Ga)As QD modulators are potentially suitable for low drive-voltage and high speed applications and substantial improvements can be obtained by new material configurations.

4. References

- [1] J. Tatebayash, N. Nuntawong, P. S. Wang, Y.-C. Xin, L. F. Lester and D. L. Huffaker, "Strain compensation technique in self-assembled InAs/GaAs quantum dots for applications to photonic devices," J. Phys. D: Appl. Phys., vol. 42, pp. 073002-073014, 2009
- [2] D. B. Malins, A. Gomez-Iglesias, E. U. Rafailov, W. Sibbett, and A. Miller, "Electroabsorption and Electrorefraction in an InAs quantum-dot waveguide modulator," IEEE Photon. Technol. Lett., vol.19, pp. 1118-1120, 2007.
- [3] Z. M. Wang, Yu. I. Mazur, G. J. Salamo, P. M. Lytvyn, V. V. Strelchuk, and M. Ya. Valakh, "Persistence of InGaAs quantum-dot chains under index deviation from GaAs, (100)", Appl. Phys. Lett. vol. 84, pp. 4681-4683, 2004.
- [4] M. Schmidbauer, Z. M. Wang, Y. I. Mazur, R.M. Lytvyn, G. J. Salamo, D. Grigoriev, P. Schafer, R. Kohler, and M. Hanke, "Initial stages of chain formation in a single layer of (In, Ga)As quantum dots grown on GaAs (100)", Appl. Phys. Lett., 91, 093110-1-093110-3, 2007
- [5] D. G. Cooke, F. A. Hegmann, Yu. I. Mazur, W. Q. Ma, X. Wang, Z. M. Wang, G. J. Salamo, M. Xiao, T. D. Mishima, and M. B. Johnson, "Control on self-organization of InGaAs/GaAs, (100) quantum-dot chains", Appl. Phys. Lett. 85, pp. 3839-3841, 2004